# Signal Processing Methods

# for Airborne Lidar Bathymetry

by

Dallas W. Lane

Thesis submitted for the degree of

**Master of Engineering Science**

Department of Electrical and Electronic Engineering
Faculty of Engineering
The University of Adelaide
Adelaide, South Australia

August 2001

# Contents

# Abstract

Airborne Laser Bathymetry is now a well-established technique for detecting the depth of shallow ocean waters, whereby laser pulses are directed downwards from an aircraft into the ocean. By measuring the round trip time difference between the sea-surface and seabed laser return pulses, the depth of water can be estimated. Signal processing methods are then used to correct biases in the estimated depths due to sea-surface wave effects, tidal action, laser beam refraction and photon scattering in turbid water. However there are still inaccuracies in the estimation of these depths.

This thesis examines the susceptibility of existing signal processing methods to errors, and also identifies other possible causes of depth error, not accounted for by existing signal processing methods, by analysis of the detected laser return waveform data. Methods to improve depth accuracy are investigated.

## Declaration

This work contains no material which has been accepted for the award of any other degree or diploma in any other university or other tertiary institution and, to the best of my knowledge and belief, contains no material previously published or written by another person, except where due reference has been made in the text.

I give consent to this copy of my thesis, when deposited in the University Library, being available for loan and photocopying.

Signature_____

Date 30th August 2001

# Acknowledgments

I would like to acknowledge the support, encouragement and information I received from a number of people and organizations in the creation of this thesis.

My involvement in the development of the Australian Laser Airborne Depth Sounder system with the DSTO team led by Mike Penny, my colleague Ralph Abbot, the cooperation of Navy, Vision Abell, British Aerospace and others all lead to my understanding of an operational Airborne Laser Bathymetry (ALB) system.

To Prof. Douglas Gray, my MEng.Sc supervisor, for his informed direction, knowledge of signal processing methods and friendly support.

To the Cooperative Research Centre for Sensor Signal and Information Processing (CSSIP), for providing the special facilities and a friendly environment in which I was able to research much of this work.

To my DSTO supervisors Dr. R Seymour, and Dr. R. Barrett, who have kindly supported this work.

To the lovely Maria, my loving wife, for her encouragement during the period of my research.

# List of Figures

## List of Tables

# Glossary

## Abbreviations

| | |
|---|---|
| ADC | analogue to digital conversion |
| ALB | airborne laser bathymetry |
| CVL | copper vapour laser |
| dB | decibel |
| FOV | field of view |
| GASS | Ground Analysis SubSystem |
| Hz | hertz |
| IR | infrared |
| KHz | kilo-hertz |
| LADS | Laser Airborne Depth Sounder |
| LAT | lowest astronomical tide |
| m | metre |
| MHz | mega-hertz |
| mJ | milli-joule |
| mR | milli-radian |
| MSL | mean sea level |
| nm | nanometre |
| ns | nanosecond |
| PMT | photomultiplier tube |
| PRF | pulse repetition frequency |
| ps | picosecond |
| s | second |
| SBR | signal to backscatter ratio |
| SNR | signal to noise ratio |
| std | standard deviation |

## Symbols

| | |
|---|---|
| $a_w$ | the absorption coefficient of seawater |
| b | the measured sea surface bias error |
| B | the zero depth backscatter parameter of seawater |
| $b_b$ | the backscatter scatter coefficient of seawater |
| $b_f$ | the forward scatter coefficient of seawater |
| $b_w$ | the scatter coefficient of seawater |
| c | speed of light in air ($2.99774 \times 10^8$ m/s) |
| $c_w$ | the total attenuation coefficient of seawater |
| $\Phi_1$ | the first measured value of the green laser beam scan angle |
| $\Phi_2$ | the second corrected value of the green laser beam scan angle |
| $\Delta\Phi$ | the measured sea surface tilt error |
| $d_{bm}$ | the benchmark depth of sea measured relative to lowest astronomical tide |
| $d_{err}$ | the measured residual depth error of the LADS system |
| $d_{lads}$ | the depth of seawater measured by the LADS system |
| $d_{tide}$ | the measurement of tide depth |
| $d_1$ | the first approximation of vertical water depth |
| $d_2$ | the second approximation of vertical water depth |
| H | aircraft height above sea level |
| k | the attenuation coefficient of seawater |
| $k_{cal}$ | the start time of the calibration pulse window |
| $k_{IR}$ | the detected position of the sea surface by the IR laser beam |
| $k_L$ | the large FOV attenuation coefficient of seawater |
| $k_S$ | the small FOV attenuation coefficient of seawater |
| $\eta_w$ | the refractive index of seawater (1.3389) |
| $s_{f1}$ | the first approximation of sea surface pulse position |
| $s_{f2}$ | the second approximation of sea surface pulse position |
| $s_{f3}$ | the third approximation of sea surface pulse position |
| $s_{b1}$ | the first approximation of the bottom pulse position |
| $s_{b2}$ | the second approximation of the bottom pulse position |
| $s_{b3}$ | the third approximation of the bottom pulse position |
| $s_{b4}$ | the fourth approximation of the bottom pulse position |

| | |
|---|---|
| $t_b$ | the time location of the sea bottom pulse |
| $t_{IR}$ | the time location of the IR surface position |
| $t_s$ | the time location of the sea surface pulse |
| $w_c$ | composite 1024 sample waveform |
| $w_r$ | raw 256 sample waveform |
| $\Delta t$ | sample time between digitized waveform samples (2ns) |
| $\Delta_1$ | the time delay between the detected IR surface pulse and the expected true surface position |
| $\Delta_2$ | the time delay due to the slant height of the scanning green laser beam |

## Definitions

(These are the definitions of some of the terms used in this thesis)

| | |
|---|---|
| **LIDAR** | the optical analog of radar, is an acronym for light detection and ranging. |
| **Scattering volume** | that section of water, which scatters the laser light. |
| **Sounding** | the depth and position of a point on the seabed for hydrographic purposes. |
| **PMT** | a photo multiplier tube is a device used to amplify light energy |

# 1. Introduction

LIDAR, the optical analog of radar, is an acronym for LIght Detection And Ranging. Lidar systems employ intense pulses of light, typically generated by a laser source, together with telescopes and sensitive optical detectors, to collect and sense the reflected laser pulses. Atmospheric lidars are commonly used to measure the composition and structure of the atmosphere. The very narrow beam-width, narrow line width, and ultra short pulses of the laser make it possible to optically probe the atmosphere with exceptional sensitivity and resolution. Lidars, when used to measure the range and velocity of hard targets, are usually called laser ranging systems or laser radars.

## 1.1 Motivation

Lidar systems have been in use since the 1960's, for probing the atmosphere to measure the presence of water vapour, wind velocities, and other atmospheric properties. Lidar systems have also been used to detect the range of hard targets, by measuring the round trip time of a pulse of laser energy.

Later in the 1970's experimental airborne lidar systems were developed to measure the depth of shallow ocean waters. The ability of a pulse of green/blue laser light to penetrate ocean water to depths of 50 m to 70 m, allows the measurements of ocean depth. Pulses of infrared (IR) and green/blue laser energy directed downward from an aircraft into the ocean, result in reflected pulses of energy from the surface of the sea and from the ocean bottom. The differential time delay between these reflected pulses can then be used to determine the depth of ocean and produce data for the production of ocean charts. In these systems, corrections need to be made for tidal effects, refraction through the ocean surface, the geometry of the scanning system, surface wave effects, and for the effect of light scattering in seawater. However, significant depth errors in certain conditions are still exhibited [1]. Identification of the causes of residual depth errors would lead to the possibility of further improvement in the depth accuracy of Airborne Lidar Bathymetry systems.

## 1.2 Thesis Outline and Contributions

This thesis investigates the depth accuracy of airborne lidar bathymetry systems. Signal processing algorithms of a typical system are analysed for their susceptibility in producing depth errors. In order to determine which errors are likely to be the most significant in practice, data analysis methods are used to examine real data, to identify and determine the cause of residual depth errors.

• Chapter 2 discusses the fundamentals of lidar systems, covering the various types of lidar systems available. In particular, it discusses the principles of Airborne Lidar Bathymetry (ALB) systems.

• Chapter 3 describes the functional structure of a typical ALB system. In particular it discusses the signal processing methods used.

*Contribution*: A functional structure of a typical ALB system is described.

• Chapter 4 investigates the dependence of the depth accuracy of a typical ALB system on errors. The propagation of errors through the Australian developed Laser Airborne Depth Sounding (LADS) system is studied, using a simplified error model.

*Contribution*: A simplified error model of a typical ALB system is developed.

• In chapter 5 data analysis of real ALB data is performed, to identify significant depth errors. In particular residual depth errors are investigated to determine whether existing signal processing methods were adequate. Significant depth errors are investigated to determine their causes.

*Contributions*: Large systematic residual depth errors are found to be dependant on seawater turbidity.

The correlation of large negative residual depth errors against the late detection of the sea surface by the IR laser beam is found to be insignificant.

The correlations of systematic residual depth errors with various measurements of seawater turbidity (ie seawater attenuation coefficients, pulse width, signal to backscatter ratio and signal to noise ratio) are determined.

A three variable depth bias model, incorporating a signal to noise ratio variable is developed and is found to improve the depth accuracy of a typical ALB system.

The 50% bottom pulse detection method used in a typical ALB system is found to introduce significant depth errors in turbid water conditions.

• In chapter 6, the research is summarized and conclusions are drawn.

# 2. Background Information

The first successful laser ranging measurements to satellites were conducted in 1964. In the early 1970's the first spaced-based laser altimeter was operated in lunar orbit from the Apollo 15, 16, and 17 command and service modules. Airborne laser altimeters provide maps of surface topography, coastal water depth, forest canopies, sea ice distribution, volcanic landforms, impact craters, and ocean wave heights.

## 2.1 Lidar Fundamentals

Profile measurements are accomplished by pulsing the laser and then periodically sampling the detector output. The received signal level is proportional to the density of scatterers and inversely proportional to the square of the distance to the scattering volume. Because reflected signals from atmospheric lidars and gas molecules are usually very weak, most lidars employ very sensitive Photo Multiplier Tube (PMT) detectors that operate in the photo-counting mode. The count given in range bin is related to the number of scatterers in the corresponding volume illuminated by the laser pulse. The most common lidar configuration is a monostatic system. The laser beam is either projected through the receiving telescope or propagates parallel to the optical axis of the telescope. If the system is designed for ranging or altimetry, the receiver measures the round trip propagation time of the laser pulse between the lidar and the target. The distance d to the target is given by the range equation below, where c is the speed of light and T is the round trip propagation time of the laser pulse.

$$d = cT/2 \tag{2.1}$$

Precision timing is accomplished electronically by a device called the time interval unit. A beam splitter directs a small fraction (<1%) of the transmitted laser beam to a photodetector. When illuminated by the laser, the photodetector generates an electrical pulse, which starts a precision clock in the time interval unit. The reflected laser pulse is collected by the receiving telescope and focussed onto another more sensitive photodetector, generating an electrical pulse that stops the clock. The elapsed time is then transmitted to the range computer, which calculates the target distance according to the range equation (2.1). The optical filter and field stop in the telescope are designed to reduce the interference and noise caused by other sources of light. The optical filter limits light transmission to the narrow wavelength range of the laser, and the field stop limits the field of view of the telescope to the region illuminated by the laser beam.

The ranging accuracy depends upon many factors, including the laser pulse duration, the received signal strength, and the timing accuracy of the time interval unit. The most sophisticated systems are used for ranging to retroreflector-equiped satellites and to the retroreflector arrays placed on the moon by the Apollo astronauts. Accuracies of a few centimetres are routinely achieved. Data from these measurements are used to monitor geophysical phenomena such as continental drift, crustal dynamics, and Earth's rotation rate. Because of the extremely high accuracy required, a more sophisticated version of the range equation must be used, which includes the effects of the additional propagation delay introduced by the Earth's atmosphere.

In order to process the photon count profile to yield the density profile of the scatterers, other factors, such as the thickness of the scattering volume and the backscatter cross section, must also be taken into account. The thickness of the scattering volume is related to the laser pulse

length and the receiver range gate length. The backscatter cross section is the effective cross-sectional area of the scatterer, and depends upon many factors including scattering mechanism, optical wavelength, and optical properties of the scatterer. Only when the scatterer is large compared to the wavelength, which may be the case for aerosol scattering, does the physical size of the scatterer influence the value of the optical backscatter cross section.

## 2.2 Atmospheric Lidars

The targets of atmospheric lidars are either suspended dust and aerosols or gas molecules, which are continuously distributed in the atmosphere along the path of the laser beam. Thus atmospheric lidar systems are used to measure density profiles of the scatterers. Atmospheric lidars are classified according to the type of scattering mechanism exploited to make the measurement. Aerosol lidars measure scattering from atmospheric dust and aerosols. Observation with ground based and airborne lidars have provided much of the data about the dispersion and global distribution of volcanic aerosols and about the life cycle and distribution of polar stratospheric clouds. Both phenomena occur in the altitude range between 10 and 35 km. Volcanic aerosols can have a significant influence on climate, while polar stratospheric clouds play a major role in the springtime depletion of ozone over both polar caps.

### 2.2.1 Differential Absorption Lidars

Differential absorption lidars (DIAL) [33] are used to measure particle concentrations in the lower atmosphere. DIAL systems employ two lasers, one tuned to an absorption line of the particle of interest and the other tuned just off the absorption line. By comparing the received signal levels at the two wavelengths, a density profile of the particle can be calculated. A wide variety of important minor constituents in the lower atmosphere, including ozone, are being studied using DIAL systems.

### 2.2.2 Doppler Lidars

Doppler lidars [34] are used to measure tropospheric winds. The scattered laser pulse is doppler shifted in frequency in proportion to the velocity of the scatterer along the propagation path. The frequency shift is measured by combining the reflected signal with the transmitted laser beam, so that the electrical signal generated by the detector is at a frequency equal to the difference between the frequencies of the transmitted and reflected beams. The signal-processing electronics following the photodetector are very similar to those used in Doppler radars. By scanning the lidar beam, the three-dimensional wind vector can be measured. Mobile Doppler lidars have been used to map wind fields associated with a variety of atmospheric phenomena such as frontal passages, downslope flows and gusts, canyon drainage flows, and down bursts caused by severe thunderstorms.

### 2.2.3 Raman Lidars

Raman lidars [33] measure the scattered signal at the Raman shifted wavelength. Because the Raman signal is very weak, measurements are usually restricted to the troposphere at altitudes below 10 km. However, at these lower altitudes, Raman lidars have provided excellent measurements of atmospheric density, temperature, and water vapour concentration.

### 2.2.4 Rayleigh Lidars

Rayleigh lidars [33] are designed to measure the molecular signal, which is proportional to atmospheric density. The atmospheric temperature profile can be calculated from the density profile by using the ideal gas law and the hydrostatic equation. Density and temperature profiles at altitudes up to 100 km have been obtained with powerful ground based systems.

### 2.2.5 Resonance Fluorescence Lidars

Resonance fluorescence lidars [33] are used to measure the density profiles of specific molecular species such as sodium in the upper atmosphere. The laser wavelength must be tuned to the resonance absorption wavelength of the species of interest. When illuminated at the resonance wavelength by the lidar beam, the atoms fluoresce because some of the photons are resonantly absorbed and then radiated. The resonant backscatter cross section is typically many orders of magnitude larger than the molecular backscatter cross section of the species. A sodium resonance fluorescence lidar, for example, can measure the concentration of sodium in the atmosphere. High counts at altitudes below 70 km generally indicate molecular scattering, while sodium scattering is normally quite strong between 80 and 105 km. Meteor trails can also be detected by the observation of very thin scattering layers at 80 km or more. Meteor burn up is the major source of sodium and other metal layers in the upper atmosphere. By studying the density perturbations of these layers, the characteristics of the background wind changes and turbulence can be deduced.

## 2.3 Airborne Lidar Bathymetry

Airborne Lidar Bathymetry (ALB) systems are designed to rapidly measure the depth of shallow seawater using a laser transmitter receiver system located in an airborne platform. Previously, all hydrographic survey work has relied on ship mounted sonar systems. This established approach is being replaced by ALB systems, for most coastal and reef areas, where it is hazardous for survey ships to operate. These systems permit sounding measurements to be made faster, and more economically, in shallow, clear coastal waters. For example, there is a considerable time and cost benefit in charting the coastline of Australia using an ALB system.

### 2.3.1 Airborne Laser Bathymetry Principles

A typical ALB operates as follows. A short pulse of blue-green laser energy is transmitted downwards from an aircraft into the sea, and a receiver detects the reflected energy as a function of time. Half the differences in time, between the detected surface return and the detected seabed return, corrected for slant angle, is a measure of water depth [2].

$$\text{depth} = \tfrac{1}{2}(t_b - t_s).(c/\eta_w)[\cos(\arcsin(\sin\phi/\eta_w))] \qquad (2.2)$$

Where $t_s$ is the detected time of the surface pulse, $t_b$ is the detected time of the seabed pulse, c is the speed of light in air, $\eta_w$ is the refractive index of seawater, and $\phi$ is the angle the laser beam makes with respect to the normal to the water surface. This depth can then be corrected for tide to provide a depth relative to lowest astronomical tide (LAT) suitable for hydrographic map production.

However, there are several problems that must be dealt with in developing a practical ALB system. The selection of a suitable, reliable, high pulse repetition frequency (PRF) laser source, and the design of a suitable receiver unit that can detect large energy surface pulse returns and

yet still detect extremely low energy seabed returns. Differences in energy between surface and seabed returns are of the order of 60 dB. The receiver must, therefore, possess both a large dynamic range and high sensitivity, to overcome this problem. Receiver designs include the use of two frequency systems, spatial filtering and polarization. In a two-frequency system, an IR frequency pulse is used to detect the water surface and a blue-green frequency pulse is used to penetrate the water and detect the seabed. For an ALB system using an Nd:YAG laser, a 1064 nm beam is used for surface detection and a 532 nm beam is used for seabed detection. The return of the IR surface pulse is sometimes used to gate-on the PMT, which is used to sense the seabed return pulse. Spatial filtering is sometimes used to provide an optical block to limit the energy of the surface return, but still allow most of the seabed return energy to be detected. Polarized laser light can be used also, in conjunction with a suitably aligned detector polarizer, to reduce the energy of the surface pulse to the detector. The insertion loss of the polarizer, will however, reduce the signal to noise ratio (SNR) of the system.

Nd:YAG lasers are suitable for ALB systems as the 1064 nm and 532 nm frequencies can be used to detect the surface and the seabed returns respectively. Pulse widths of 2 to 5 ns, PRFs of 20 to 200 Hz, green pulse energies of 5 to 8 mJ ensure reliable, and relatively maintenance free, operation. Early Nd:YAG laser systems were optically pumped using flashlamp technology, however recent systems use solid state diode pumping technology, which is more efficient, more reliable, requires less power and cooling, enables higher PRFs of 400 Hz or higher, and provides pulse widths of 2 to 5 ns.

Copper vapour lasers (CVL) output frequencies of 511 nm (green) 578 nm (yellow) and produce PRFs of 6 to 16 Khz with 3 to 10 ns pulse widths. CVLs are not considered suitable for an airborne environment, because platform accelerations can shorten the expected life of the tube. Also, CVLs have lower pulse energies than comparable Nd:YAG lasers.

### 2.3.2 Typical Airborne Laser Bathymetry Systems

There have been several systems developed over the past 20 years [2]. Listed below are some of the ALB systems that were developed.

WRELADS I, WRELADS II, LADS I, LADS II (Australian)[3-6]
LARSEN 500 (Canadian)[7]
FLASH, HAWKEYE (Swedish)[8-12]
SHOALS (Swedish/Canadian for US Army/US airforce)[13-14]
AOL, ABS, HALS, OWL, (USA)[15-18]
GOI (Russian)[19]
BLOL (Chinese)[20]
Thompson and Sintra (French)
DSS (German)
TRLF (European)

Most of these systems were purely experimental. However some of these systems have been developed to operational ALB systems. For example; the Australian LADS system, the Swedish HAWKEYE system, the Canadian LARSEN system and the US Army/ US Airforce SHOALS system.

Each of these operational systems use the Nd:YAG laser source with wavelengths of 1064 nm and 532 nm. This laser source was chosen to provide the most suitable light frequencies for surface detection and depth penetration of coastal waters. Minor differences in these systems occur due to laser power, laser pulse repetition frequency (PRF), field of view (FOV) of the receiver system, analogue to digital conversion (ADC) resolution, sample rate, etc. The main differences occur because of the scanning system and the sea surface reference method employed. The LADS system differs from the other systems, because it uses a rectangular scanning system for a green laser beam, and an accompanying IR beam fixed vertically downwards to detect the sea surface. The direction of the IR beam was selected to point vertically downwards, to maximise the detection of the sea surface in smooth seas, to provide a reliable sea surface reference. The HAWKEYE and the SHOALS systems both use an IR beam concentric with the green beam, both operating together in a conical scanning pattern. The IR beam again is used to detect the water surface and the green beam to detect the seabed. The conical scan is tilted forward to provide a 15 degree beam scan angle relative to vertical.

The design for an ALB system essentially depended on the choice of a suitable laser source, and on how that laser was to be directed to probe the seabed. Early experimental systems such as WRELADS I etc, were profiling systems, and directed the laser beam vertically downwards into the water. Later systems employed scanning mechanisms to increase the coverage rate of the area to be surveyed. WRELADS II and later LADS systems employed a rectangular scanning mechanism to provide uniform seabed coverage. The Canadian Larsen 500 system used a conical scanning system.

# 3. Signal Processing Methods in a Typical ALB System

A typical ALB (Airborne Laser Bathymetry) system is the Australian developed LADS (Laser Airborne Depth Sounding) system. The LADS system was built in the late 1980's for the Royal Australian Navy (RAN) and was a further development of the prototype WRELADS II system [5]. An improved LADS II system was built by the LADS Corporation and made operational in September 1998. The LADS system essentially consists of an airborne sub-system and a ground analysis sub-system. The airborne sub-system is comprised of laser transmitting and receiving units, scanning optics, and data logging hardware.

A functional block diagram of the LADS airborne system is shown in Figure 1 below.

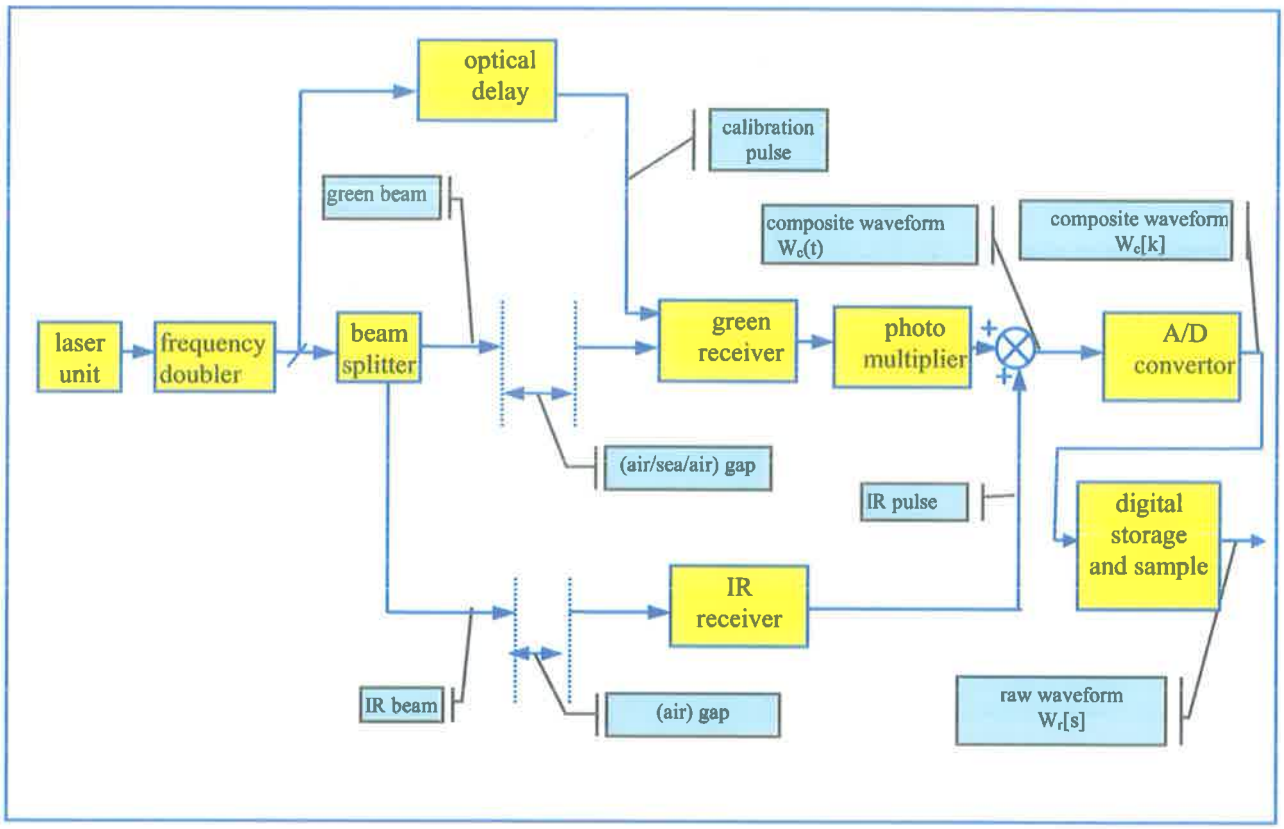


Figure 1. Functional block diagram of the LADS airborne system

A Nd: YAG laser is located in a Fokker F27 aircraft and fires 5 ns laser pulses down-wards into the sea at 168 pulses per second. The IR output of 1064 nm, is frequency doubled to produce green pulses at 532 nm, and a beam splitter separates the IR and green beams. The IR beam is directed vertically down-wards, and expanded (≅50 mR) to illuminate a spot of 25 m diameter on the sea surface, to establish a reliable sea surface datum. The IR pulses, which are reflected off the surface of the sea, are detected by a diode IR receiver in the aircraft.

The narrower green beam (≅6 mR), which illuminates a spot of 3 m diameter on the sea surface, is scanned 15 deg on either side of nadir, and penetrates the seawater to detect the sea bottom. A small portion of the laser source energy is bled off and delayed before being fed into the input of the green receiver, refer Figure 1. The bled off laser energy generates a calibration pulse in

the detected composite waveform, see Figure 2, which provides a relative measure of the energy of the laser pulse at firing time.

The green laser pulses penetrate the seawater to depths of up to 70 m, dependant upon seawater clarity, before being reflected back to the aircraft, where they are detected by a green receiver. The green receiver consists of a Cassegrain telescope, containing a spatial filter to control the field of view of the green beam, a spectral filter to suppress unwanted light and a polarisation filter to attenuate surface reflections. The field of view of the spatial filter is set at 40 mR for all scanning beams, except for the first beam in each scan, where the field of view is set to 8 mR. The spectral filter is designed to pass 532 nm light with a bandwidth of 0.6 nm.

The output of the green receiver is passed through a PMT, where it is combined with the IR pulse output from the IR receiver, to form composite waveforms (refer Figure 2). The gain of the PMT is controlled for non-extremity beams (refer to Figure 4) to optimise the SNR of the reflected bottom pulses, while for the two extremity beams, the gain of the PMT is kept constant, to provide constant gain waveforms suitable for the evaluation of seawater turbidity parameters. The composite waveform signals are input into an analogue to digital converter, where they are sampled every 2 ns to record digital composite waveforms of 1024 samples. Note that a fixed time delay is used before recording the 1024 waveform samples to account for the 500 m aircraft altitude. The position, of the IR pulse in these waveforms, represents the detection time of the sea surface by the IR beam. Note that; see Figure 2, the detection time of the sea surface by the green beam occurs later in time, due to the longer propagation delay in the green receiver hardware and the PMT than in the IR receiver. This delay is accounted for, when reducing the composite waveforms of 1024 samples, to raw waveforms, refer to para 3.2, where the position of the IR pulses are used to position 256 samples of the green laser waveforms to form the raw waveforms. The reduction in waveform size to 256 samples is required to reduce storage size and recording time, when logging the waveform data to magnetic recording media (ie compact disc) in the aircraft.

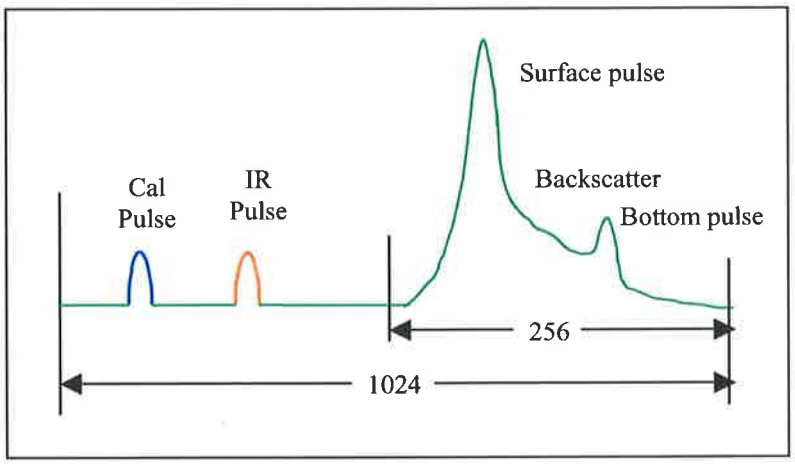


Figure 2 Composite waveform structure

A Ground Analysis Sub-system processes the recorded raw waveform LADS data and uses that data to calculate the depth and position of soundings. A functional block diagram of the ground analysis system is shown in Figure 3. Note that the symbols used are defined later.

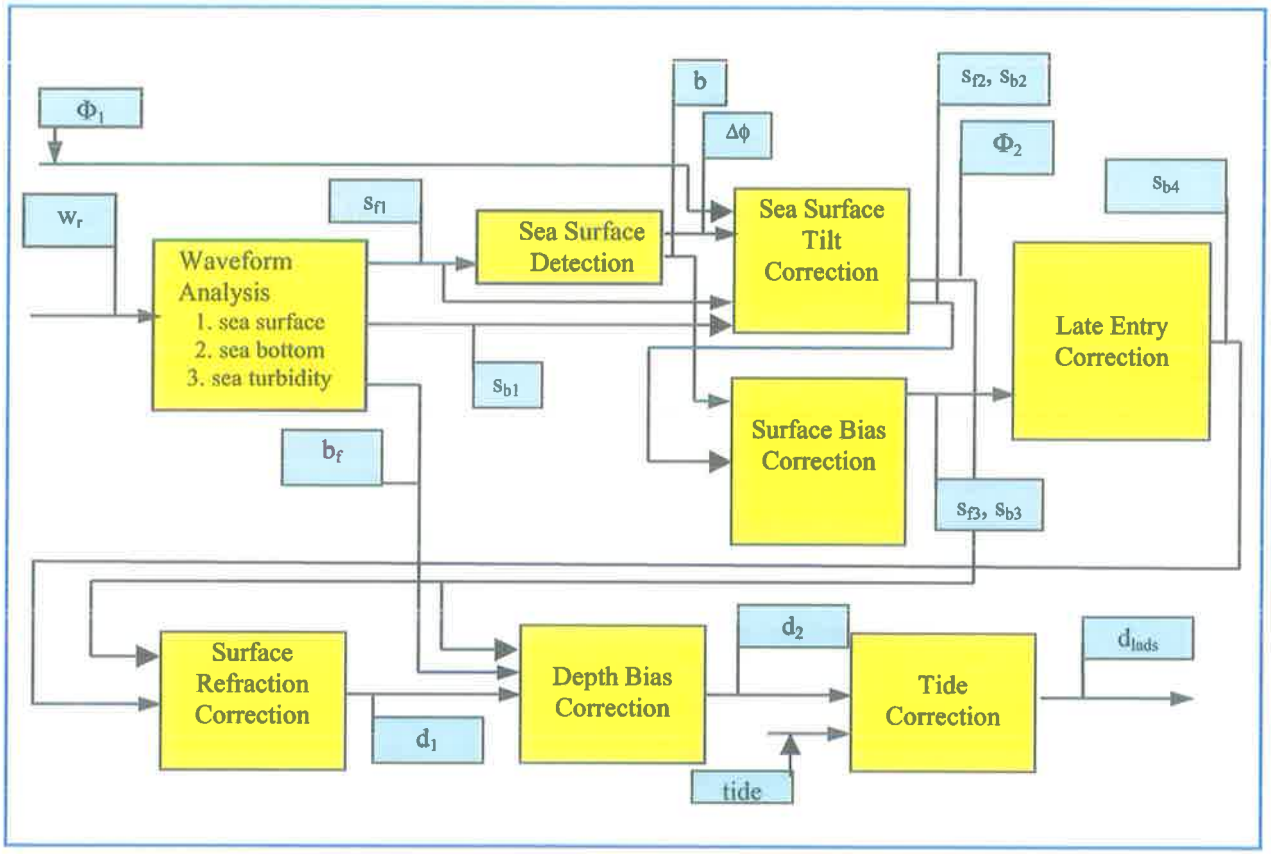


Figure 3. Functional block diagram of the LADS ground analysis system

Briefly, the surface and bottom pulses of the non-extremity raw waveforms ($w_r$) are used to detect the position of the sea surface and the sea bottom, while the backscatter region of the extremity waveforms is used to estimate seawater turbidity. The positions of the raw waveform surface pulses, are then filtered to determine the mean sea level and any apparent sea surface tilt. Corrections to the detected positions of the sea surface and sea bottom are then made, to allow for any determined sea surface bias (b) or any apparent sea surface tilt ($\Delta\phi$), refer section 3.4. Further corrections are made to depth positions for late entry of the laser beam due to detected wave action, air/seawater surface refraction, depth bias due to light particle scattering and tide. The resulting depths ($d_{lads}$) are then evaluated for selection as sounding depths for chart production.

As illustrated in Figure 4, the LADS system is designed to produce a rectangular pattern of depth positions, with a nominal spacing between adjacent depth positions of 10 m. The scanning system, is intended for an aircraft height and speed of 500 m and 70 m/s respectively, and produces 24 laser positions (or spots) per scan and 7 scans per second. Data is stored in 2 s frames of 14 scans, which results in a total of 336 raw waveforms stored per frame of data.

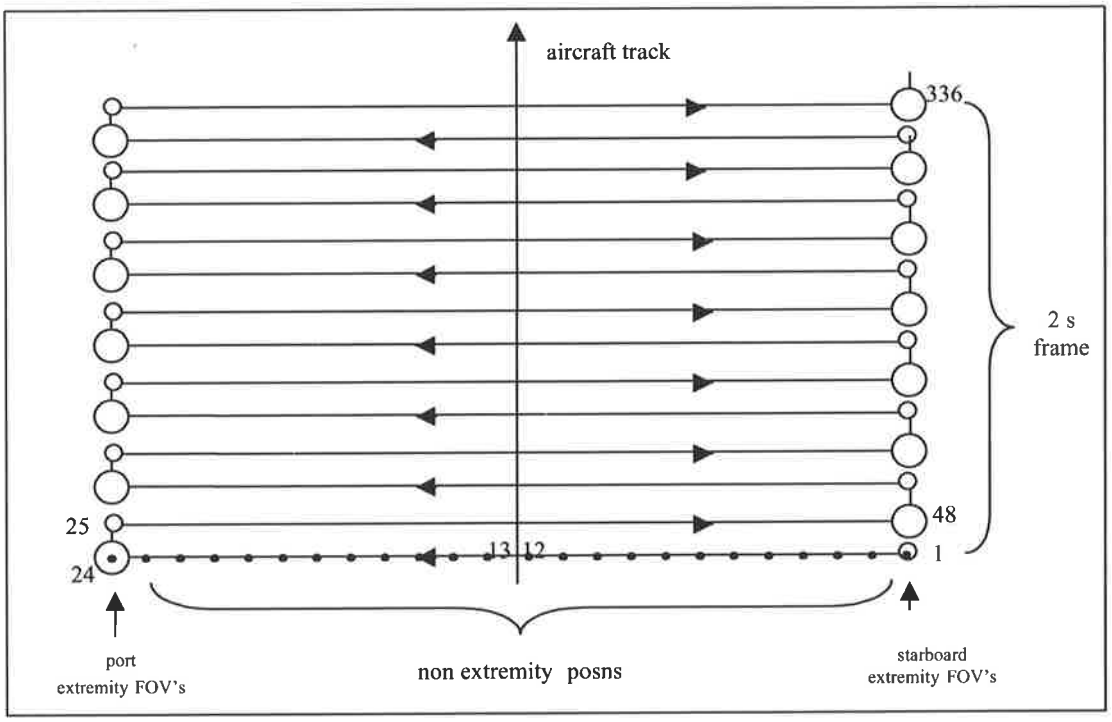


Figure 4. LADS scan pattern

In LADS, all depths are calculated from non-extremity waveforms. Here, the field of view (FOV) of the green receiver is maintained large (40m R) and the gain of the PMT is dynamically controlled to suppress backscatter noise while amplifying the returned bottom pulse, as discussed in [22]. The large FOVs collect the maximum amount of returned laser light energy for bottom pulse detection, while the PMT gain control maximizes the SNR of the bottom pulses.

As mentioned previously, only the extremity waveforms are used to estimate seawater turbidity. Here, as the FOV of the green receiver is switched between small (8 mR) and large (40 mR), the raw waveforms produced are analysed to calculate attenuation coefficients $k_S$ and $k_L$ , for small and large FOV respectively. Here, because the gain of the PMT is held constant for each waveform, the exponential decay of the waveform can be estimated, as explained in Section 3.3.3.

A more detailed explanation of relevant functional blocks is now given.

## 3.1 Anologue to Digital Conversion

All continuous composite laser waveforms $w_c(t)$, refer to Figure 1, are digitised by a 6 bit Biomation A/D converter, which samples each waveform at 2 ns intervals and stores each resulting digitized waveform ($w_c[k]$) as 1024 samples. A sample interval of 2 ns was selected, so that the sampling frequency of 500 MHz is greater than twice the highest frequency component of $w_c(t)$, to prevent aliasing errors.
Therefore, we have

$$w_c[k] = w_c(k\Delta t),\ k = 1 \text{ to } 1024 \qquad (3.1)$$

where $\Delta t = 2$ ns

## 3.2 Digital Waveform Storage

Composite laser waveforms ($w_c[k]$ of 1024 samples) are reduced to raw waveforms ($w_r[s]$ of 256 samples) for economy of storage and computer processing time, to allow data logging to be accomplished in real time. The 256 samples of the composite laser waveforms that are selected for logging are those, which contain the reflected surface and bottom pulse returns of the green laser beams.

The position of the IR pulse in the composite waveforms determines a principal (or nominal) IR time reference in the raw waveforms at $w_r[15]$, as indicated in Figure 5. Here the raw waveforms ($w_r[s]$ of 256 samples) consist of the last section of the composite waveforms as defined by equation (3.2). The nominal IR surface reference represents the expected detected position of the sea surface by the scanning green beam, allowing for delays $\Delta_1$ and $\Delta_2$. Delay $\Delta_1$ accounts for the delay in the response time of the green receiver and the PMT electronics compared with the response time of the IR receiver electronics, and delay $\Delta_2$ accounts for the delay due to the extra slant distance travelled by the scanning green laser beam. Note that some variation in the position of the green beam surface position in relation to the nominal IR sea surface position will occur because of wave action.

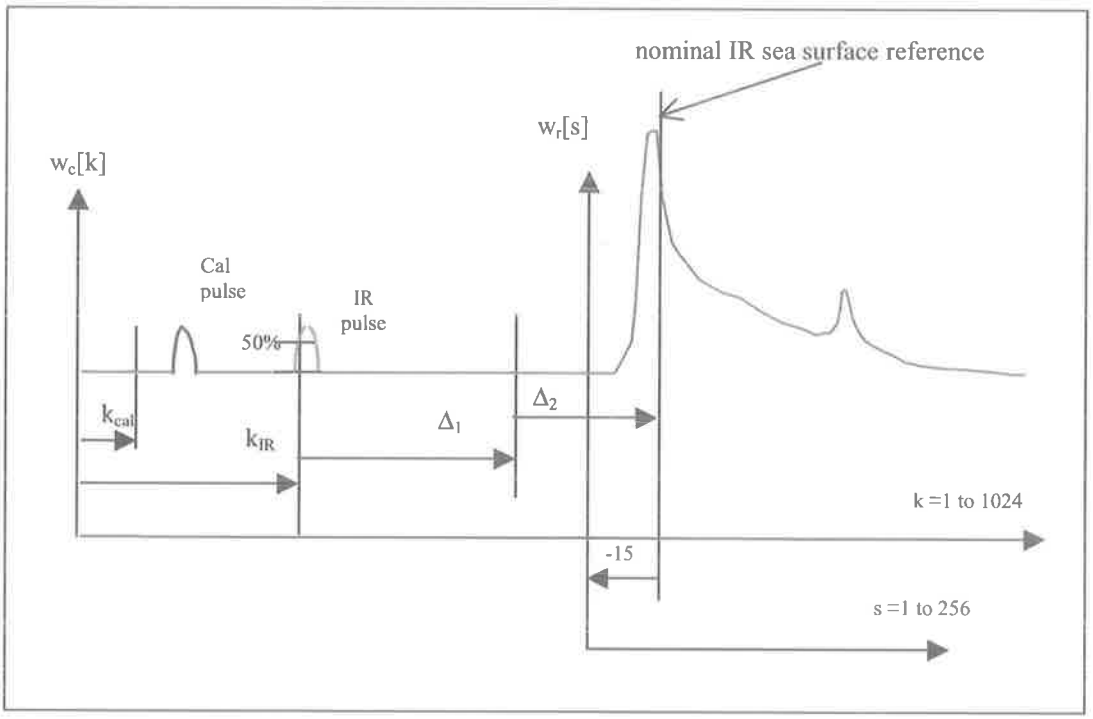


Figure 5 Raw laser waveform structure

Therefore we have:

$$w_r[s] = w_c[s + k_{IR} + \Delta_1 + \Delta_2 - 15],\ s=1 \text{ to } 256 \qquad (3.2)$$

where

$k_{IR}$ is the 50% pulse level detection position of the IR surface pulse. (It represents the sample time when the IR pulse detected the sea surface)

$\Delta_1$ is the time delay between the detected IR sea surface pulse and the expected true surface position.

$\Delta_2$ $= 2H(\sec\Phi_1-1) / (c.\Delta t)$ and is the time delay to account for the slant height of the scanning green laser beams, where H is the height of the aircraft above the sea surface, measured by the IR laser beam and $\Phi_1$ is the measured green laser beam scan angle. $[= 2H(\sec\Phi_1-1) / (c.\Delta t)]$

For extremity waveforms, calibration pulses replace the end of the raw waveforms to provide calibration parameters, which can be used to calibrate backscatter amplitudes. In this case

$$w_r[s] = w_c[s-200+k_{cal}],\ s=200 \text{ to } 256 \qquad (3.3)$$

where

$k_{cal}$ is the start time (sample index) of the calibration pulse window.

## 3.3 Waveform Detection and Analysis

The stored raw waveforms $w_r$ are retrieved and processed to determine the location of the sea surface, the location of the sea bottom and the turbidity of the seawater.

The shape of the raw waveforms will vary with sea surface conditions, seawater clarity, seawater depth, and sea bottom characteristics. Less green laser energy is reflected back from the sea surface towards the aircraft for laser beams angled away from the vertical, than for laser beams directed vertically downwards, especially in smooth seas. In these conditions, some of the reflected laser beam surface energy is lost to the field of view of the green receiver, which results in small or non-detectable surface pulses. Seawater backscatter energy is higher in turbid seawater, and generally results in large backscatter envelopes and small bottom pulses, while in clear seawater, less laser energy is lost and larger bottom pulses result. Reflected laser energy from the seabed depends on the characteristics of the bottom. Sandy bottoms provide highly reflective surfaces, and larger bottom pulses usually result, while muddy weedy bottoms absorb and scatter most of the laser beam energy, resulting in much smaller bottom pulses.

The condition of the sea surface is particularly relevant when valid surface returns are required by the surface filter, in determining the true mean sea level. In smooth seas, valid surface reflections are generally only obtained from near nadir waveforms, as surface reflections for laser beams directed away from nadir, are generally lost to the field of view of the green receiver as previously mentioned. In rough seas however, valid surface returns are observed for most of the waveforms across the scan.

Figure 6 below shows a scan set of 24 waveforms from a two second frame of data. A typical non-extremity raw waveform is shown highlighted, and shows a surface pulse, a region of backscatter energy and a bottom pulse. Here the waveform detection process examines the waveform for the existence of a valid surface pulse and bottom pulse.

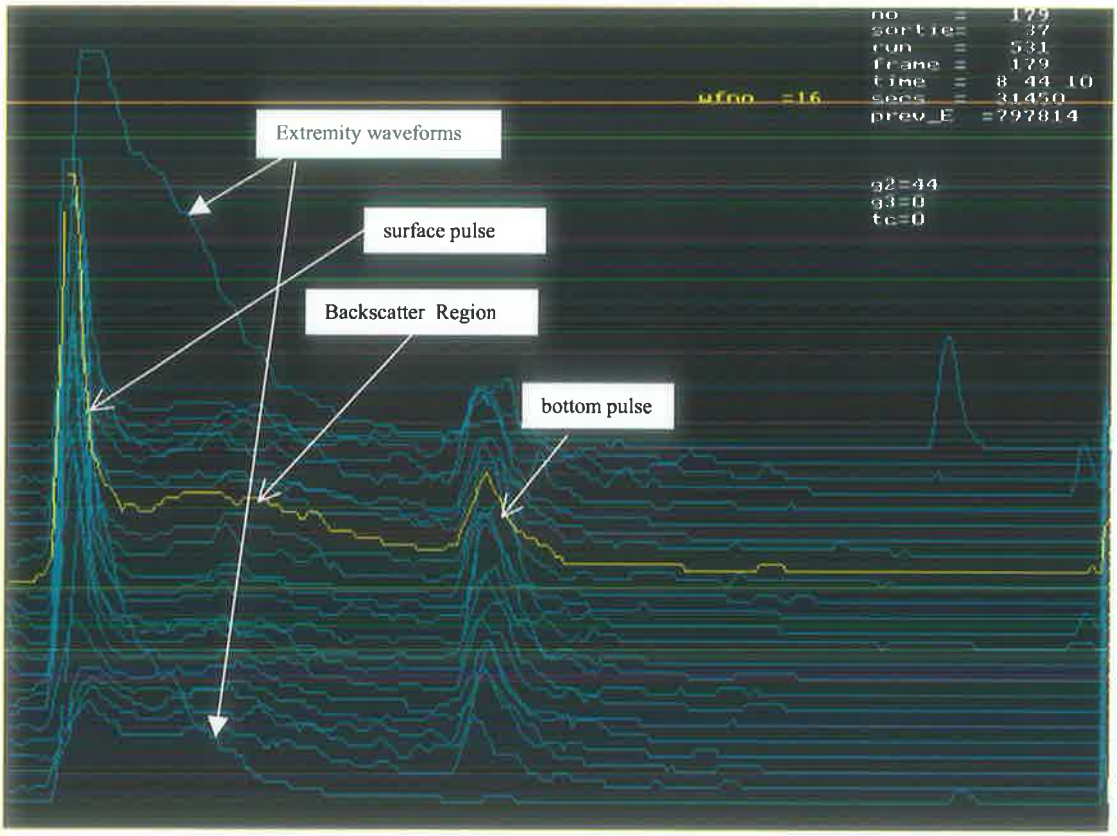


Figure 6. A typical LADS raw waveform

Two extremity waveforms are also shown in Figure 6. They are typical of extremity waveforms used to determine seawater turbidity parameters, as explained in section 3.3.3, and the backscatter region of these waveforms is an indication of the amount of scattering of the green laser beam in the seawater. The two pulses located at the extreme right of these two waveforms are calibration pulses, mentioned previously, and are not currently used in any subsequent calculations.

### 3.3.1 Surface Position Estimation

All non-extremity raw waveforms, are examined within a surface region for the existence of a surface pulse, refer to Figure 7.

The surface region is defined as the first 30 2 ns samples of the raw waveform, which will allow for wave action of up to plus or minus 3 1/3 metres. As mentioned previously, for smooth seas the surface reflected laser energy is generally reflected away from the field of view of the green receiver and the detected laser energy is mostly due to backscatter energy from seawater molecules and other seawater impurities. A true surface reflection is therefore recognised when a sufficiently fast rise time pulse is detected within the surface region.

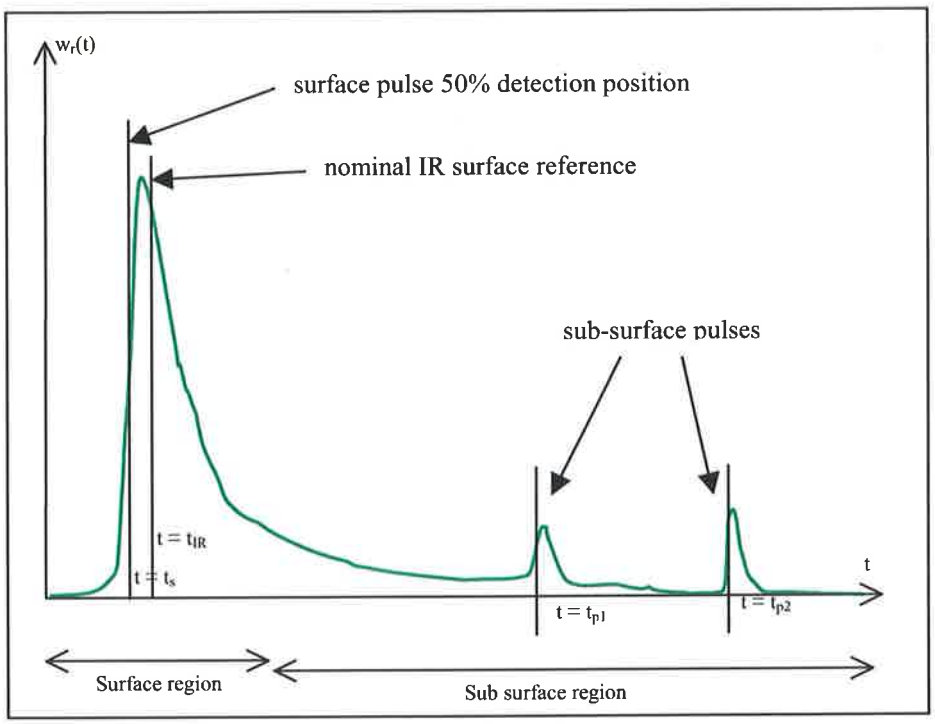


Figure 7 Surface and bottom pulse detection

A surface pulse is said to exist, if within the surface region, a significant pulse is detected, and the rise time of the pulse is less than 12 ns. The rise time of the pulse is defined as the time interval between the 20% and the 80% height of the leading edge of the pulse, and pulse detection is defined as the time at the 50% pulse height on the leading edge of the pulse.

When a surface pulse is determined, then the position ($s_{f1}$) of the surface in metres, with respect to the nominal IR surface reference is determined by:

$$s_{f1} = (t_s - t_{IR})(c\Delta t)/(2\eta_w) \tag{3.4}$$

where $t_s$ is the 50% pulse level time position of the surface pulse and $\eta_w = 1.3389$.
$t_{IR} = 15(2\eta_w/c\Delta t)$ and is the time position of the nominal IR surface reference in the raw waveform, as discussed in section 3.2.

### 3.3.2 Bottom Position Estimation

After estimation of the surface position the waveforms are filtered by zero phase shift high and low pass linear filters, to remove low and high frequency noise components and the sub-surface region is searched for up to two sub-surface pulses (see Figure 7) as follows. A moving average filter (with a 10-sample bandwidth) is moved along all samples in the filtered waveforms [30] to estimate pulse energy values. The two largest pulse energy maximum values are found, which locates pulse1 and pulse2, if they exist. The 50% position of each of the identified pulses, $t_{p1}$ and $t_{p2}$, is then determined. The most probable pulse is then determined, as suggested by Billard [21] and the position ($s_{b1}$) in metres of this bottom pulse relative to the IR surface position determined by:

$$s_{b1} = (t_p - t_{IR})(c\Delta t)/(2\eta_w) \tag{3.5}$$

where $t_p$ is the 50% pulse level time position of the most probable bottom pulse.

### 3.3.3 Seawater Turbidity Parameter Estimation

It has been shown by Billard et al [22] that the optical attenuation coefficient (k) and a backscatter parameter B of seawater can be estimated from constant gain laser waveforms collected by a laser-based airborne hydrographic system. Here it was shown, assuming uniform seawater turbidity with depth, that the returned laser power to an airborne platform can be represented by a simple exponential expression of the form:

$$P(d) = B \exp(-2kd) \tag{3.6}$$

where d is the distance below the sea surface, k is the attenuation coefficient and B is a zero depth backscatter parameter. Regression analysis was then used to estimate B and k. It should be noted that k will vary with the FOV of the green receiver, dependent upon the scattering of the laser beam. For example, in clear seawater with less scattering of the beam there will be less dependence of k on FOV than in turbid seawater. It should also be noted, that B is dependent upon the transmitted power of the laser pulse.

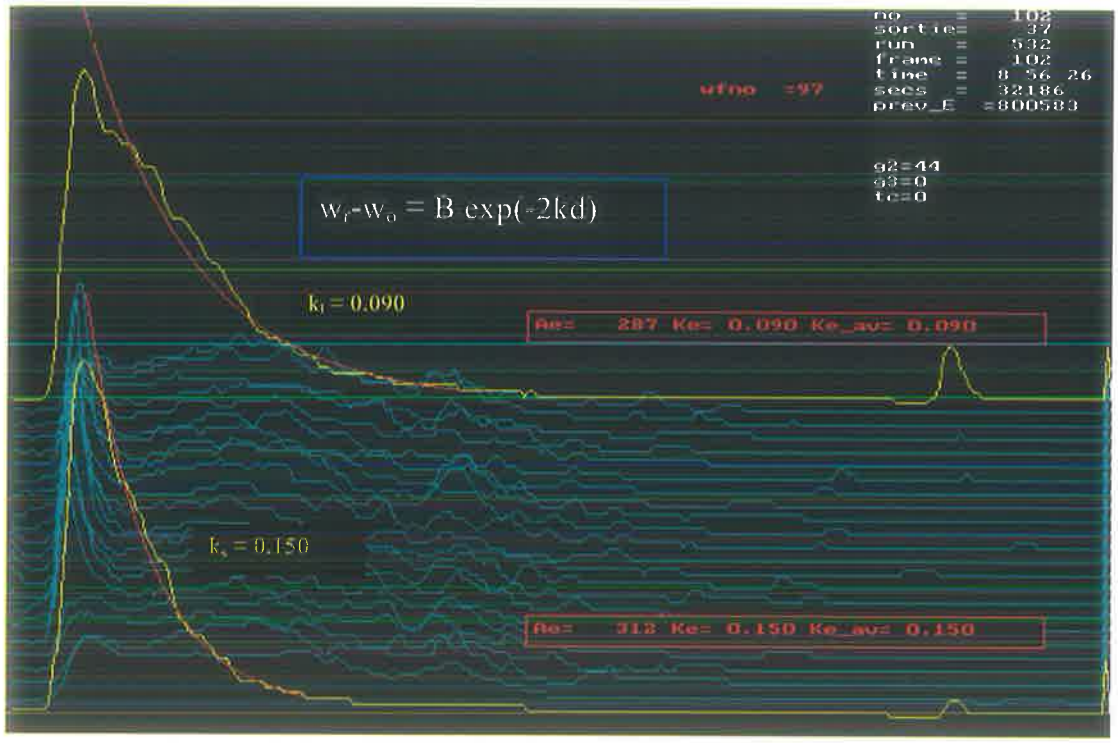


Figure 8 Estimation of turbidity parameters

In LADS, where the extremity waveforms are specifically amplified with constant gain, regression analysis is used to fit an exponential expression, refer figure 8, and estimate B and k. From this analysis, k for both large ($k_L$) and small ($k_S$) fields of view and B for large fields of view are calculated, where $k_L = k$ , for large fields of view and $k_S = k$, for small fields of view.

Estimates of k are obtained by regression analysis of the logarithm of the extremity waveforms in the backscatter region, excluding any sea-surface or seabed reflected energy.

$$w_r[s] = w_o + B \exp(-2kd[s]) \tag{3.7}$$

$$\ln(w_r[s] - w_o) = \ln(B) - 2kd[s]$$

where

$$d[s] = (s-t_{fl})\,(c\Delta t)/(2\eta_w)$$

and

$w_o$ = base level of the waveform
$w_r[s]$ = amplitude of the extremity raw waveform
B = backscatter amplitude at zero depth
k = attenuation coefficient

For the calculated turbidity values to be considered valid, k must be greater than say $0.02m^{-1}$ and the number of good points in the fit must be greater than 10.

Now

$k_s$ = k for small FOV extremity waveforms
$k_L$ = k for large FOV extremity waveforms

This estimation is discussed in detail by Billard, in [22], where the optical properties that are relevant for monochromatic unpolarised light in seawater are defined.

$a_w$ is the absorption coefficient of seawater
$b_w$ is the scattering coefficient of seawater
$b_f$ is the forward scatter coefficient of seawater
$b_b$ is the backscatter coefficient of seawater

and

$c_w$ is the total attenuation coefficient of seawater (where $c_w = a_w + b_w$)

The method used in LADS to estimate seawater turbidity is that proposed by Billard [23], where $b_f$ is estimated as a function of $k_S$ and $k_L$. Here he reports that theoretically, $k \rightarrow a_w$ for a sufficiently large FOV of the receiver optics and that $k \rightarrow c_w$ for a small FOV. In practice some allowance must be made for the relevant scattering phase function, the relevant single scattering albedo $\omega_o$ and the actual FOV. However as $k_L \sim= a_w$ and $k_S \sim= c_w = a_w + b_w$, then $b_w \sim= k_S - k_L$. He also noted [23], that the backscatter coefficient $b_b$ is determined as $b_b = b_w - b_f$ and is typically no more than 1-10% of $b_w$. Thus as $b_f$ is approximately 90-99% of the total backscatter $b_w$, then $b_f$ can be represented as some function of $k_S$ and $k_L$.

$$b_f = f(k_S , k_L) \tag{3.8}$$

This parameter, which is an estimation of the forward scattering of photons through the seawater, is then used in LADS to account for the observed depth biases, measured by the LADS system. In laser bathymetry it is the forward scattering light that detects the seabed and reflects back to the airborne receiver.

## 3.4 Mean Sea Surface Estimation

In LADS, as mentioned previously, the wide vertical IR laser beam is used to provide a reliable first estimate of the mean sea level. It illuminates a spot of 25 m diameter on the sea surface and the upward reflected laser energy is readily detected by the IR receiver. However two principal effects limit the accuracy of the IR beam in detecting the mean sea level. Firstly, where there is wave action, the sensitive IR receiver detects the returned energy from the wave peaks, resulting in sea level measurements, biased towards the peaks of the of the wave action.

Secondly, the 25m diameter spot size is restricted to surface waves with wavelengths less than 25m, to provide adequate sea surface position averaging, refer Figure 9.

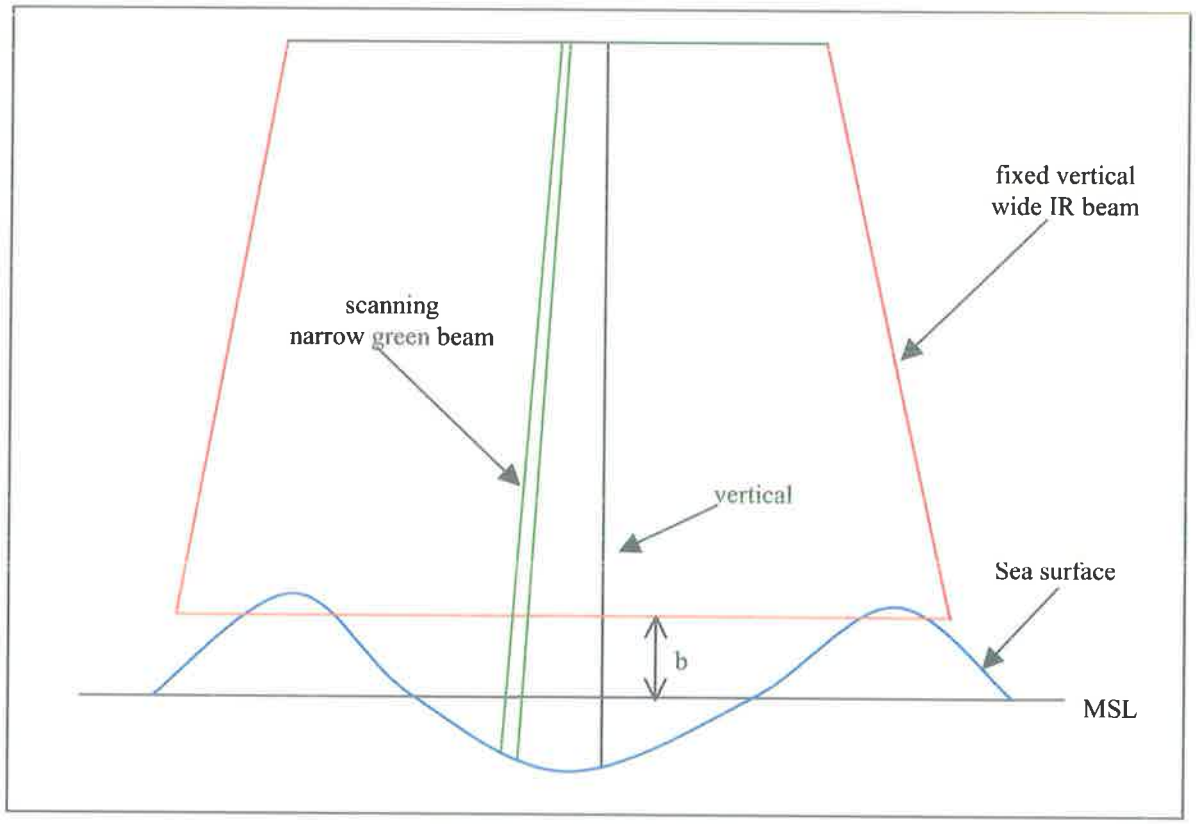


Figure 9 Sea surface detection geometry

The narrower scanning green laser beam is then used to determine a more accurate mean sea level estimate than the wide vertical IR beam. The green laser beam, which illuminates a 2.5 m diameter spot, will act as a profiler and track the sea surface through the peaks and troughs of waves having wavelengths less than 1.5 m. By averaging the positions of the valid green beam surface returns with respect to the corresponding surface positions estimated by the IR beam, any sea-surface bias, and any apparent tilt in the measured position of the sea surface, can be evaluated. A predictive Kalman filter method described in [24] is used adjusted for LADS configuration, to calculate sea surface bias (b) and sea surface tilt error ($\Delta\Phi$). A sea surface tilt error will be detected when there is a tilt off horizontal in the airborne laser platform. Another consideration occurs in glassy seas, where the reflected energy of the green laser pulse is often reflected away from the field of view of the green beam receiver, and the only detected valid sea surface returns are from nadir pulses. This can affect the accuracy in estimating tilt, refer section 4.6.

## 3.5 Sea Surface Corrections

The sea surface tilt error ($\Delta\Phi$), determined by the surface filter, is used to correct the green beam scan angles ($\Phi_1$), the position of surface ($s_{f1}$) and sub-surface ($s_{b1}$) pulses.

Any detected sea-surface tilt indicates an error in the vertical reference of the laser platform and therefore and error in the measurement of scan angles relative to vertical. This requires a correction; to account for an incorrect time delay ($\Delta_2$) used in the position determination of raw waveforms, refer to section 3.2.

$$\Phi_2 = \Phi_1 + \Delta\Phi$$
$$s_{f2} = s_{f1} - d_A\Delta\Phi \quad (3.9)$$
$$s_{b2} = s_{b1} - d_A\Delta\Phi$$

where

$\Phi_1$ is the measured scan angle of the green laser beam

$\Phi_2$ is the second approximation of the scan angle of the green laser beam

$s_{f2}$ is the second approximation of the sea surface pulse position in metres

$s_{b2}$ is the second approximation of the sea bottom pulse position in metres

and

$$d_A = \partial((H/\eta_w)/(\sec\Phi_1 - 1))/\partial\Phi_1 = (H/\eta_w)(\sec^2\Phi_1)\sin\Phi_1$$

Further corrections are necessary, to the positions of both the surface and the sub-surface pulses, to account for any calculated surface bias error.

$$s_{f3} = s_{f2} - b \quad (3.10)$$
$$s_{b3} = s_{b2} - b$$

where

$s_{f3}$ is the third approximation of the sea surface pulse position

$s_{b3}$ is the third approximation of the sea bottom pulse position

## 3.6 Sea Surface Late Entry Correction

A late entry correction is used to correct the position of bottom pulses, to account for wave trough action. The initial calculation of the position of the bottom pulse, refer to para 3.3.2, assumes the time of laser beam propagation, from the IR surface position to the sea bottom and back, is totally in seawater. This is not the case where a wave trough occurs, and the $(1 - 1/\eta_w)$ term accounts for the difference in speed of the laser energy in air as compared with its speed in seawater, refer Figure 10.

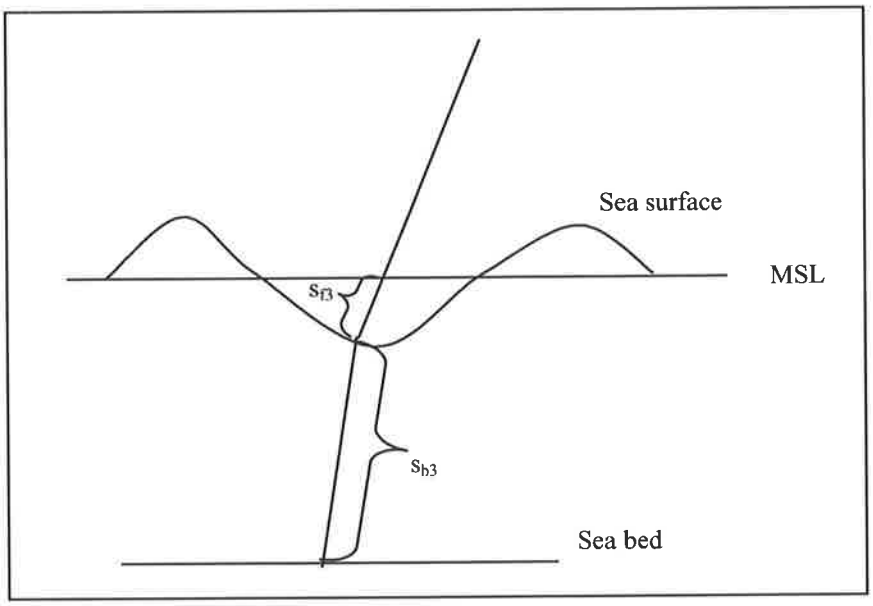


Figure 10 Sea surface late entry diagram

For example, the late entry of the green laser pulse into the seawater will cause it to take less time for the return trip from the mean sea level to the sea bottom than if there were no late entry. This results in the depth to the sea bottom being calculated deeper than it actually is (time to distance calculations assume seawater light velocity conversion). A correction must be made. In this case, $s_{f3}$ (the position of the surface relative to the mean sea level) in the formula below would be negative and $s_{b3}$ would be adjusted to be shallower.

$$s_{b4} = s_{b3} + (1 - 1/\eta_w)\, s_{f3} \qquad (3.11)$$

When the laser beam encounters a wave peak, no correction is required, because there is no air path between the mean sea level and the sea surface. The sea surface and sea bottom positions were calculated assuming laser pulse propagation in seawater, refer to equations 3.4 and 3.5.

## 3.7 Sea Surface Refraction Correction

$s_{b4}$ represents the slant depth of the seabed (in metres) relative to the mean sea level. Allowance must now be made for the refraction of the laser beam across the air/sea interface and to calculate the vertical depth $d_1$ of the seawater, refer to Figure 11.

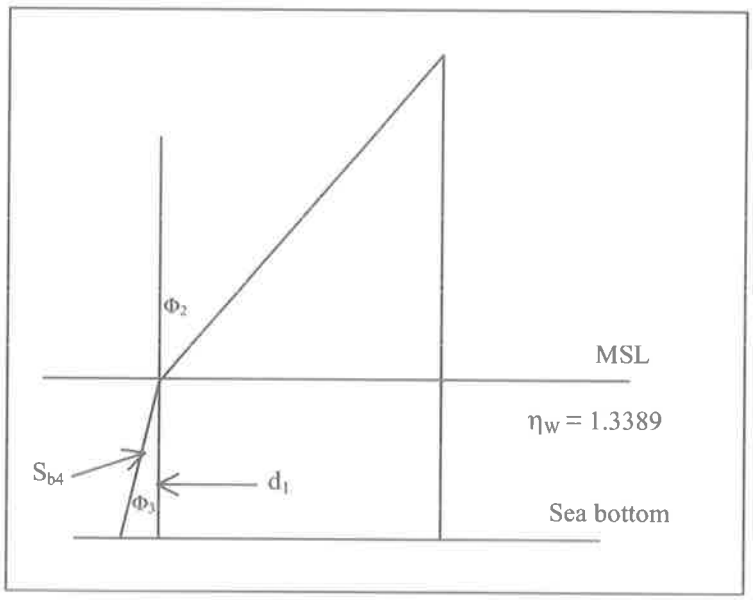


Figure 11 Sea surface refraction correction

Initially the vertical depth (in metres) can be calculated as:

$$d_1 = s_{b4} \cos(\Phi_3) = s_{b4} \sqrt{(1 - \sin^2(\Phi_3))},$$

where

$\Phi_3$ is the refracted laser beam scan angle.

Allowing for refraction and assuming a flat sea surface at the point of beam entry:

$$\eta_w = \sin(\Phi_2)/\sin(\Phi_3) \quad \text{or} \quad \sin(\Phi_3) = \sin(\Phi_2)/\eta_w$$

$$d_1 = s_{b4} [1 - (\sin\Phi_2 / \eta_w)^2]^{1/2} \qquad (3.12)$$

## 3.8 Depth Bias Correction

A further correction to $d_1$ is required to account for the delay in detection time of the reflected bottom pulse, due to light scattering in seawater. The effect of such scattering is to lengthen the path length of light photons in seawater and delay their detection time. This phenomenon was investigated by Billard *et al* [25], where an empirical predictive depth bias model was proposed based on seawater depth and laser beam scan angle. Later studies by Penny, Abbot and Lane [29,1] developed two depth bias models, one based on seawater depth ($d_1$) and laser beam scan angle ($\Phi_2$) and the other based on seawater depth ($d_1$), laser beam scan angle ($\Phi_2$) and a forward scatter coefficient ($b_f$), to account for the effect of seawater turbidity on depth bias. These models are classified Commercial in Confidence and are not disclosed in this thesis.

Therefore we have:

$$d_2 = d_1 - d_{bias} \tag{3.13}$$

where

$$d_{bias} = f(d_1, \Phi_2) \text{ or } f(d_1, \Phi_2, b_f)$$

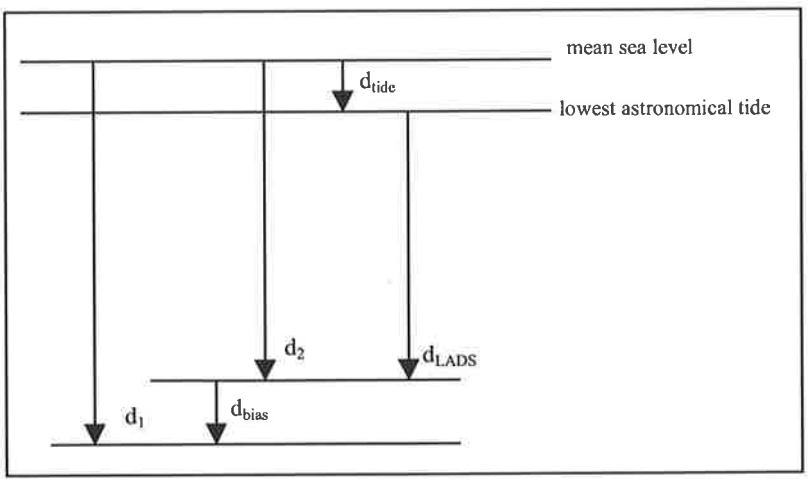


Figure 12 Depth bias and tide corrections

## 3.9 Tidal Correction

Finally depths must be related to a recognised hydrographic chart datum, instead of to a local mean sea level. This correction is performed by subtracting the depth of tide ($d_{tide}$) from $d_2$.

$$d_{lads} = d_2 - d_{tide} \tag{3.14}$$

Tides are measured using tide poles, or using tide gauges. Tide poles have a local datum mark above which the depth of seawater (ie tide) can be measured at regular times. Tide pole measurements are corrected to a Lowest Astronomical Tide (LAT) [26] datum, which is used by the Royal Australian Navy, for chart production.

Tide poles are normally located on jetties or other locations around the coast where measurements can be read conveniently. Tide gauges on the other hand can be deployed in open seawaters and retrieved at later intervals and tide measurements determined. These tide gauges record seawater pressure and therefore allowance must be made for temperature and atmospheric pressure when computing tide values. Tides may also be predicted using a suitable prediction model for specific locations. Tide determined by predictive models require correction for the effects of wind and atmospheric pressure particularly in shallow coastal areas where these effects can cause large tide variations from predicted values.

Corrections for tide are made by subtracting the tide estimate ($d_{tide}$) from the corrected vertical seawater depth (d2), refer to Figure 12.

## 3.10 Summary

This section described the main functions of a typical airborne laser bathymetry system and outlined the signal processing methods used. It described the function of the laser transmitting and receiving systems and the use of a wide angle IR laser beam to detect the sea surface and the use of a scanning narrow blue-green laser beam to probe the seawater and detect the sea bottom.

It described methods of detecting returned laser energy and the signal processing methods used to extract and correct sea depth information.

# 4. Error Analysis of a Typical Airborne Lidar Bathymetry System

## 4.1 The Airborne Laser Bathymetry Measurement Process

An ALB system measures depth by pulsing laser energy downward into the sea and observing the detection times of the reflected laser pulses from the sea surface and the seabed. Then, allowing for system geometry, surface wave action, subtracting accurate tide measurements, depth relative to lowest astronomical tide (LAT) is calculated. In the LADS system, algorithms have been developed to correct for these factors. However residual depth errors still remain. Measurement errors of aircraft height, laser beam scan angle, and others will propagate through the algorithms and contribute to errors in depth estimation. Furthermore, laser pulses are corrupted by noise during their transition time, due to sea surface effects, seawater scattering and absorption, sea bottom reflection characteristics, and system electronics, all resulting in errors in the detection of the position of surface and bottom pulses, and therefore in the measurement of depth.

The following error analysis of the LADS system will estimate the sensitivity of depth accuracy to noise in the raw input data and to limitations in LADS depth data processing algorithms.

## 4.2 Error Analysis Method

A thorough error analysis of the LADS system would be extremely difficult and time consuming because of the complex nature of the signal processing functions. Many processing functions are non-linear and are not always accurately defined analytically, and therefore an analysis of propagation of errors, and of their effect on depth accuracy is an extremely difficult problem. Furthermore, measurements of the absolute signal error, at intermediate stages of the signal processing chain, are not generally available.

Therefore a simplified model of LADS error processes, based on the existing LADS signal processing functions, is proposed, and is illustrated in Figure 13. Here a functional block represents each of the significant signal processing functions. Errors are assumed to be random and statistically independent from block to block, unless otherwise stated. The simplified error model method will estimate error propagation through each functional block in turn, until the errors at the output of the last block are determined.

To achieve this, an error model for a multiple input singular output non-linear function $y=f(a,b,c)$ was developed, refer to Appendix A. Here, $\delta y$ is the error in y due to errors $\delta a$, $\delta b$ and $\delta c$ in a, b and c respectively, at a point of interest $(a_1,b_1,c_1)$, where f(a,b,c) is assumed linear.

The resulting equations are:

$$\delta y = [\partial f(a,b,c)/\partial a]\,\delta a + [\partial f(a,b,c)/\partial b]\,\delta b + [\partial f(a,b,c)/\partial c]\,\delta c \tag{4.1}$$

$$\mu_{\delta y} = \partial f(a,b,c)/\partial a \,|_{a1,b1,c1}\, \mu_{\delta a} + \partial f(a,b,c)/\partial b \,|_{a1,b1,c1}\, \mu_{\delta b} + \partial f(a,b,c)/\partial c \,|_{a1,b1,c1}\, \mu_{\delta c}$$

$$\sigma^2_{\delta y} = (\partial f(a,b,c)/\partial a)^2 \,|_{a1,b1,c1}\, \sigma^2_{\delta a} + (\partial f(a,b,c)/\partial b)^2 \,|_{a1,b1,c1}\, \sigma^2_{\delta b} + (\partial f(a,b,c)/\partial c)^2 \,|_{a1,b1,c1}\, \sigma^2_{\delta c} \tag{4.2}$$

Applying these equations to the system processes, the propagation of error distributions through each functional block in the system can be modelled.

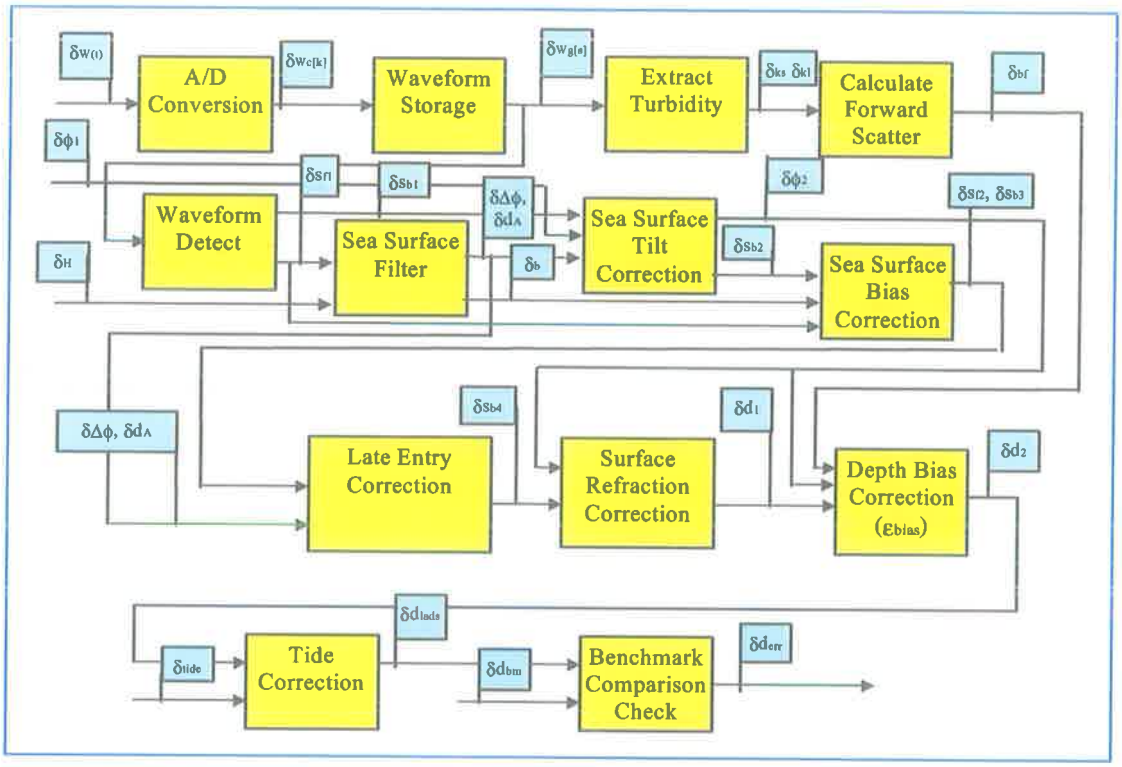


Figure 13: Block diagram of the LADS error processes

However, the propagation of errors through the model relies on valid estimates of the errors at all input stages of the model. Unfortunately, as mentioned previously, no quantitative measure of mean errors within the LADS system is available and only estimates of the standard deviations of the errors can generally be made. Therefore, the simplified error model is only used to calculate the propagation of the variance of error though the system. This approach is considered reasonable, as it will enable the identification of processes within LADS, which result in the occurrence of significant variations in depth error. Further, the application of a linear model is considered acceptable, as LADS processes are relatively linear within their operational regions.

The development of a simplified error model, as applied to LADS processes, follows.

## 4.3 Analogue to Digital Conversion

The process of analogue to digital conversion (ADC) consists of two operations; sampling and quantization. Sampling is the process of defining instantaneous points in time of the data, while quantization is the conversion of the value of the data at sampling time into numerical quantities. Errors occurring in the ADC process can be identified as being due to sampling or aliasings, quantization, aperture timing, timing jitter or other miscellaneous non-linearities [27,p337-342].

In LADS, the detected laser analogue waveforms $w_c(t)$ are digitised by a 6 bit ADC unit, which samples the waveform $w_c(t)$ at 2 ns intervals with a 6 bit resolution for 1024 samples.

$w_c[k] = w_c(t)$, k = 1 to 1024

where

$t = k\Delta t$

$\Delta t = 2ns$

Sampling or aliasing errors occur when the sampling frequency selected in the ADC process is less than twice the highest frequency component in the signal being sampled. In LADS, the sampling frequency of 500 MHz is greater than twice the highest frequency component of the raw data waveforms, and no detectable waveform distortion due to aliasing was apparent in the sampled raw data.

However quantizing errors ($\Delta w_c$) in amplitude, will result in small quantization errors ($\delta t_q$) in pulse detection time, and will be dependant on pulse slope (m) at the quantization point, refer to Figure 14.

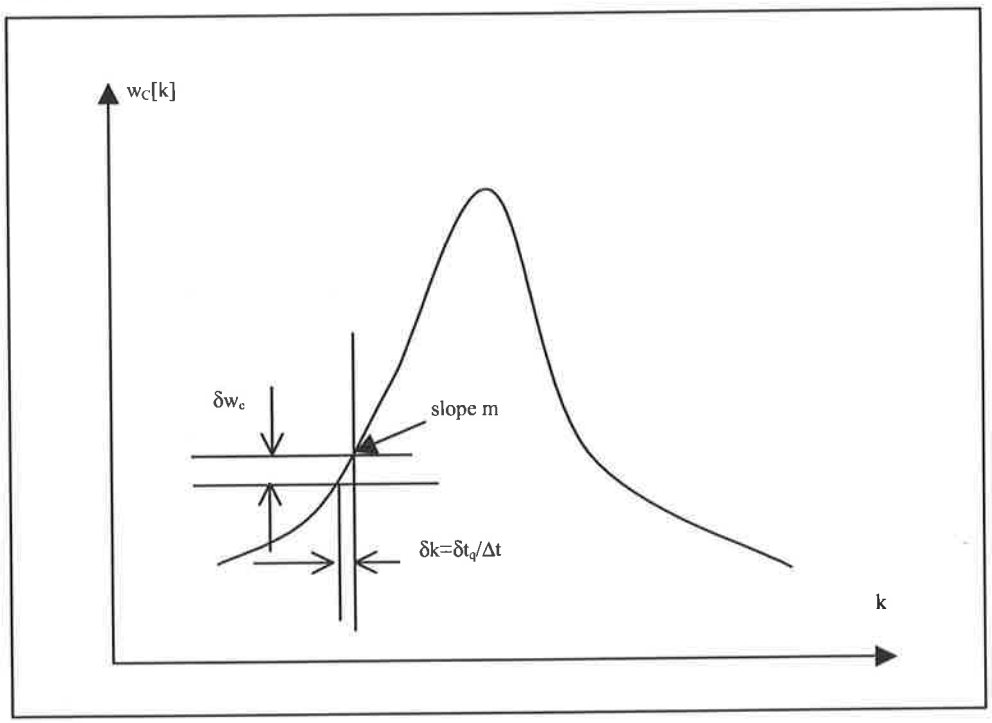


Figure 14: Quantization waveform time errors

Here the quantising increment ($\Delta w_c$) can be estimated [28, p146] as

$$\Delta w_c = fsd/(2^n-1)$$

where fsd is the full scale display value of $w_c$ and n is the number of bits used in the ADC. As the quantising amount ($\Delta w_c$) is equally likely any where within the quantization increment, the mean and standard deviation of $\Delta w_c$ can be estimated [27,p340] as:

$$\mu_{\delta wc} = 0$$
$$\sigma_{\delta wc} = (1/\sqrt{12})(fsd/(2^n-1))$$

which will result in waveform position time errors of:

$$\mu_{\delta tq} = 0$$
$$\sigma_{\delta tq} = (1/\sqrt{12})(fsd/(2^n-1))(\Delta t/m) \quad (4.3)$$

where m is the slope of the composite waveform ($w_c$) at the quantization point.

Evaluating for fsd = 252, n = 6 and m=16/2ns (for a typical bottom pulse), we have:

$$\sigma_{\delta tq} = (1/\sqrt{12})(252/(2^6-1))(2x10^{-9}/16) = 1.443x10^{-10} \text{ s (or} \cong \text{1 cm in depth)}$$

The errors in depth due to quantisation will vary, dependant on the front slope of the bottom pulse, and are of the order of centimetres. The likely maximum depth error of 4 cms, would occur when the smallest likely pulse slope of m=4/2ns occurred.

Another consideration is the effect of aperture errors. The Biomation A/D converter, used in the LADS system, uses high-speed parallel discrete digital logic circuitry and has an estimated aperture error of 100 ps. This will, assuming a worse case of equal probability of occurrence in jitter position, result in small timing errors of

$$\mu_t = 0$$
$$\sigma_t = (1/\sqrt{12})\Delta t = (1/\sqrt{12})100 \text{ ps} = 2.9x10^{-11} \text{ s (or} \cong \text{2 mm in depth)}$$

Aperture errors will result in depth errors less than 1 cm and will be ignored.

There is also an interval trigger delay stability of 3 samples in the Biomation ADC unit, which means that all samples within a given digitized waveform may be shifted together by plus or minus one sample. Because the relative positions of samples (in particular the relative position of surface and bottom pulses to the IR surface reference pulse) within waveforms, will not be altered, no errors in depth determination, due to internal trigger delay stability, will result.

## 4.4 Waveform Storage

The raw waveform $w_r[s]$ is stored as 256 samples, and is displaced in time from the composite waveform $w_c[k]$ by a sample time such that $w_r[15]$ corresponds to the nominal sea surface position detected by the IR beam, refer to section 3.2, where

$$w_r[s] = w_c[s + k_{IR} + \Delta_1 + \Delta_2 - 15], \; s=1 \text{ to } 256 \qquad (4.4)$$

and, referring to section 3.2, we have:

$$s = k - k_{IR} - \Delta_1 - [2H(\sec\Phi_1 - 1)/(c\Delta t)] + 15 \qquad (4.5)$$

Thus any errors, $\delta k_{IR}$, $\delta H$ and $\delta\phi$ which occur in the measurement of $k_{IR}$, H and $\phi_1$, will result in errors $\delta s$ in the position s of the sampled waveform $w_r[s]$, and therefore to errors in the calculation of depth.

The error in the measurement of $k_{IR}$, will occur due to abnormal wave peaks, wave spray or because of the detection sensitivity of the IR receiver and will result in errors $\delta s$ in the time position of individual raw waveforms. Note this error is considered distinct from those corrected by the filtered average sea surface bias discussed in section 4.6, where a filtered average difference between the detected green surface returns and the IR surface returns, is used to measure and correct a sea surface bias.

Now applying equation (4.1) to (4.5) we have:

$$\delta s = (\partial s/\partial k_{IR})\delta k_{IR} + (\partial s/\partial H)\delta H + (\partial s/\partial \Phi_1)\delta \Phi_1$$

$$= -\delta k_{IR} - [2(\sec\Phi_1 - 1)/(c\Delta t)]\delta H - [(2H/c\Delta t)(\sec^2\Phi_1)(\sin\Phi_1)]\delta\Phi_1$$

and, applying equations (4.2), we have:

$$\mu_{\delta s} = -\mu_{\delta kIR} - [2(\sec\Phi_1 - 1)/(c\Delta t)]\mu_{\delta H} - [(2H/c\Delta t)(\sec^2\Phi_1)(\sin\Phi_1)]\mu_{\delta\Phi 1}$$

$$\sigma^2_{\delta s} = \sigma^2_{\delta kIR} + [2(\sec\Phi_1 - 1)/(c\Delta t)]^2\sigma^2_{\delta H} + [(2H/c\Delta t)(\sec^2\Phi_1)(\sin\Phi_1)]^2\,\sigma^2_{\delta\Phi 1} \qquad (4.6)$$

The conversion of composite waveforms into 256 sample raw waveforms has the potential for error. Any error $\delta k_{IR}$ in the position of the IR surface will be directly transferable to the position of the raw waveform and therefore to the ALB system depth. Also any error $\delta\Phi_1$ in the measurement of the scan angle $\Phi_1$ will have the potential to cause a significant error $\delta s$ for large scan angles and therefore in system depth.

## 4.5 Waveform Detection

The waveform detection process detects the 50% pulse location of the sea surface ($s_{f1}$) and the 50% pulse location of the sub-surface ($s_{b1}$) reflections relative to the nominal IR surface reference, refer to sections 3.3.1 and 3.3.2. In LADS the 50% pulse time detection points are determined by linear interpolation between waveform sample points. There is a storage time error ($\delta s$) associated with every raw waveform position, a quantization time error ($\delta t_q$) associated with each waveform sample point and a time error ($\delta t_l$) associated with the linear interpolation process, refer to Figure 15. Here the maximum absolute value of $\delta t_1$ is dependant on the curvature of the waveform and is assumed to be of the order of 1/10 of one sample time (2 ns). Also, it was noted from results data, that the curvature of the waveform at the 50% detection point is equally likely to be convex or concave. Therefore, assuming that $E\{\delta t_1\}=0$ and the magnitude of $\delta t_1$ is equally likely between 0 and 0.2 ns we have:

$$\mu_{\delta t1} = 0$$
$$\sigma_{\delta t1} = (0.1)(1\sqrt{12})\,\Delta t \qquad (4.7)$$

and

$$\sigma_{\delta t1} = (0.1)(1/\sqrt{12})(2\text{x}10^{-9}) = 5.77\text{x}10^{-11}\ \text{s}\ \ (\text{or} \cong 4\ \text{mm})$$

Now, for the calculation of a surface pulse detection error ($\delta s_{f1}$) and referring to Figure 15, we have a waveform position input error ($\delta s$), a linear interpolation input error ($\delta t_1$), and two point quantization input errors ($\delta t_{qs1}$ , $\delta t_{qs2}$).

Also for the calculation of a bottom pulse detection error ($\delta s_{b1}$) we have input errors of $\delta s$, $\delta t_1$, $\delta t_{qb1}$ and $\delta t_{qb2}$.

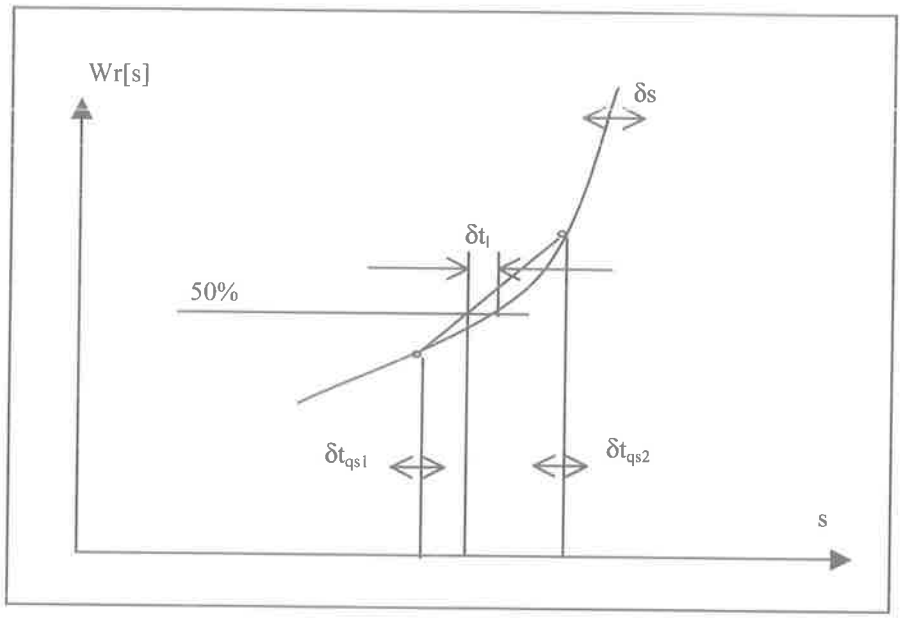


Figure 15: Pulse position error diagram

Now, the errors in determining $s_{fl}$ and $s_{bl}$ can be estimated in metres as:

$$\delta s_{fl} = (c\Delta t/2\eta_w)\delta s + (c/2\eta_w)\delta t_{qs1} + (c/2\eta_w)\delta t_{qs2} + (c/2\eta_w)\delta_{tl}$$
$$\delta s_{bl} = (c\Delta t/2\eta_w)\delta s + (c/2\eta_w)\delta t_{qb1} + (c/2\eta_w)\delta t_{qb2} + (c/2\eta_w)\delta_{tl}$$

Therefore, assuming that $E\{\delta t_{qs1}\} = E\{\delta t_{qs2}\} = E\{\delta t_{qb1}\} = E\{\delta t_{qb2}\} = E\{\delta t_1\} = 0$

and applying equations (4.2), we have:

$$\mu_{\delta sfl} = (c\Delta t/2\eta_w)\,\mu_{\delta s}$$
$$\mu_{\delta sbl} = (c\Delta t/2\eta_w)\,\mu_{\delta s}$$

$$\sigma^2_{\delta sfl} = (c\Delta t/2\eta_w)^2\,\sigma^2_{\delta s} + (c/2\eta_w)^2\sigma^2_{\delta tqs1} + (c/2\eta_w)^2\sigma^2_{\delta tqs2} + (c/2\eta_w)^2\sigma^2_{\delta tl} \quad (4.8)$$
$$\sigma^2_{\delta sbl} = (c\Delta t/2\eta_w)^2\,\sigma^2_{\delta s} + (c/2\eta_w)^2\sigma^2_{\delta tqb1} + (c/2\eta_w)^2\sigma^2_{\delta tqb2} + (c/2\eta_w)^2\sigma^2_{\delta tl}$$

where $\sigma_{\delta s}$ is given by equation (4.6), $\sigma_{\delta tqs1}$, $\sigma_{\delta tqs12}$, $\sigma_{\delta tqb1}$and $\sigma_{\delta tqb2}$ is given by equation (4.3), and $\sigma_{\delta tl}$ is given by equation (4.7).

Generally the waveform detection process will not cause significant depth errors as quantization errors $\delta t_q$ and interpolation errors $\delta t_1$ introduce errors of the order of 2 mm and 4 mm respectively, refer sections 4.3 and 4.5.

## 4.6 Sea Surface Filter Calculation

The sea surface position ($s_{fl}$) is filtered, refer to section 3.4, to estimate bias (b) and tilt ($\Delta\Phi$) errors in the sea surface. These parameters are used to correct surface and bottom pulse positions, refer to section 3.5, to improve the resulting depth accuracy of the LADS system.

The sensitivity of errors in the filter output variables (b and $\Delta\Phi$) to errors in the surface position ($s_{fl}$) and scan angle ($\Phi_1$), is determined in Appendix B, and can be estimated from the

following equations, where R is a reduction factor to account for the filtering effect of the sea surface filter:

$$\delta b = R\,[\cos(\Phi_1+\Delta\Phi)]\,\delta s_{fl} + R\,[H\sin\Phi_1\cos(\Phi_1+\Delta\Phi)/\cos^2\Phi_1 - (s_{fl} - s_{wave} + H/\cos\Phi_1)\sin(\Phi_1+\Delta\Phi)\,]\,\delta\Phi_1$$

$$\delta\Delta\Phi = R\,[(H+b)/((s_{fl}-s_{wave}+H/\cos\Phi_1)((s_{fl}-s_{wave}+H/\cos\Phi_1)^2-(H+b)^2)^{1/2})]\,\delta s_{fl} + R\,[H(H+b)\sin(\Phi_1)/(\cos^2\Phi_1(s_{fl}-s_{wave}+H/\cos\Phi_1)((s_{fl}-s_{wave}+H/\cos\Phi_1)^2-(H+b)^2)^{1/2})]\,\delta\Phi_1$$

and applying equations (4.2) we have:

$$\mu_{\delta b} = R\,[\cos(\Phi_1+\Delta\Phi)]\,\mu_{\delta sfl} + R\,[H\sin\Phi_1\cos(\Phi_1+\Delta\Phi)/\cos^2\Phi_1 - (s_{fl} - s_{wave} + H/\cos\Phi_1)\sin(\Phi_1+\Delta\Phi)\,]\,\mu_{\delta\Phi 1}$$

$$\mu_{\delta\Delta\Phi} = R\,[(H+b)/((s_{fl}-s_{wave}+H/\cos\Phi_1)((s_{fl}-s_{wave}+H/\cos\Phi_1)^2-(H+b)^2)^{1/2})]\,\mu_{\delta sfl} + R\,[H(H+b)\sin(\Phi_1)/(\cos^2\Phi_1(s_{fl}-s_{wave}+H/\cos\Phi_1)((s_{fl}-s_{wave}+H/\cos\Phi_1)^2-(H+b)^2)^{1/2})]\,\mu_{\delta\Phi 1} \quad (4.9)$$

$$\sigma^2_{\delta b} = R^2\,[\cos(\Phi_1+\Delta\Phi)]^2\,\sigma^2_{\delta sfl} + R^2\,[H\sin\Phi_1\cos(\Phi_1+\Delta\Phi)/\cos^2\Phi_1 - (s_{fl} - s_{wave} + H/\cos\Phi_1)\sin(\Phi_1+\Delta\Phi)\,]^2\,\sigma^2_{\delta\Phi 1}$$

$$\sigma^2_{\delta\Delta\Phi} = R^2\,[(H+b)/((s_{fl}-s_{wave}+H/\cos\Phi_1)((s_{fl}-s_{wave}+H/\cos\Phi_1)^2-(H+b)^2)^{1/2})]^2\,\sigma^2_{\delta sfl} + R^2\,[H(H+b)\sin(\Phi_1)/(\cos^2\Phi_1(s_{fl}-s_{wave}+H/\cos\Phi_1)((s_{fl}-s_{wave}+H/\cos\Phi_1)^2-(H+b)^2)^{1/2})]^2\,\sigma^2_{\delta\Phi 1}$$

Generally, it can be assumed that the errors in the estimation of $\Delta\Phi$ and b are small. In smooth seas the error in the estimation of b is negligible, as the averaged position of the green laser surface reflections correspond with the positions of the IR laser surface reflections. But with increasing sea roughness the error in the estimation of b would be expected to increase, as the distortion in the surface pulses will usually result in larger errors in the positions $s_{fl}$ of the green laser surface reflections. In smooth seas however, the error in the estimation of $\Delta\Phi$ will depend on how accurately the surface position and laser beam scan angle are measured. In smooth seas, valid surface returns usually occur at small scan angles, and as the sensitivity of tilt estimation to surface position is higher at small scan angles, then small errors in the estimation of tilt can result.

## 4.7 Sea Surface Tilt Correction

Surface position ($s_{fl}$), sub surface position ($s_{bl}$) and scan angle ($\Phi_1$ ) are both corrected for tilt ($\Delta\Phi$) as follows, refer to section 3.5.

$$s_{f2} = s_{fl} - (H/\eta_w)\,(\sin\Phi_1/\cos^2\Phi_1)\,\Delta\Phi$$
$$s_{b2} = s_{bl} - (H/\eta_w)\,(\sin\Phi_1/\cos^2\Phi_1)\,\Delta\Phi$$
$$\Phi_2 = \Phi_1 + \Delta\Phi$$

Now considering the errors $\delta s_{fl}$, $\delta s_{bl}$, $\delta\Phi_1$ and $\delta\Delta\Phi$ in $s_{fl}$, $s_{bl}$, $\Phi_1$ and $\Delta\Phi$ respectively, and substituting into equations (4.1) we get:

$$\delta s_{f2} = \delta s_{fl} - [(H/\eta_w)\,(1/\cos\Phi_1 + 2\sin^2\Phi_1/\cos^3\Phi_1)\,(\Delta\Phi)]\,\delta\Phi_1 - [(H/\eta_w)\,(\sin\Phi_1/\cos^2\Phi_1)]\,\delta\Delta\Phi$$

$$\delta s_{b2} = \delta s_{b1} - [(H/\eta_w)\,(1/\cos\Phi_1 + 2\sin^2\Phi_1/\cos^3\Phi_1)\,(\Delta\Phi)]\,\delta\Phi_1 - [(H/\eta_w)\,(\sin\Phi_1/\cos^2\Phi_1)]\,\delta\Delta\Phi$$
$$\delta\Phi_2 = \delta\Phi_1 + \delta\Delta\Phi \qquad (4.10)$$

and applying the error model equations (4.2) we obtain:

$$\mu_{\delta sf2} = \mu_{\delta sf1} - [(H/\eta_w)\,(1/\cos\Phi_1 + 2\sin^2\Phi_1/\cos^3\Phi_1)\,(\Delta\Phi)]\,\mu_{\delta\Phi 1} - [(H/\eta_w)\,(\sin\Phi_1/\cos^2\Phi_1)]\,\mu_{\delta\Delta\Phi}$$
$$\mu_{\delta sb2} = \mu_{\delta sb1} - [(H/\eta_w)\,(1/\cos\Phi_1 + 2\sin^2\Phi_1/\cos^3\Phi_1)\,(\Delta\Phi)]\,\mu_{\delta\Phi 1} - [(H/\eta_w)\,(\sin\Phi_1/\cos^2\Phi_1)]\,\mu_{\delta\Delta\Phi}$$
$$\mu_{\delta\Phi 2} = \mu_{\delta\Phi 1} + \mu_{\delta\Delta\Phi}$$

$$\sigma^2_{\delta sf2} = \sigma^2_{\delta sf1} + [(H/\eta_w)\,(1/\cos\Phi_1 + 2\sin^2\Phi_1/\cos^3\Phi_1)\,(\Delta\Phi)]^2\,\sigma^2_{\delta\Phi 1} + [(H/\eta_w)\,(\sin\Phi_1/\cos^2\Phi_1)]^2\,\sigma^2_{\delta\Delta\Phi}$$
$$\sigma^2_{\delta sb2} = \sigma^2_{\delta sb1} + [(H/\eta_w)\,(1/\cos\Phi_1 + 2\sin^2\Phi_1/\cos^3\Phi_1)\,(\Delta\Phi)]^2\,\sigma^2_{\delta\Phi 1} + [(H/\eta_w)\,(\sin\Phi_1/\cos^2\Phi_1)]^2\,\sigma^2_{\delta\Delta\Phi}$$
$$\sigma^2_{\delta\Phi 2} = \sigma^2_{\delta\Phi 1} + \sigma^2_{\delta\Delta\Phi} \qquad (4.11)$$

It can be seen from the above equations, that the sea surface tilt correction process will propagate any error $\Delta\Phi$ in tilt, into the positions of the sea surface $s_{f2}$ and sea bottom $s_{b2}$, the propagated error becoming larger with increasing scan angles. The sea surface tilt correction process will also transfer tilt error into the corrected scan angle $\Phi_2$.

## 4.8 Sea Surface Bias Correction

The surface position ($s_{f1}$) and the sub surface position ($s_{b2}$) are corrected for sea surface bias (b), using the following expressions, refer to section 3.5.

$$s_{f3} = s_{f2} - b$$
$$s_{b3} = s_{b2} - b$$

from which it directly follows that

$$\mu_{\delta sf3} = \mu_{\delta sf2} - \mu_{\delta b}$$
$$\mu_{\delta sb3} = \mu_{\delta sb2} - \mu_{\delta b}$$

$$\sigma^2_{\delta sf3} = \sigma^2_{\delta sf2} + \sigma^2_{\delta b}$$
$$\sigma^2_{\delta sb3} = \sigma^2_{\delta sb2} + \sigma^2_{\delta b} \qquad (4.12)$$

Here, it can be seen that the sea surface bias correction process will transfer any error in the determined sea surfacc bias b, directly into the corrected positions of the sea surface $s_{f3}$ and the sea bottom $s_{b3}$.

## 4.9 Late Entry Correction

The late entry correction process corrects for the difference in speed of the laser beam in air compared with its speed in seawater, refer to section 3.6. Thus, when a late surface reflection is detected, the sub surface distance $s_{b3}$ is corrected for late entry to the sub surface distance $s_{b4}$, by the following expression, where $s_{f3}$ is positive.

$$s_{b4} = s_{b3} + (1 - 1/\eta_w)\, s_{f3}$$

Thus

$$\delta s_{b4} = \delta s_{b3} + (1-1/\eta_w)\, \delta s_{f3}$$

and applying the error model we have:

$$\mu_{\delta sb4} = \mu_{\delta sb3} + [1-1/\eta_w]\, \mu_{\delta sf3}$$

$$\sigma^2_{\delta sb4} = \sigma^2_{\delta sb3} + [1-1/\eta_w]^2\, \sigma^2_{\delta sf3} \qquad (4.13)$$

In the late entry correction process, any error in the estimate of the corrected surface position $s_{f3}$ (ie of the wave trough), is reduced by the factor $(1-1/\eta_w)$, which is approximately ¼,when propagated into the bottom position $s_{b4}$. In general this correction will be insignificant, particularly for smooth seas, where the error in $s_{f3}$ is generally small.

However, whenever a valid surface waveform is not detected, this correction will not be applied, and an error equal to ¼ of the wave trough will occur, and the depth $s_{b4}$ will be shallow by that amount. This situation often occurs in calm seas for non-nadir scan angles, where the scanning green laser beam is reflected away for the airborne receiver field of view. Fortunately in calm seas, wave heights are small and any errors, from not applying the late entry correction, would be minor.

## 4.10 Surface Refraction Correction

The sub surface distance $s_{b4}$ is corrected, for surface refraction, to vertical depth $d_1$ by the following expression, refer to section 3.7.

$$d_1 = s_{b4} \sqrt{(1-(\sin\Phi_2/\eta_w)^2)}$$

The error $(\delta d_1)$ in $d_1$ due to errors $(\delta s_{b4}, \delta\Phi_2)$ in $s_{b4}$ and $\Phi_2$ can be calculated as follows.

$$\delta d_1 = \sqrt{[1 - (\sin\Phi_2/\eta_w)^2]}\, \delta s_{b4} - [(s_{b4}/n^2_w)\, (\sin\Phi_2.\cos\Phi_2)/(\sqrt{(1 - (\sin\Phi_2/\eta_w)^2)})]\, \delta\Phi_2$$

and applying the error model we have:

$$\mu_{\delta d1} = \sqrt{[1 - (\sin\Phi_2/\eta_w)^2]}\, \mu_{\delta sb4} - [(s_{b4}/n^2_w)\, (\sin\Phi_2.\cos\Phi_2)/(\sqrt{(1 - (\sin\Phi_2/\eta_w)^2)})]\, \mu_{\delta\Phi 2}$$

$$\sigma^2_{\delta d1} = [1 - (\sin\Phi_2/\eta_w)^2]\, \sigma^2_{\delta sb4} + [(s_{b4}/n^2_w)\, (\sin\Phi_2.\cos\Phi_2)/(\sqrt{(1 - (\sin\Phi_2/\eta_w)^2)})]^2\, \sigma^2_{\delta\Phi 2} \qquad (4.14)$$

In the surface refraction correction process and errors in bottom position $s_{b4}$ and in scan angle $\Phi_2$ will result in errors in the estimation of depth $d_1$. Any errors in $s_{b4}$ propagate into $d_1$ particularly for small $\Phi_2$, while any errors in $\Phi_2$ propagate into $d_1$ only becoming significant as $\Phi_2$ becomes larger.

Note that this correction assumes a horizontal sea surface at the point of refraction. Wave action will affect the angle of refraction and because the scanning green beam has a 3 m diameter footprint at the sea surface, the beam will be refracted in numerous directions. In rough seas therefore, we can expect some contribution to depth error because the sea surface at the point of

refraction is not likely to be horizontal. However, in smooth seas, the sea surface is likely to be horizontal, and therefore little or no error would be expected from the surface refraction process.

## 4.11 Turbidity Extraction

Attenuation coefficients ($k_S$ and $k_L$) are determined by regression analysis of the backscatter region of the sampled raw extremity waveform ($w_r[s]$), refer to section 3.3.3. For any given waveform the mean error of fit is considered to be zero, and the standard deviation in the fit of each waveform is computed to provide an indication in the accuracy of the estimation of the coefficients.

Values of $k_L$, $k_S$, $\sigma_{\delta kL}$ and $\sigma_{\delta kS}$ vary with seawater turbidity, as shown in Figure 16.

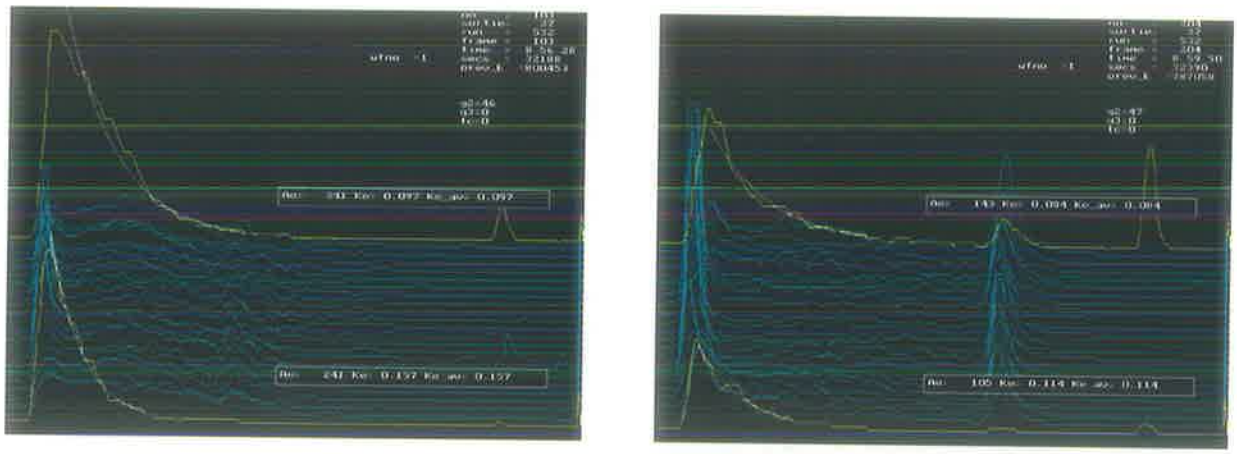

(a) Turbid seawater at 18 m depth (b) Clear seawater at 30 m depth

Figure 16 Turbidity measurements for clear and turbid seawater

Figure 16 (a) shows the results of a single scan of 24 waveforms at a depth of 18 m. As previously explained only the constant gain extremity waveforms are used to measure attenuation coefficients. For this scan the fitted exponential curves are shown highlighted and the resultant coefficients are $k_S = 0.157$ and $k_L = 0.097$. Note the attenuation of the bottom return pulses, which indicates significant seawater turbidity.

Figure 16 (b) similarly shows the results of a single scan of 24 waveforms for clear seawater at a depth of 30 m. Note here the bottom pulses are clearly visible even at a deeper depth. The resultant measured coefficients are $k_S = 0.114$ and $k_L = 0.084$.

Further results were taken at these two locations to obtain average values. The results are shown in table 1 where the sample mean and standard deviation were computed for 10 samples.

| Frame no | k_S (turbid | k_L (turbic | Frame no | k_S (clear) | k_L (clear |
|---|---|---|---|---|---|
| 100 | 0.163 | 0.083 | 201 | 0.080 | 0.072 |
| 101 | 0.163 | 0.097 | 203 | 0.102 | 0.077 |
| 102 | 0.165 | 0.093 | 204 | 0.114 | 0.084 |
| 103 | 0.157 | 0.097 | 205 | 0.110 | 0.072 |
| 104 | 0.168 | 0.094 | 206 | 0.122 | 0.090 |
| 105 | 0.162 | 0.092 | 209 | 0.096 | 0.064 |
| 106 | 0.157 | 0.105 | 210 | 0.116 | 0.083 |
| 108 | 0.175 | 0.106 | 211 | 0.148 | 0.090 |
| 109 | 0.160 | 0.100 | 212 | 0.102 | 0.085 |
| 111 | 0.176 | 0.104 | 213 | 0.103 | 0.076 |
| Sum | 1.646 | 0.971 | Sum | 1.093 | 0.793 |
| Mean | 0.165 | 0.097 | Mean | 0.109 | 0.079 |
| std | 0.00665 | 0.00706 | std | 0.0179 | 0.00853 |

Table 1 Attenuation Coefficient Values for Turbid and Clear Seawater

The results for turbid seawater at 18 m were $\bar{k}_S = 0.165$ $s_{kS} = 0.00665$ $\bar{k}_L = 0.097$ $s_{kL} = 0.00706$ and for clear seawater at 30 m were $\bar{k}_S = 0.109$ $s_{kS} = 0.00179$ $\bar{k}_L = 0.079$ $s_{kL} = 0.00853$.

In general these results show the coefficients become smaller with clear seawater and the value of the smaller FOV coefficient is larger than that of the large FOV coefficient. Also there is less variation in the measurements of the coefficients in turbid seawater and less variation in the measurement of the large FOV coefficients.

The difference between the small and large coefficients is a measure of seawater turbidity. In clear seawater, where there is little spreading of the laser beam, the difference in energy detected between the large and small FOV receiver is small, when compared with that for turbid seawater, where photon scattering results in a larger spreading of the laser beam. The results previously obtained, support this giving a larger value for turbid seawater than for clear seawater. In particular $k_S - k_L = 0.165\text{-}0.097 = 0.068$ for turbid seawater and $= 0.109\text{-}.079 = 0.030$ for clear seawater. However, in LADS a more sophisticated model of forward scatter was used, refer section 4.12.

The above attenuation coefficient results were input into the forward scatter and depth bias models described in sections 4.12 and 4.13 to allow the modelling of the depth bias correction process.

## 4.12 Forward Scatter Determination

A forward scatter coefficient ($b_f$) is calculated as a function, of small and large field of view coefficients ($k_S$, $k_L$).

$$b_f = f(k_S, k_L)$$

This function is described in [1] and its form was used in deriving the results reported in section 4.17. However as it is classified as Commercial in Confidence, it is not detailed here.

The error ($\delta b_f$) in $b_f$ can be estimated from errors ($\delta k_S$, $\delta k_L$) in the estimate of $k_S$ and $k_L$, giving $\mu_{\delta bf}$ and $\sigma^2_{\delta bf}$ as follows:

$$\mu_{\delta bf} = (\partial b_f / \partial k_S)\, \mu_{\delta kS} + (\partial b_f / \partial k_L)\, \mu_{\delta kL} + \mu_{Ebf}$$

$$\sigma^2_{\delta bf} = (\partial b_f / \partial k_S)^2\, \sigma^2_{\delta kS} + (\partial b_f / \partial k_L)^2\, \sigma^2_{\delta kL} + \sigma^2_{Ebf} \qquad (4.15)$$

The error term ($E_{bf}$) is provided to allow for the imperfections of the forward scatter model.

The errors in the measurement of the attenuation coefficients $k_S$ and $k_L$, together with the error in the forward scatter model $E_{bf}$, are transmitted into the estimation of the forward scatter coefficient $b_f$.

## 4.13 Depth Bias Correction

Correction to vertical depth ($d_1$) to estimate vertical depth ($d_2$) is made by a depth bias model, refer to section 3.8, where:

$$d_2 = d_1 - d_{bias}(d_1, \Phi_2) + E_{bias} \quad \text{or} \quad d_2 = d_1 - d_{bias}(d_1, \Phi_2, b_f) + E_{bias}$$

which results in

$$\mu_{\delta d2} = \mu_{\delta d1} - (\partial d_{bias}/\partial d_1)\, \mu_{\delta d1} - (\partial d_{bias} / \partial \Phi_2)\, \mu_{\delta \Phi 2} - (\partial d_{bias} / \partial b_f)\, \mu_{\delta bf} + \mu_{Ebias}$$

$$\sigma^2_{\delta d2} = \sigma^2_{\delta d1} + (\partial d_{bias} / \partial d_1)^2\, \sigma^2_{\delta d1} + (\partial d_{bias} / \partial \Phi_2)^2\, \sigma^2_{\delta \Phi 2} + (\partial d_{bias} / \partial b_f)^2\, \sigma^2_{\delta bf} + \sigma^2_{Ebias} \qquad (4.16)$$

where $d_{bias}(.)$ is the correction applied to compensate for the seawater scattering effect on the green laser beam and $E_{bias}$ is the error introduced by the depth bias model.

Note that, as mentioned previously in section 3.8, the depth bias models are classified Commercial in Confidence and are not disclosed in this thesis.

## 4.14 Tide Correction

Vertical depth ($d_2$) is corrected for tide, to determine LADS depth ($d_{lads}$) relative to LAT, refer to section 3.9.

$$d_{lads} = d_2 - d_{tide}$$

from which it directly follows that

$$\mu_{\delta dlads} = \mu_{\delta d2} - \mu_{\delta dtide}$$

$$\sigma^2_{\delta dlads} = \sigma^2_{\delta d2} + \sigma^2_{\delta dtide} \qquad (4.17)$$

Here any errors in depth $d_2$ and tide $d_{tide}$ will be transferred directly into the error in the determination of the ALB system depth $d_{lads}$.

## 4.15 Bench Mark Comparison

Benchmark comparison results are used to check on the depth accuracy of Airborne Laser Bathymetry systems. The benchmark comparison process first interpolates benchmark depths

onto a rectangular grid. Then a linear interpolation of the three nearest benchmark grid depths to the selected ALB depth is performed, before a depth comparison can be made. The error in this process is accounted for by an $E_{bmc}$ term, included in the equations below. A flat seabed area is normally selected for the benchmark depth area, to minimize the error $E_{bmc}$ in the benchmark comparison process.

The benchmark comparison results ($d_{err}$), are calculated by subtracting the interpolated benchmark depths ($d_{bm}$) from the corresponding ALB depths ($d_{lads}$) as formulated below, where $E_{bmc}$ is the error introduced by the benchmark comparison process.

$$d_{err} = d_{lads} - d_{bm} + E_{bmc}$$

from which it follows that:

$$\mu_{\delta derr} = \mu_{\delta dlads} - \mu_{\delta dbm} + \mu_{Ebmc} \cong 0$$

$$\sigma^2_{\delta derr} = \sigma^2_{\delta dlads} + \sigma^2_{\delta dbm} + \sigma^2_{Ebmc} \qquad (4.18)$$

The resulting mean error ($\mu_{\delta derr}$) will generally be close to zero, because of the corrections made by the depth bias model. The depth bias model was developed, using a least squares method, to minimize $d_{err}$ for a given set of data. The resulting standard deviation error ($\sigma_{\delta derr}$) is a measure of the variation in $d_{err}$ to given errors of input or measurement. Previous work [29] has measured the overall standard deviation of the LADS system (for a selected set of trial data) as:

$$\sigma_{\delta derr} = 0.10\text{m } (d_{lads}=10\text{m}),\ 0.18\text{m } (d_{lads}=20\text{m}),\ 0.25\text{m } (d_{lads}=30\text{m})$$

## 4.16 Assumptions used

The error model, developed here in chapter 4 and summarised in Appendix A, assumes the propagation of stationary random error variables for simplification. The independence of process variables is also assumed as well as the linearity of process functions in the region of their use. The assumption of linearity is considered acceptable, because in general, process functions are approximately linear in their operating regions especially for small changes in variables.
The model also requires the input of a number of system measurement errors and system parameters, to predict the resultant output depth errors. Because the measurements of absolute errors in the system are not readily available and are difficult to estimate, only the propagation of error variances is performed. This use of the model is considered appropriate, as the prediction of the sensitivity of the ALB system depth accuracy to data and processing errors is required, and the variance in the output depth error($d_{err}$) is an indicator of system accuracy.

The error in the values of $k_L$, $k_S$, $\sigma_{\delta kL}$ and $\sigma_{\delta kS}$ vary with seawater turbidity, being small in clear seawater and becoming larger with increasing seawater turbidity, as discussed previously in section 4.11. Typical values for average seawater conditions are, $k_L$=0.060, $k_S$=0.085 with $\sigma_{\delta kL} \cong 10\%$ of $k_L$ and $\sigma_{\delta ks} \cong 10\%$ of $k_S$.

The accuracy in the measurement of tide depends upon the measurement method used, as mentioned in section 3.9. With careful measurement, the standard deviation error ($\sigma_{\delta dtide}$) in the measurement of tide is likely to be 0.1m.

It should be noted, the accuracy of benchmark depths is dependent on how well the benchmark survey was done. In the past, it has proved difficult to achieve consistent benchmark results. Furthermore the benchmark comparison process is far from ideal as benchmark depths are first interpolated onto a rectangular grid before comparing with LADS depths. This results in a two-stage interpolation, which is prone to errors. For a well-surveyed benchmark, the std error ($\sigma_{\delta dbm}$) in the benchmark depths is assumed to be 0.15m, and the std error ($\sigma_{\delta Ebmc}$) in the benchmark comparison process is assumed to be 0.05m.

The resultant error model is summarized in Appendix A.

## 4.17 Results

The error model was programmed for 39 experiments for the conditions listed in table 2 over page, where $\sigma_{dtide} = 0$, $\sigma_{dbm}=0$ and $\sigma_{Ebmc} = 0$, except for experiment no 19 where $\sigma_{dtide} = 0.1$m, $\sigma_{dbm} = 0.15$m, $\sigma_{Ebmc} = 0.05$m, and the resulting std errors in depth $\sigma_{derr}$ are plotted in Figure 17 below.

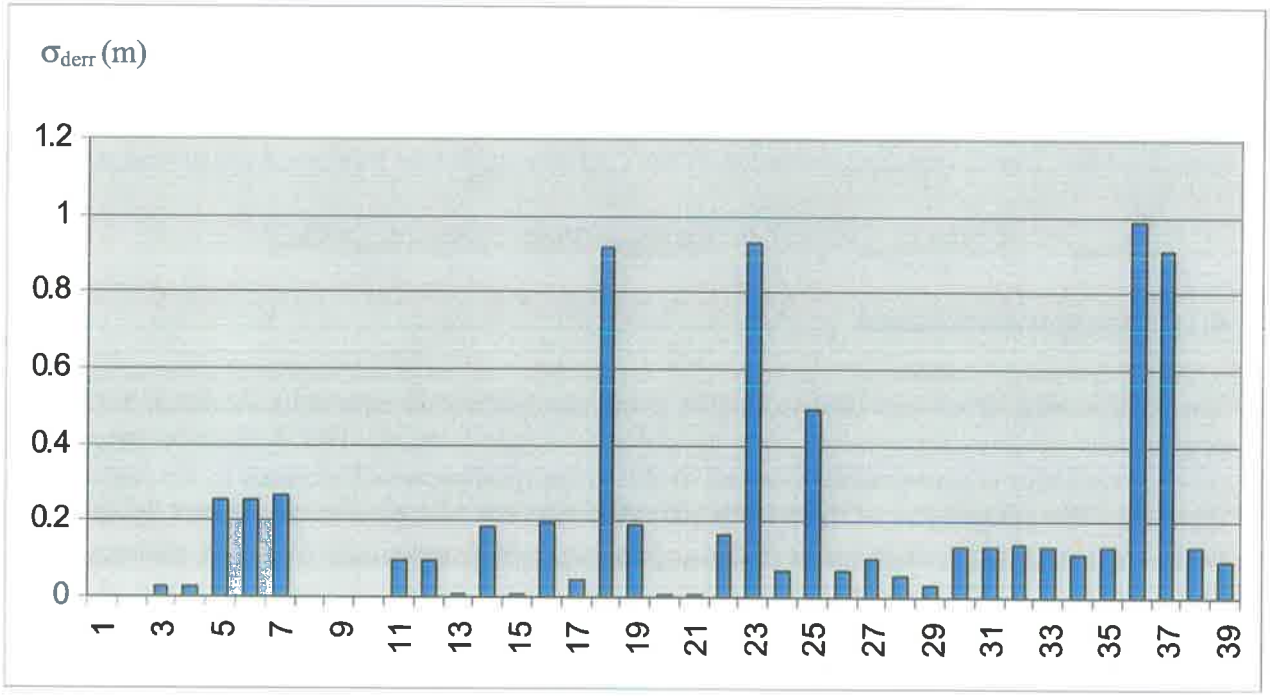


Figure 17 Results of the Simplified Error Model

| No | $\sigma_h$ | $\sigma_{kIR}$ | $m_s$ | $m_b$ | $\Phi_1$ | $s_{f1}$ | $s_{b1}$ | $\sigma_{\Phi 1}$ | b | $\Delta\Phi$ | $k_S$ | $k_L$ | $\sigma_{kS}$ | $\sigma_{kL}$ | $\sigma_{derr}$ |
|---|---|---|---|---|---|---|---|---|---|---|---|---|---|---|---|
| 1 | 0 | 0 | ∞ | ∞ | 0.652 | 0 | 30 | 0 | 0 | 0 | 0.15 | 0.09 | 0 | 0 | 0.011 |
| 2 | 1 | 0 | ∞ | ∞ | 0.652 | 0 | 30 | 0 | 0 | 0 | 0.15 | 0.09 | 0 | 0 | 0.011 |
| 3 | 1 | 0 | ∞ | ∞ | 13.7 | 0 | 30 | 0 | 0 | 0 | 0.15 | 0.09 | 0 | 0 | 0.037 |
| 4 | 1 | 0 | ∞ | ∞ | 13.7 | 0 | 50 | 0 | 0 | 0 | 0.15 | 0.09 | 0 | 0 | 0.040 |
| 5 | 0 | 1 | ∞ | ∞ | 0.652 | 0 | 30 | 0 | 0 | 0 | 0.15 | 0.09 | 0 | 0 | 0.370 |
| 6 | 0 | 1 | ∞ | ∞ | 13.7 | 0 | 30 | 0 | 0 | 0 | 0.15 | 0.09 | 0 | 0 | 0.366 |
| 7 | 0 | 1 | ∞ | ∞ | 13.7 | 0 | 50 | 0 | 0 | 0 | 0.15 | 0.09 | 0 | 0 | 0.39 |
| 8 | 0 | 0 | 70 | ∞ | 0.652 | 0 | 30 | 0 | 0 | 0 | 0.15 | 0.09 | 0 | 0 | 0.011 |
| 9 | 0 | 0 | 70 | ∞ | 13.7 | 0 | 30 | 0 | 0 | 0 | 0.15 | 0.09 | 0 | 0 | 0.011 |
| 10 | 0 | 0 | 70 | 30 | 0.652 | 0 | 30 | 0 | 0 | 0 | 0.15 | 0.09 | 0 | 0 | 0.011 |
| 11 | 0 | 0 | 70 | 1 | 0.652 | 0 | 30 | 0 | 0 | 0 | 0.15 | 0.09 | 0 | 0 | 0.094 |
| 12 | 0 | 0 | 70 | 1 | 13.7 | 0 | 30 | 0 | 0 | 0 | 0.15 | 0.09 | 0 | 0 | 0.094 |
| 13 | 0 | 0 | ∞ | ∞ | 0.652 | 0 | 30 | 0.1 | 0 | 0 | 0.15 | 0.09 | 0 | 0 | 0.018 |
| 14 | 0 | 0 | ∞ | ∞ | 13.7 | 0 | 30 | 0.1 | 0 | 0 | 0.15 | 0.09 | 0 | 0 | 0.317 |
| 15 | 0 | 0 | ∞ | ∞ | 0.652 | 0 | 50 | 0.1 | 0 | 0 | 0.15 | 0.09 | 0 | 0 | 0.018 |
| 16 | 0 | 0 | ∞ | ∞ | 13.7 | 0 | 50 | 0.1 | 0 | 0 | 0.15 | 0.09 | 0 | 0 | 0.338 |
| 17 | 0 | 0 | ∞ | ∞ | 0.652 | 0 | 50 | 0.5 | 0 | 0 | 0.15 | 0.09 | 0 | 0 | 0.074 |
| 18 | 0 | 0 | ∞ | ∞ | 13.7 | 0 | 50 | 0.5 | 0 | 0 | 0.15 | 0.09 | 0 | 0 | 1.687 |
| 19 | 0 | 0 | ∞ | ∞ | 0.652 | 0 | 30 | 0 | 0 | 0 | 0.15 | 0.09 | 0 | 0 | 0.187 |
| 20 | 0 | 0 | ∞ | ∞ | 0.652 | 0 | 30 | 0 | 0 | 0 | 0.15 | 0.09 | 0 | 0 | 0.011 |
| 21 | 0 | 0 | ∞ | ∞ | 13.7 | 0 | 30 | 0 | 0 | 0 | 0.15 | 0.09 | 0 | 0 | 0.011 |
| 22 | 0 | 0 | ∞ | ∞ | 0.652 | 0 | 30 | 0 | 0 | 0 | 0.165 | 0.097 | 0.017 | 0.01 | 0.167 |
| 23 | 0 | 0 | ∞ | ∞ | 0.652 | 0 | 50 | 0 | 0 | 0 | 0.165 | 0.097 | 0.017 | 0.01 | 0.954 |
| 24 | 0 | 0 | ∞ | ∞ | 13.7 | 0 | 30 | 0 | 0 | 0 | 0.165 | 0.097 | 0.017 | 0.01 | 0.07 |
| 25 | 0 | 0 | ∞ | ∞ | 13.7 | 0 | 50 | 0 | 0 | 0 | 0.165 | 0.097 | 0.017 | 0.01 | 0.507 |
| 26 | 0 | 0 | ∞ | ∞ | 0.652 | 0 | 30 | 0 | 0 | 0 | 0.165 | 0.079 | 0.011 | 0.008 | 0.074 |
| 27 | 0 | 0 | ∞ | ∞ | 0.652 | 0 | 50 | 0 | 0 | 0 | 0.165 | 0.079 | 0.011 | 0.008 | 0.1 |
| 28 | 0 | 0 | ∞ | ∞ | 13.7 | 0 | 30 | 0 | 0 | 0 | 0.165 | 0.079 | 0.011 | 0.008 | 0.06 |
| 29 | 0 | 0 | ∞ | ∞ | 13.7 | 0 | 50 | 0 | 0 | 0 | 0.165 | 0.079 | 0.011 | 0.008 | 0.031 |
| 30 | 0.1 | 0.1 | 70 | 1 | 0.652 | 1 | 50 | 0 | 0.5 | 0 | 0.165 | 0.097 | 0.002 | 0.001 | 0.151 |
| 31 | 0.1 | 0.1 | 70 | 1 | 0.652 | 1 | 50 | 0 | 0.5 | 1 | 0.165 | 0.097 | 0.002 | 0.001 | 0.151 |
| 32 | 0.1 | 0.1 | 70 | 1 | 0.652 | 3 | 50 | 0 | 0.5 | 0 | 0.165 | 0.097 | 0.002 | 0.001 | 0.154 |
| 33 | 0.1 | 0.1 | 70 | 1 | 0.652 | 3 | 50 | 0 | 1 | 0 | 0.165 | 0.097 | 0.002 | 0.001 | 0.151 |
| 34 | 0.1 | 0.1 | 70 | 1 | 13.7 | 3 | 50 | 0 | 1 | 0 | 0.165 | 0.097 | 0.002 | 0.001 | 0.125 |
| 35 | 0.1 | 0.1 | 70 | 1 | 0.652 | 1 | 50 | 0.1 | 0.5 | 0.1 | 0.165 | 0.097 | 0.002 | 0.001 | 0.152 |
| 36 | 0.1 | 0.1 | 70 | 1 | 0.652 | 1 | 50 | 0.1 | 0.5 | 0.1 | 0.165 | 0.097 | 0.017 | 0.001 | 1.014 |
| 37 | 0.1 | 0.1 | 70 | 1 | 0.652 | 1 | 50 | 0.1 | 0.5 | 0.1 | 0.165 | 0.097 | 0.017 | 0.01 | 0.939 |
| 39 | 0.1 | 0.1 | 70 | 1 | 0.652 | 1 | 50 | 0.1 | 0.5 | 0.1 | 0.109 | 0.079 | 0.011 | 0.008 | 0.138 |
| 39 | 0.1 | 0.1 | 70 | 1 | 0.652 | 1 | 50 | 0.1 | 0.5 | 0.1 | 0.109 | 0.079 | 0.001 | 0.001 | 0.1 |

Table 2 Results of the Simplified Error Model

The experiments listed in table 2 and discussed following were programmed for the 3-variable depth bias model. Experiments 1 to 21 were also programmed for the 2-variable depth bias model with almost identical results and therefore are not included because the following discussion applies. Experiments 22 to 39 investigate water turbidity effects and were therefore only programmed for the 3-variable model.

Experiments 1 to 4 examine the effect of aircraft height measurement error on depth accuracy. Aircraft height standard deviation (std) errors of 1m were examined for small and large scan angles at depths of 30m and 50m with negligible depth errors predicted.

Experiments 5 to 7 examine the effect of a one-sample std error in the detection of IR surface position. The predicted resulting std errors of the order of 0.25 m is significant and indicates

the importance of minimizing the error in the estimation of the position of the IR surface. This result is obvious; as the IR laser beam acts as a local surface reference, refer section 3.2.

Experiments 8 to 12 examine the effect of waveform detection. Here the effect on depth error is seen to be trivial as normal bottom pulse slopes are generally much greater than one. However the depth error increases as the slope of the pulses approach one, which occurs in deep or turbid water where the pulse gradually disappears into the background noise. However even with a small pulse slope, assuming the correct bottom pulse is selected, the depth error contribution is less than 0.01m.

Experiments 13 to 18 examine the effect of errors in the measurement of scan angles ($\Phi_1$). These results predict depth errors increasing with scan angles, becoming significant at large scan angles. Experiment 18 predicts a large depth error of 0.9m, for a scan angle error ($\sigma_{\delta\varphi}$) of 0.5° at a scan angle ($\varphi_1$) of 13.7°. This result is to be expected because of the H sec$\Phi$ correction factor in the delay ($\Delta_2$) used in the positioning of the laser waveforms, refer to section 3.2. This result indicates the importance of accurate measurements of scan angles.

Experiment 19 shows the effect of errors outside the control of the ALB system. They consist of tide measurement errors (which add to the system errors) and benchmark comparison errors (which give a false measurement of the accuracy of the ALB system). Assuming tide errors ($\sigma_{\delta dtide}$) of 0.1m, benchmark depth errors ($\sigma_{\delta dbm}$) of 0.15m and benchmark comparison errors ($\sigma_{Ebmc}$) of 0.05m the model predicts a depth std error of 0.19m.

Experiments 20 and 21 show the effect of an error $\delta t_1$ in the linear interpolation process in the detection of the bottom pulse, refer section 4.5 figure 15. Depth errors resulting from this effect are shown to be insignificant.

Experiments 22 to 25 examine the effect of errors in the measurement of attenuation coefficients ($k_S$ and $k_L$) in turbid seawater. Here it is predicted that measurement errors in $k_S$ or $k_L$ may cause significant errors in depth particularly for small scan angles ($\varphi_1$=0.652°) and deep depths ($d_1$>30m), refer result 23. For these experiments it was assumed that the measurement error of k was 10% of the value of k. This assumption in reality is excessive; as can be seen from measure real data values in section 4.12. However it does illustrate the importance in the measurement accuracy of attenuation coefficients.

Experiments 26 to 29 examine the effect of errors in the measurement of attenuation coefficients in clear seawater. Again error values of 10% value of k were assumed. These results predict a much smaller depth error, which indicates the 3-variable model is less sensitive to error for clear seawater coefficients. This result is providential in that it is easier to measure attenuation coefficients in turbid seawater than in clear seawater, because of the larger back scatter waveforms.

Experiments 30 to 34 examine the effect of rough seas and turbid seawater conditions. Small errors are assumed in the measurement of $k_S$ and $k_L$, and pulse slopes of $m_s$=0.5m and $m_b$=1 are assumed for surface and bottom pulses respectively. Model results predict depth errors that are insensitive to different degrees of sea roughness. For example for a surface bias of b=0.5m or 1m, or a measured tilt of $\Delta\Phi$=0° or 1° with $\Phi$=0.652° predicted depth errors are approximately 0.13m.

However for experiments 35 to 39 where an additional scan angle error of 0.1° was used, little change in the predicted depth error was evident except for experiments 36 and 37 where a larger error in the measurement of $k_s$ was used. These results again illustrate the sensitivity of the 3-variable depth bias model to $k_S$ and $k_L$ values.

In summary we can see from figure 17 that large depth errors are predicted for experiments 18, 23, 25, 36 and 37. Of these, experiment 18 predicts a large depth error for a large error 0.5° in the measurement of a large scan angle $\Phi_1$=13.696°. The other experiments indicate the sensitivity of depth accuracy to the measurement accuracy of $k_S$ and $k_L$, particularly $k_S$ in turbid seawater conditions.

## 4.18 Discussion

The results produced have identified three areas where significant depth errors were predicted.

Firstly, the results of experiments 5 to 7 show significant depth errors where there was an error assumed in the measurement of the IR sea surface position $k_{IR}$ of one sample time. In the LADS system, interpolation between sample times is used to detect the position of the IR surface pulse more accurately than to one sample time of $\Delta t$= 2 ns. Alternatively a higher sampling rate could be employed which would require the use of faster analogue to digital conversion and support hardware.

Secondly, it was seen that where an error in the measurement of the scan angle ($\Phi_1$) was assumed for large scan angles, see experiments 14,16 and 18, significant depth errors can occur. Here, the measurement accuracy of the angle of the scanning green laser beam is related to the system hardware. The use of digital shaft encoders or some other accurate angle measurement hardware is required to minimize depth errors from this cause.

However the most significant depth errors predicted by the error model occurred when errors in the measurement of attenuation coefficients are assumed. Errors of 0.017 and 0.01 in the measurement of $k_S$ and $k_L$ respectively, result in large depth errors of 0.493 m to 0.926 m at a depth of 50 m, refer to experiments 25 and 23. Typical values for $k_S$ and $k_L$ are 0.165 and 0.097, so that a percentage measurement error of 10% was assumed. These experiments show the importance of accuracy in the measurement of turbidity parameters, to minimize depth errors when using the 3-variable depth bias model. However, it should be realised that to estimate depth, without any account of water turbidity, will also cause large errors in the measurement of depth, refer to the benchmark analysis results in section 5.1.

Tide errors can also be significant as they are added directly to errors in depth. Tide pole measurements are normally only possible in convenient location and need careful reading in rough seas. In open sea conditions, it is convenient to use pressure tide gauges. However their readings need to be carefully adjusted for local atmospheric pressure and temperature to obtain accurate tide measurements. Tide prediction stations may also be used, but a convenient monitor station must be used to correct these tide predictions. Errors from the careful measurement of tide can be of the order of 0.1 to 0.15 metres.

It should be realised that the simplified error model is based on the depth correction processes detailed in section 3. Therefore it is to be expected that there will be other errors not predicted by the simplified error model, and the analysis of data performed in the next section is used in an attempt to identify them. Some possible causes of errors not predicted by the error model are listed following.

- When a depth bias model is used that does not allow for water turbidity, large errors in depth, of the order of 1m or larger, can occur.
- When no surface pulse is detected and a late entry occurs, then no late entry correction is applied by the LADS algorithms, and depth errors will result, which may be up to one quarter of the local wave height.
- When the scanning laser beam does not refract through a horizontal sea surface, skewing of the beam will occur causing either deeper or shallower depths to be predicted depending whether a larger or smaller refraction angle results.
- Other effects, such as turbidity layering, may occur and contribute to errors in the depth bias correction algorithm.
- Other effects may produce depth errors, which have not yet been identified, and the analysis of trial data may help to discover them.

In summary, the error model allows the prediction of depth errors of an ALB system, given estimates of input and system measurement errors. It allows the identification of factors, which most effect, the accuracy of the ALB system.

# 5. Analysis of Airborne Laser Bathymetry Data

A method for measuring the depth accuracy of an ALB system is to compare its estimated depths against benchmark depths accurately measured by hydrographic survey ships. The remaining or residual depth errors can then be examined for correlation against measurable system variables, in an attempt to find a method for reducing these errors.

It is important to select a suitable benchmark area, where accurate benchmark depths can be determined. The benchmark area should have a flat bottom, to minimise the effect of position error on the accuracy in the calculation of depth comparisons. A continuous benchmark area, gradually increasing in depth, is also desirable. This feature will enable the effect of seawater depth on any determined depth accuracy, to be investigated. Ideally, the benchmark area should cover all depths between zero and 50m, which is the range of depth measured by a typical ABL system.

The Rod's Run benchmark is the only benchmark surveyed in Australia at present, meeting these requirements. It is located in Saint Vincent's Gulf South Australia and slopes down from 2 m at the shallow end to approximately 32 m at the deep end, and is approximated 35 km long by 500 m wide.

The last available suitable benchmark results data from this area, are from the South Australian August 1994 trial, which consisted of four sorties, detailed below. Here the runs shown underlined were flown from shallow to deep water; the remaining listed runs were flown from deep to shallow water.

| Date | Sortie | Runs | Weather Condition |
|---|---|---|---|
| 2/8/94 (Tues) | s332 | r531, r532, r540 | smooth seas |
| 3/8/94 (Wed) | s333 | r533, r534 | glassy seas |
| 5/8/94 (Fri) | s334 | r584 | rough seas |
| 6/8/94 (Sat) | s335 | r590, r611, r612 | very rough seas |

The first two sorties were flown under calm sea conditions while the remaining two sorties were flown under rough sea conditions. The data collected were therefore, ideal for examining the effect of sea surface conditions on residual depth errors. Furthermore, because the data were collected along a continuous benchmark area, with varying depth and seawater turbidity, valuable information can be gained from the returned laser waveforms against the measured residual depth errors. For example it was apparent in the data from sorties s332 and s333 that large positive residual depth errors occur when small return bottom pulses were observed.

## 5.1 Benchmark Analysis

Results from the August 94 trial are analysed for all of the runs listed above. For convenience the continuous benchmark is divided into twenty smaller adjoining benchmarks, which are named: rr1, rr2, rr3, to rr20. The residual depth errors for each separate benchmark area can be analysed and compared separately.

For each separate benchmark area, each measured LADS depth ($d_{lads}$), is compared with a corresponding surveyed benchmark depth ($d_{bm}$), and a residual depth error ($d_{err}$) calculated, as follows.

$$d_{err} = d_{lads} - d_{bm} \tag{5.1}$$

where $d_{lads}$ is the depth of seawater measured by the LADS system using the 2-variable depth bias model, refer to sections 3.8 and 3.9.

Histograms of all $d_{err}$ data, for each benchmark were compiled, and provide a measure of the depth accuracy of the LADS system for each benchmark area. From plots of these histograms it was observed that the distribution of residual depth errors is essentially gaussian.

A test for normality was performed on the histogram of run r534 data by comparing it with a fitted gaussian function and performing a chi-square test at $\alpha = 0.1$ level of significance. The Levenberg-Marquardt (LM) algorithm [32] was used to fit a gaussian function

$$y = \frac{A}{\omega\sqrt{\frac{\pi}{2}}} e^{\frac{-2(x-x_0)^2}{\omega^2}}$$

to the residual depth error histogram of 300 bins from –1.5 to 1.5m in 0.01m increments. The resulting gaussian function is shown in figure 18 where it is plotted over the residual depth error histogram.

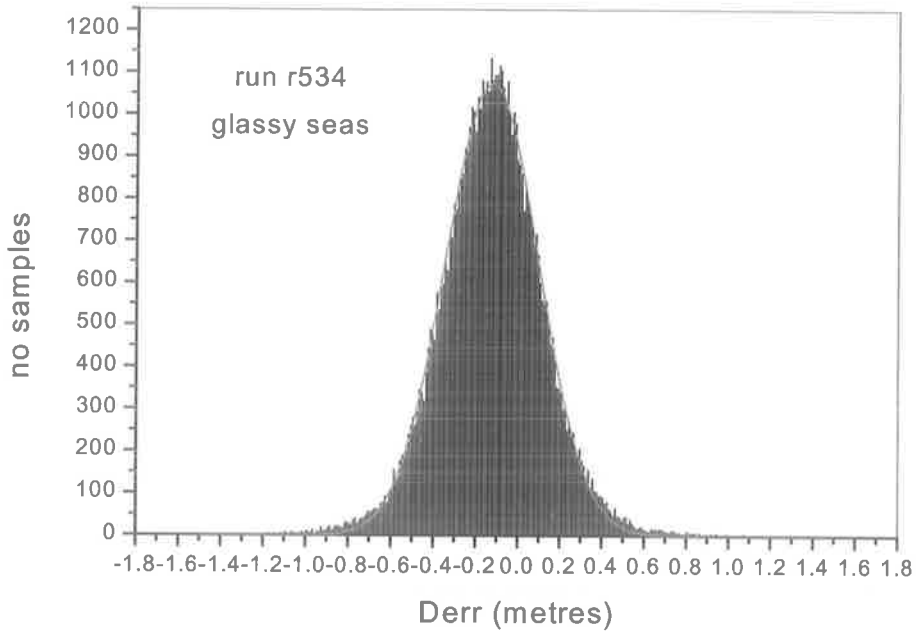


Figure 18 Histogram of residual depth errors $d_{err}$ for run r534

A chi-squared result of: $\chi^2 = 281.5$ was obtained, and with n = 300-3 = 297 degrees of freedom and for the acceptance of normality for a $\alpha = 0.1$ level of significance it is required that: $\chi^2 < \chi^2_{297,0.1} = 299$.

We therefore have a 90% confidence of normality for the residual depth error histogram of run r534. Similar results were obtained for the other run data.

The combined $d_{err}$ statistics of all benchmark areas for each run are listed in table 3 below. Here the sample mean, standard deviation and number of samples for each residual depth error distribution are provided. (The $d_{err}$ results include data from all scan angles. )

| Run number | Mean_$d_{err}$ (metres) | Std_$d_{err}$ (metres) | No Samples |
|---|---|---|---|
| r532 (smooth) | -0.033 | 0.261 | 57813 |
| r532 | -0.018 | 0.260 | 60787 |
| r540 | -0.046 | 0.302 | 60335 |
| r533 (glassy) | -0.118 | 0.247 | 58940 |
| r534 | -0.117 | 0.244 | 60796 |
| r584 (rough) | -0.021 | 0.199 | 69420 |
| r590 | -0.047 | 0.230 | 61907 |
| r611 (very rough) | -0.058 | 0.223 | 63121 |
| r612 | -0.052 | 0.227 | 69062 |

Table 3 Mean and standard deviations of residual depth errors ($d_{err}$)

This data is presented graphically in Figure 19 for examination, where, for a given run, the sample mean and the standard deviation for each residual depth error distribution for each individual benchmark area, are plotted against the average depth of each benchmark area. There are nine plots, one for each run. Runs r531, r532, r540 for day one (smooth seas), runs r533, r534 for day two (glassy seas), run r584 for day three (rough seas) and runs r590, r611, r612 for day four (very rough seas). (Note that the horizontal marks on the plots are used to represent the standard deviation of each residual depth error distribution, and not error bars of the mean estimates)

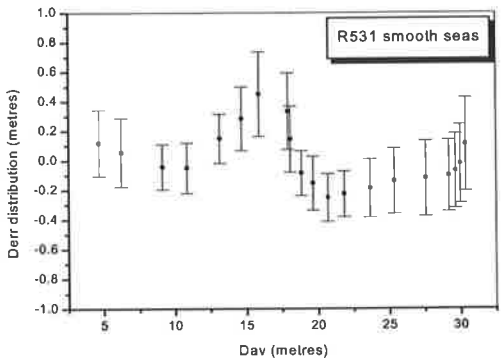


19 (a)

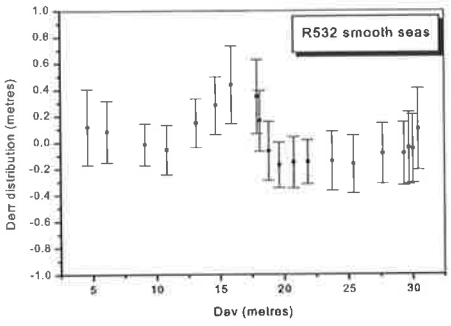


19 (b)

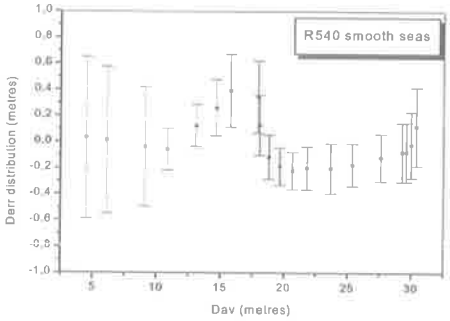


19 (c)

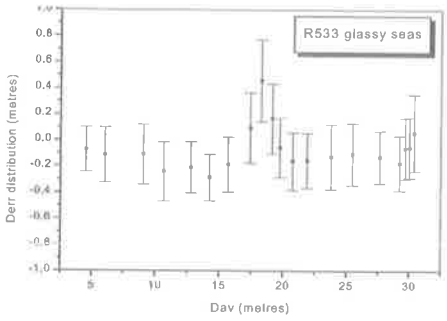


19 (d)

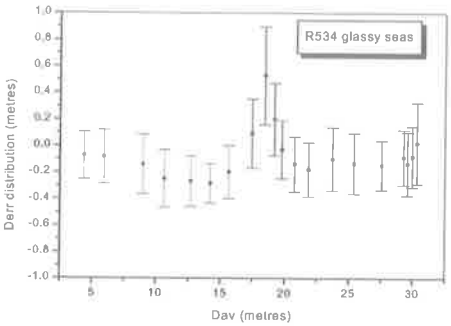


19 (e)

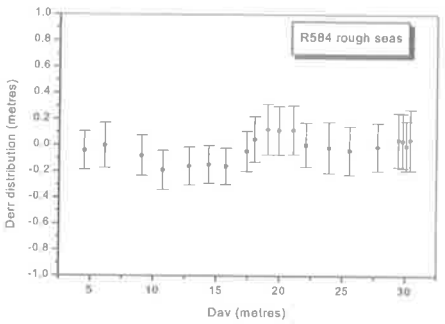


19 (f)

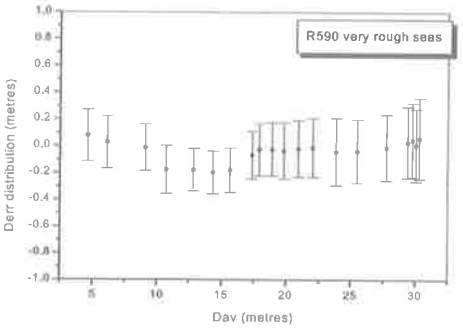


19 (g)

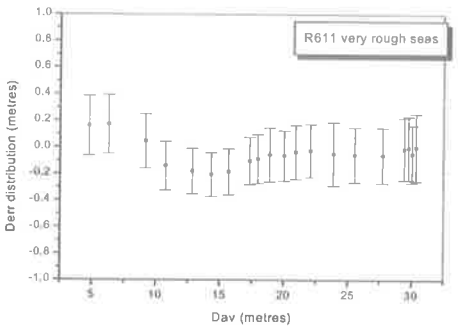


19 (h)

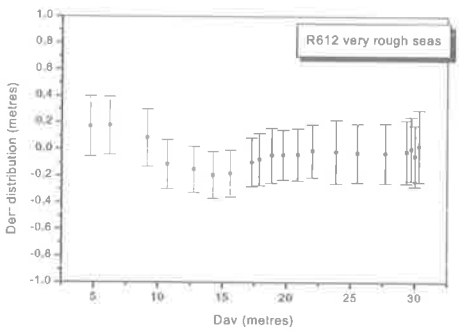


19 (i)

Figure 19 Residual depth error ($d_{err}$) benchmark results

These plots summarise the depth accuracy of the LADS system over all runs of the SA August 1994 trial.

Examination of these results provides several important observations.

Firstly, for any one-day the results are consistent, with one exception. The first three benchmark results of r540 differ from those in r531 and r532. This difference was due to tilt induced depth errors. An experimental platform tilt was enforced on the scanning laser platform in the LADS airborne system during the last section of run r540. This action resulted in tilt errors in the corresponding LADS depth measurements, and is discussed further in paragraph 5.3.

Secondly, day-to-day variations reflect the state of the sea. For example on Tuesday (Figure19(a,b,c) smooth seas) the mean residual depth errors for benchmarks at depths of 15 to 18 metres are positive. A positive $d_{err}$ indicates that the LADS system is measuring depth too deep, refer equation (5.1), and that the LADS bias model is not providing enough depth bias correction. Then on Wednesday (Figure 19(d,e) glassy seas), results show that this effect has moved deeper to depths of 17 to 20 metres. On Friday (Figure 19(f) rough seas) this effect has moderated but is still visible at 18 to 21 metres, and on Saturday (Figure 19(g,h,i) very rough seas) it is not apparent.

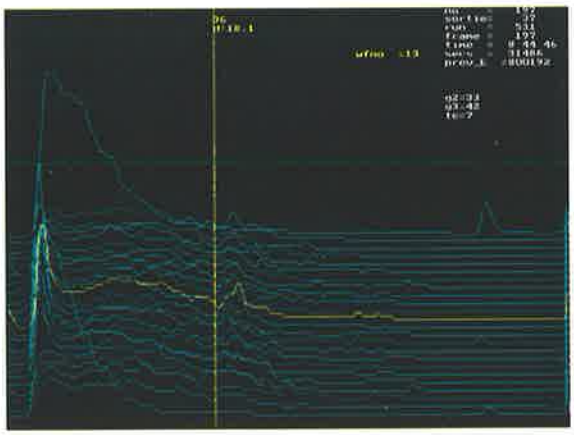

20(a) smooth seas (r531)

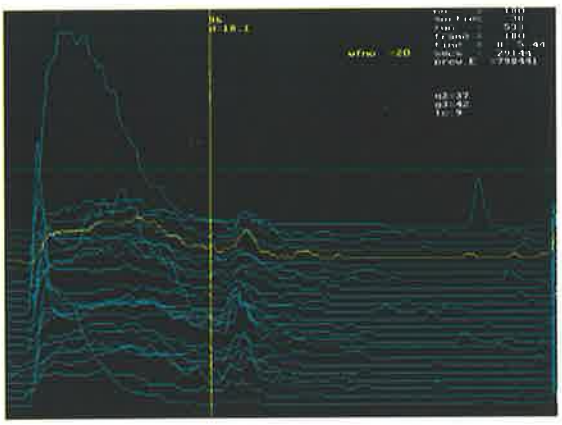

20(b) glassy seas (r533)

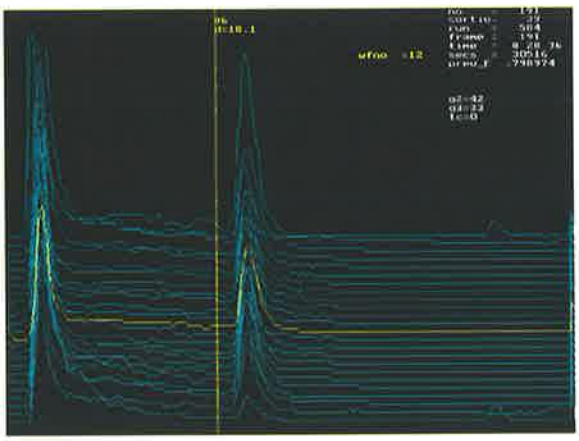

20(c) rough seas (r584)

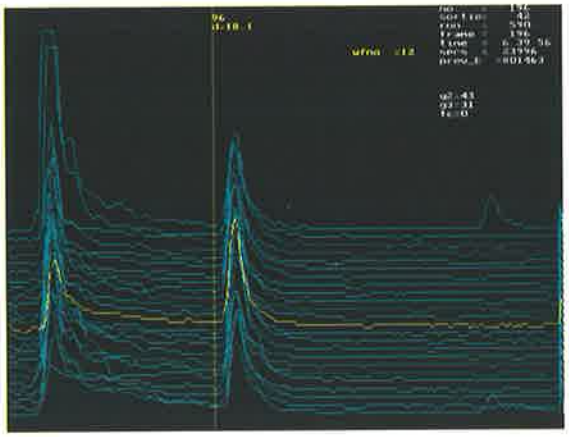

20(d) very rough seas (r590)

Figure 20 Waveform displays of various seawater conditions

The question arises, why are these results different on different days? The results are over the same benchmark area, so any errors in the benchmark depths or in seabed reflectivity are not responsible. Errors due to tide measurement can also be discounted, for if they occurred, they would apply along the whole run and not be confined to one isolated part of the run. Sea surface effects can be ruled out, because the positive residual depth phenomenon occurred on days where there is little or no sea surface wave activity. Therefore seawater quality would appear to be the cause of this effect. The examination of the raw sounding waveforms at a depth of approximately 18m, supports this explanation, as large backscatter and bottom pulse attenuation is clearly evident on the waveforms of Figures 20(a) and 20(b) but not on waveforms of Figures 20(c) and 20(d). The connection between positive $d_{err}$ and turbid seawater is obvious. The extremity waveforms shown in Figures 20(a) and 20(b) show a slow decay indicating turbid seawater, while the extremity waveforms of Figures 20(c) and 20(d) show a fast decay indicating clear seawater. The highlighted waveforms shown in Figures 20(a) and 20(b) both show a small pulse for the bottom return, preceded by a hump in the waveform again indicating turbid seawater, while those in Figures 20(c) and 20(d) show large bottom pulse with little other return backscatter energy, thus indicating clear seawater.

## 5.2 Large Error Analysis

For a more detailed understanding of the causes of residual depth errors, it was decided to investigate the characteristics of individual large errors. The idea was to locate large errors in the $d_{err}$ data, and by examining the corresponding raw waveform data, see whether some error cause could be determined. The method used to locate these depth errors was to display the magnitude and scan pattern position of two-second frames of $d_{err}$ data, refer to Figure 21(a). Errors larger than some preset value could be highlighted and their position in the scan pattern noted. Once the scan position of the error was determined, the corresponding laser waveform could be identified and examined. A typical two-second frame of $d_{err}$ data is shown displayed in Figure 21(a).

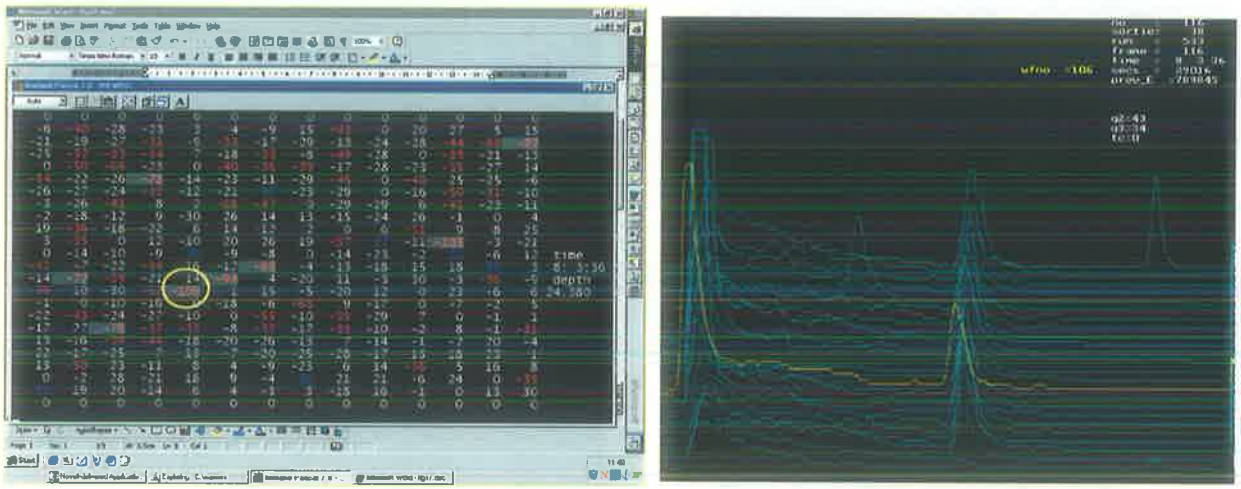

21(a) Scan spot display

21(b) Scan waveform display

Figure 21 Large error analysis diagrams

All the $d_{err}$ errors in figure 21(a) are displayed in cms and all large positive or negative errors are highlighted for attention as previously mentioned.

Note that the position of the $d_{err}$ values in figure 21(a) corresponds to the scan pattern positions (previously illustrated in Figure 4) rotated clockwise by 90°. For example, in Figure 21(a), for scan position 8, $d_{err}$ = -22 cm and for scan position 27, $d_{err}$ = -19 cm and so on.

For example in Figure 21(a) an error of –109 cm occurs (circled) for sounding position 106. This error can then be related to the corresponding laser waveform, highlighted in Figure 21(b), used to calculate the ABL depth. Here the highlighted waveform for sounding 106 shows a waveform displacement to the left, compared with the other waveforms in that scan. This left shift or error in the position of the waveform indicates that the depth is measured shallower than true and a negative $d_{err}$ is recorded.

Also of note in Figure 21(d) is a bottom pulse much shallower than the rest. If this waveform were examined carefully, it would be found that no surface reflection was present on this raw waveform. The explanation for this result is that the IR surface reflection pulse was not detected and recorded on the composite waveform $w_c[k]$, refer to Figure 5. This will result in the green surface reflection being selected as the IR pulse, which will result in a left shift in the stored raw waveform $w_r[s]$. This situation is routinely checked for in the ABL processing, and when detected the resulting depth calculation is treated as invalid.

The large error analysis technique explained here was used extensively to isolate sections of data for analysis in the following sections.

## 5.3 Sea Surface Tilt Analysis

Benchmark results suprisingly indicate a wider variance of depth errors under smooth sea conditions than under rough sea conditions, refer to table 3 and to Figure 19.

A possible cause for this result, could be the occurance of errors in the measurement of sea surface tilt. Depth errors due to tilt measurement errors will occur, if there was an error in the vertical reference of the laser platform, causing the laser platform to be stabilized off horizontal, and if the sea surface filter was not effective in detecting $\Delta\Phi$ and removing this tilt, refer to section 3.5. Any error $\delta\Delta\Phi$ in the measurement of $\Delta\Phi$, will result in an error $[-(H/\eta_w)(\sin\Phi_1/\cos^2\Phi_1)]\,\delta\Delta\Phi$ in the determination of $s_{b2}$, refer equation 4.8. That is the error $\delta s_{b2}$ in the position of the bottom pulse will be positive or negative dependent on the sign of $\Phi_1$. This will result in shallow errors (ie $d_{lads} < d_{bm}$) occurring on one side of the display pattern and deep errors ($d_{lads} > d_{bm}$ ) on the other side of the display pattern.

In the last section of run r540 a deliberate platform tilt was imposed of unknown angle and the resultant displacement of the waveforms are shown in figure 22. Here a displacement of approximately 5m of the waveforms from nadir to extremity is seen. The resultant error in the determination of the bottom was determined to be –1.44m, by reference to the corresponding scan spot display (not shown), for the sounding corresponding to waveform no 23. Thus, although the surface filter was able to reduce the depth error from -5m to -1.44m some error remained.

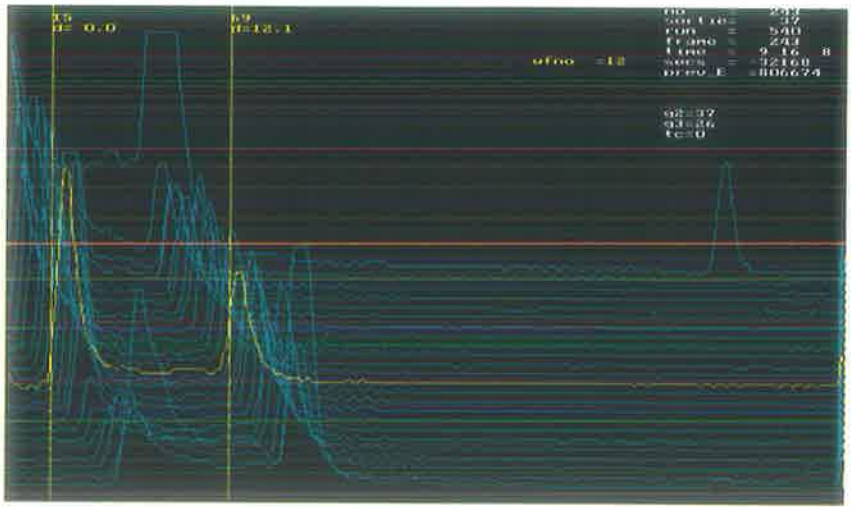

Figure 22 Platform tilt waveform diagram

Also, increasing positive depth errors can be seen on the port side of the spot display, with decreasing negative errors on the starboard side. Again these errors are considerably smaller than indicated by the waveforms in Figure 22, again signifying that the surface filter was successful in reducing tilt error but not completely, refer to Figure 19(c).

When the ABL system is in operation use, platform tilt errors are much smaller than those shown here. The large inertia of the laser platform helps to stabilize it against any sudden roll motions of the aircraft, and the platform roll stabilization control system basically only has to overcome the friction of the platform roll bearings.

In reality, the tilt induced depth error problem is most likely to occur in smooth seas, where the number of valid sea surface reflections (from the green laser beam) available to the sea surface filter is limited to one or two at nadir. Invalid sea surface reflections occur in flat sea conditions when the green beam is scanning away from vertical and the reflected sea surface pulse is reflected away from the field of view of the receiver. In this case the accuracy of the sea surface filter in removing tilt under smooth seas may not be ideal. This phenomenon is examined in Appendix B, where it is shown that the surface filter will be less effective in removing tilt induced depth errors in smooth seas than in rough seas.

To establish whether tilt induced errors were significant, all benchmark comparison data for flat sea conditions were examined. Scan spot displays of all depth errors along runs r531, r532, r540, r533 and r534 for calm and glassy seas were performed. While the theoretical analysis in Appendix B suggested that tilt induced depth errors are likely to occur in smooth seas, the data analysis results showed no evidence of this, except at the end of run r540, where a deliberately large platform tilt was caused. The spot scan display of figure 21(a) was typical of results obtained, with positive and negative depth errors evenly spread across all scan angles.

## 5.4 Late Detection of IR Surface Reference

Applying the large error analysis method to all the trial data, it was also found that a number of large negative depth errors were associated with early green laser waveforms (refer equation 3.2). An example is shown highlighted in Figure 23 below, where waveform 62 (shown highlighted), is seen to be displaced earlier in time, than the other 23 scan waveforms.

This example is typical example of a delayed IR surface detection. This result can be explained by the late detection ($t_{IR}$) of the sea surface by the IR pulse, refer to sections 3.3.1

and 3.3.2. That is, as the detected time of the sea surface by the IR pulse ($t_{IR}$) becomes later, the position of the surface pulse ($s_{fl}$) and the position of the bottom pulse ($s_{bl}$) becomes earlier relative to the IR surface position. Late detection errors of the sea surface by the IR pulse will therefore result in shallow depth errors in the LADS system. That is, LADS depths will be determined shallower than the true depths.

In order that these errors can be corrected, some reliable method of prediction is required. From the previous explanation, any late detection of the sea surface by the IR pulse results, not only in an early calculation of the sea bottom, but also on an early calculation of the sea surface detected by the green laser pulse. Therefore, it would seem, (in flat seas) the early detection of the sea surface, relative to its neighbours, by the green laser pulse may be a satisfactory method by which these errors can be predicted and corrected.

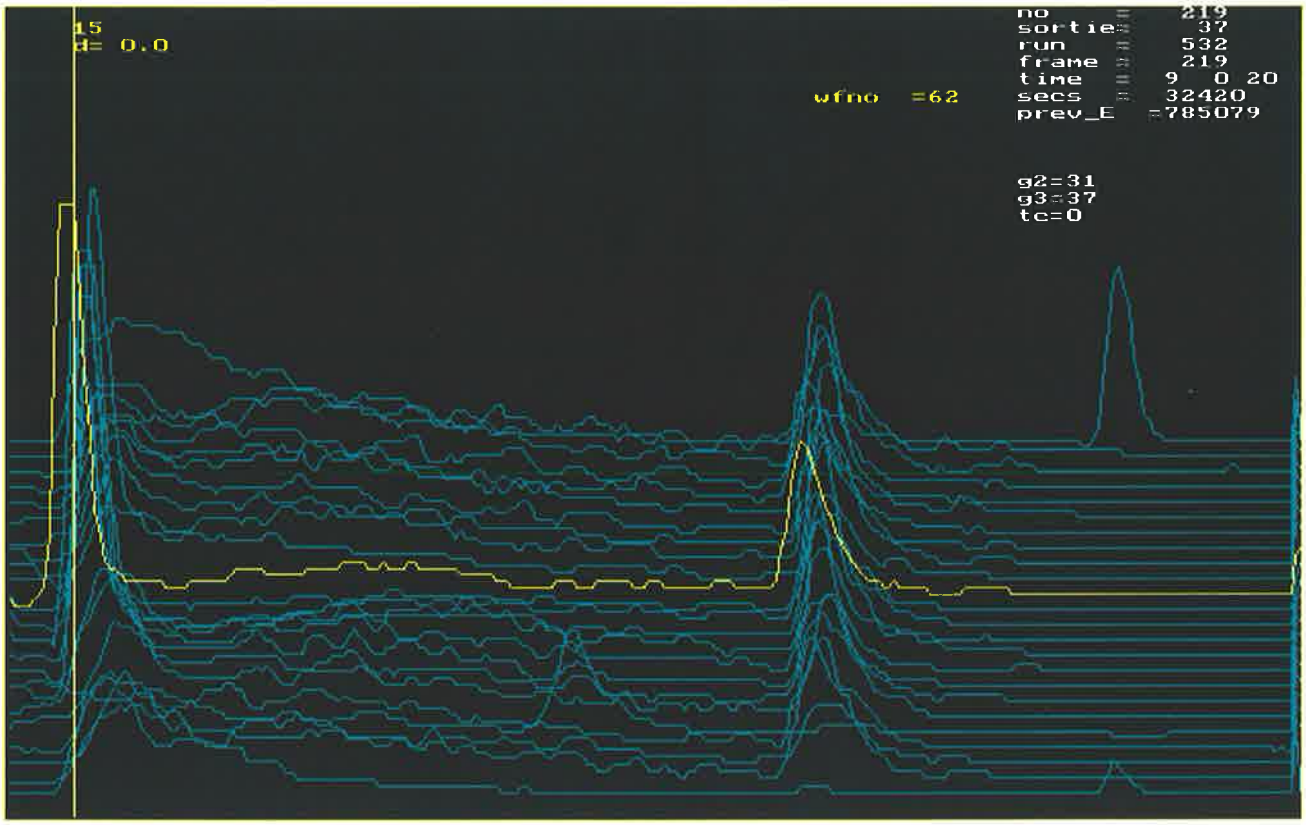


Figure 23 Late IR surface detection waveform diagram

The results of sorties s332 and s333 were analysed for correlation between early surface detection, by the green laser pulse, and shallow depth errors. Results from these sorties were selected, to remove the error caused by wave action in the detection of the mean sea surface. Histograms of surface detection positions ($s_{bl}$) and depth errors ($d_{err}$) were compiled, and checked for anomalies.

For example, a large negative residual depth error is shown circled in Figure 24(a), run r532, frame time 8:59:18, laser spot 230, where a residual depth error of –1.08 m was observed. Errors from neighbouring pulses were +0.19m, -0.20m, +0.47m and –0.26m for laser spots 229, 251, 231 and 203 respectively. Again examination of the raw laser waveforms, shows laser waveform 230 to be displaced earlier in time.

In Appendix C, the dependency of depth error on the detection position of the green surface pulse was analysed. Here for each benchmark area, the normalised green surface positions were determined and correlated against the corresponding residual depth errors normalised as discussed in Appendix C. The results obtained were inconclusive however and although it was shown that there is some correlation between green beam surface position and residual depth error, there was insufficient correlation to enable a significant improvement in depth accuracy. In particular, although several shallow depth errors were related to the detection of early green surface pulses, the detection of early pulses did not generally signify a shallow depth error measurement.

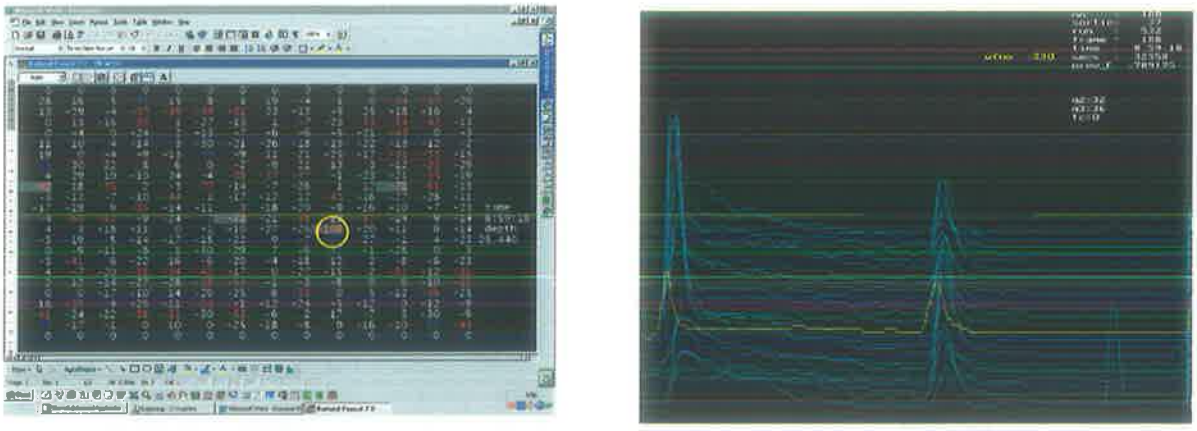

24(a) 24(b)

Figure 24 Large residual error diagram

## 5.5 Turbidity Characteristics Analysis

Previous benchmark analysis (using the 2-variable depth bias model), refer to para 5.1, has implied a relationship between large positive depth errors and turbid seawater. Referring to figures 19 and 20, it can be seen that the increase in the residual depth error at a depth of 18m, coincides with the attenuation of the return laser waveform. Here the attenuation of the laser waveforms in figures 20(a) and 20(b) is clearly seen and is an indication of turbid seawater.

The 3-variable depth bias model, referred to in section 3.8, was developed to account for seawater turbidity by the use of a forward scatter coefficient ($b_f$). However trial results have shown that the measurement of $b_f$ does not always correlate closely with residual depth errors and when included in the 3-variable depth bias model, does not always provide the required improvement in depth accuracy.

In this section the dependence of residual depth error against seawater turbidity variables are examined. Data from runs r540, r533, r584 and r590, were selected for analysis, these runs providing representative data for all trial weather conditions. Frame averaged values for $d_{crr}$, $k_S$, $k_L$ and $k_S$-$k_L$ were computed scaled and plotted against time of run, refer Figure 25, where the direction of each of run is from deep seawater (32 m) to shallow seawater (3 m). The terms were scaled for plotting purposes as shown:

$d_{err} = d_{err}$
$k_{S5} = 5k_S$
$k_{L5} = 5k_L$
$k_{SkL5} = 5(k_S - k_L)$

Referring to figure 25, it can be seen that there appears to be some degree of correlation between depth error and the turbidity variables. For smooth seas, figure 25(a), $d_{err}$ initially goes negative before increasing to 0.5m positive momentarily before dropping negative again. As mentioned previously, a positive $d_{err}$, indicates the ALB system is measuring deeper than it should. This result shows that the 2-variable depth bias model is overcompensating in the deeper section of the run and under compensating in the shallow part of the run where the seawater quality is turbid.

It has been observed previously [22] that a turbid gutter exists in the gulf under some conditions. It is thought to occur in calm conditions, where water mixing is low, and when the tide is running out disturbing the seabed.

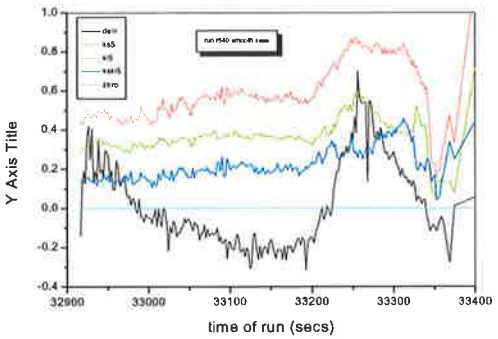


25(a)

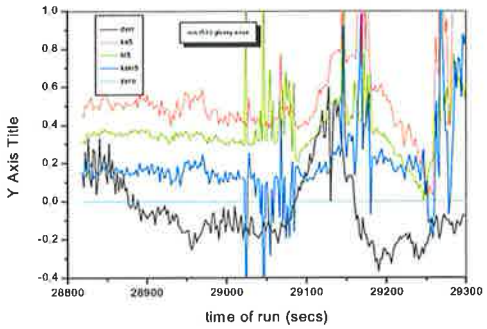


25(b)

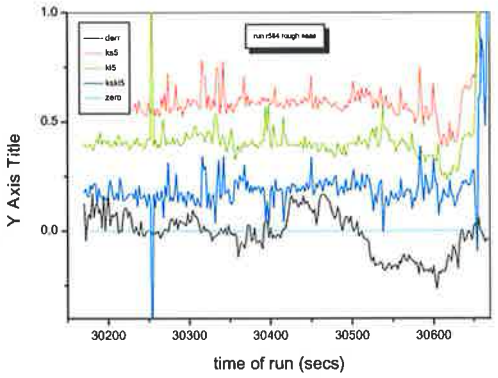


25(c)

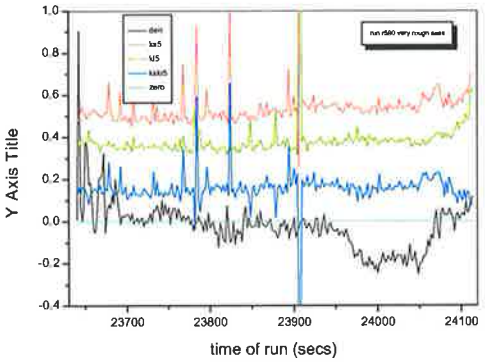


25(d)

Figure 25 Turbidity analysis diagrams

It can also be seen that the attenuation coefficients $k_S$ and $k_L$, remain basically constant for the first half of the run and then increase and decrease in sympathy with $d_{err}$, towards the end of the run. The peak values of $k_S$ and $k_L$ coincide with the peak value of $d_{err}$ about two thirds of the way along the run. However when it comes to the value of the $(k_S - k_L)$ term, which is considered a representative measure of forward scatter of laser light in seawater, it is seen that this term does not always correlate well with $d_{err}$.

It has been found, both in this and the analysis of other data [1, 22], that the measurement of $k_S$ and $k_L$ is less reliable in shallow seawater, where surface seawater effects sometimes distort the raw laser waveforms, and in particular $k_S$ is generally more difficult to measure than $k_L$ . The term $(k_S - k_L)$ is therefore particularly susceptible to error, because of the closeness in the values of $k_S$ and $k_L$ and because it depends on the accuracy of both $k_S$ and $k_L$.

These observations also apply to glassy seas, refer to figure 25(b), where some aberrations are seen in the measurement of $k_S$, and in the determination of $(k_S - k_L)$ and where a turbid region of seawater is again observed.

In rough seas, where there is little variation in the turbidity variables over the runs, refer Figures 25(c) and 25(d), the 2-variable depth bias model is better able to cope, albeit, with some overcompensation (negative $d_{err}$ ) at the shallow ends of the runs. It is thought that rough seas have caused mixing of the water, which has resulted in the dispersal of the turbidity gutter across the run.

In summary, it is shown here that the 2-variable depth bias only produces accurate depth results for average seawater turbidity conditions and does not cater for changing seawater turbidity on a day by day basis. Further, it is seen that the measured turbidity term $(k_S - k_L)$ is not a reliable indicator of $d_{err}$, and therefore any 3-variable depth bias model based on this term would be susceptible to error.

## 5.6 Bottom Pulse Characteristics Analysis

In this section, the characteristics of bottom pulses were examined, to see whether a more satisfactory variable could be found that would more closely correlate with $d_{err}$ than the previously examined turbidity variables. Laser energy as it passes through seawater is absorbed and scattered. This results in the laser sounding pulses being both attenuated in height and spread in width. The more turbid the seawater, the greater are these effects.

Therefore the variables chosen for investigation were, pulse signal to noise ratio ($s_{nr1}$, $s_{nr2}$), pulse width ($p_w$) and the turbidity variable $(k_S - k_L)$ for comparison. Referring to Figure26, (where $c_i$ is an exponential fit to $w_i$ from $i_1$ to $i_2$) we have:

$$s_{nr1} = (w_3 - w_0)/(w_2 - w_0)$$
$$s_{nr2} = (w_3 - w_4)/noise_2 \quad \{ \text{ where } noise_2 = \sum i=i_1 \text{ to } i_2 \sqrt{((w_i-c_i)^2/(i_2-i_1))} \}$$
$$p_w = (i_3 - i_2)$$

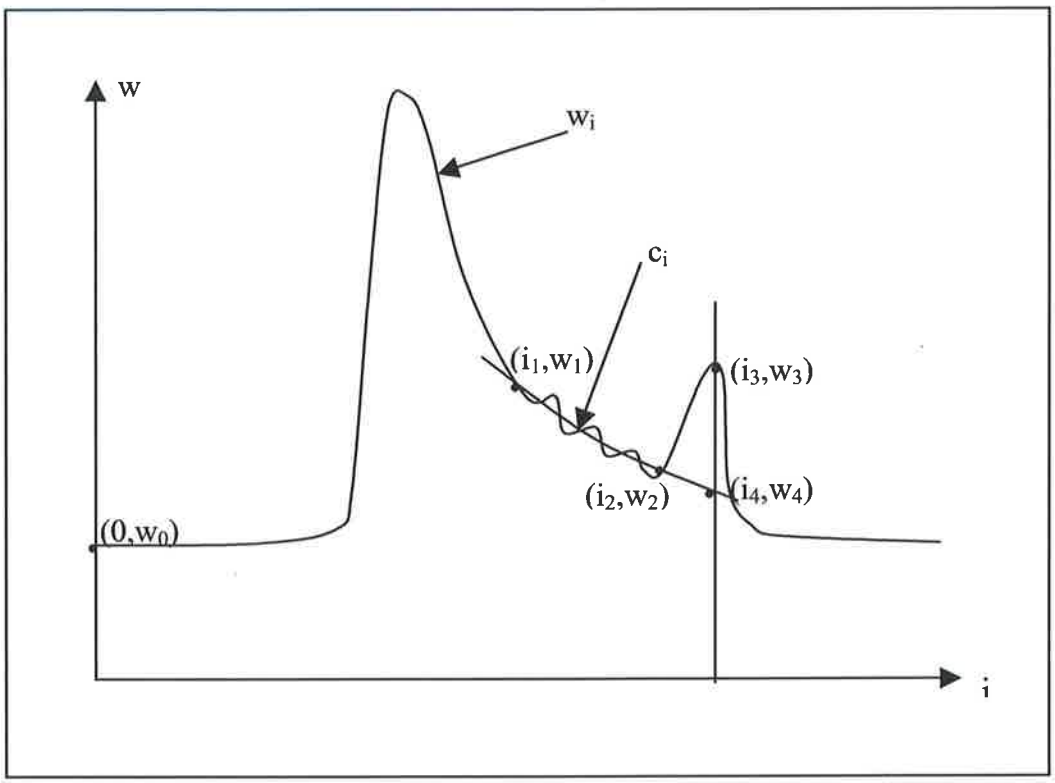


Figure 26 Signal to noise ratio diagram

The following plots, refer to figure 27, show the variation of $d_{err80}$, $s_{nr1}$, $s_{nr2}$, $k_{SkL300}$ and $w_{ide10}$ against time of run in seconds, for runs r540, r533, r584 and r590, where the variables below are scaled for plotting purposes only:

$d_{err80} = 80(d_{err})$
$s_{nr1}$
$s_{nr2}$
$w_{ide10} = 10(p_w)$
$k_{SkL300} = 300(k_S - k_L)$

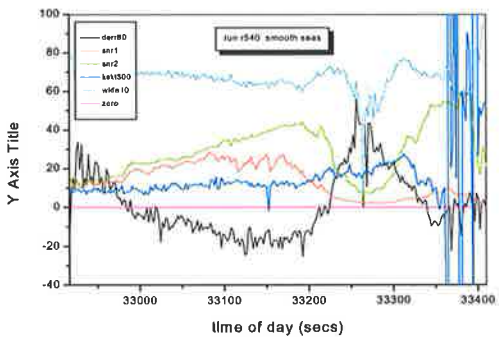


27(a)

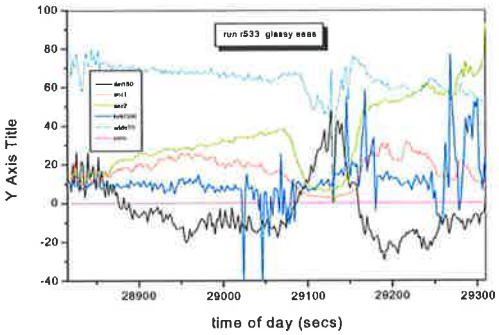


27(b)

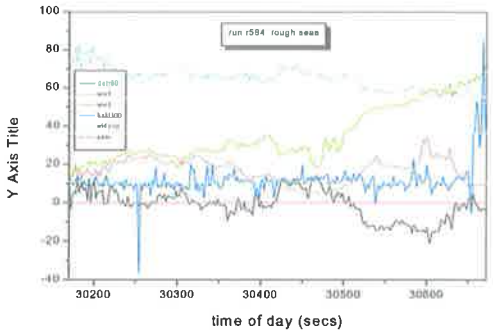


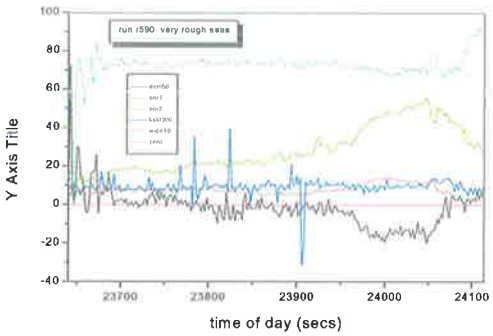


27(c) 27(d)

Figure 27 Bottom pulse characteristics diagram

As mentioned previously in section 5.4, runs r540, r533, r584 and r590 were selected for analysis representing smooth, glassy, rough and very rough seas respectively. The direction of each of these runs in time, is from deep seawater (32m) to shallow seawater (3m).

If we consider the results from run r540 for smooth seas, refer to figure 27(a), we see that the turbidity term $k_{SkL300}$ does not track the residual depth error term $d_{err}$ particularly well. This turbidity measurement gradually increases with a reduction in depth until a point where the turbidity measurement falls off and becomes unreliable in shallow seawater. This does not match the variation in residual depth error with depth, which shows a positive $d_{err}$ hump in the moderately shallow region of the run. However it is noted that the $s_{nr2}$ variable, inversely tracks $d_{err}$ reasonably closely and the $s_{nr1}$ variable also inversely tracks $d_{err}$, to a lesser extent.

It is also interesting to see that the pulse width variable ($w_{ide10}$) initially tracks $d_{err}$, but falls off quickly as $d_{err}$ becomes large positive. The explanation for this result can be explained by examining the relevant waveforms. In the region where there is a large positive $d_{err}$, the bottom pulses merge into the noise, and the measurements of the pulse widths become decreasingly smaller. This is an extremely important observation, as not only does it indicate that the pulse width variable is not a reliable indicator of turbid seawater but it also infers that the 50% pulse depth detection method used in LADS is faulty in highly turbid seawater. The consequences of this observation will be discussed in detail later.

The results of run r533 for glassy seas, show a movement of the positive $d_{err}$ towards deeper seawater. Again it is seen the $k_{SkL300}$ variable does not reliably track $d_{err}$ and becomes erratic in shallow seawater as before. However, the signal to noise variables again are seen to inversely track $d_{err}$.

For runs r584 and r590, refer figures 27(c) and 27(d), it is seen the 2-variable model provides reasonable depth accuracy, as $d_{err}$ remains relatively constant except in the shallow regions where the 2-variable model slightly overcompensates. Here it is interesting to note that the $s_{nr2}$ variable gradually becomes smaller the deeper the seawater. This is expected and holds for all the other results, except where the seawater becomes more turbid and the signal to noise measurement is attenuated further. The $s_{nr1}$ measurement is a different measurement, as it represents the level of the signal to the level of the backscatter and noise. This measurement of signal to noise although being less depth dependant, does not offer as good as measurement of turbidity as the $s_{nr2}$ variable.

Therefore, from the results shown here, the $s_{nr2}$ variable would appear to offer the best chance to model out the effects of turbidity on depth.

## 5.7 SNR Depth Modelling

Experimentation with some elementary polynomial models, using depth, scan angle and signal to noise ratio variables have been made, and have resulted in a number of models which show significant improvement to depth accuracy compared to the existing two-variable B2 model.

The best results were obtained with a three-variable depth bias model D5, which considerably reduced depth errors compared with the existing B2 model. The D5 model was developed using selected data from the SA August 1994 trial, and is defined as:

$$D5 = c_1 d_1/s + c_2 d_1^2/s^2 + c_3 \Phi_2 + c_4 \Phi_2^2 + c_5 \Phi_2^3 + c_6 d_1 \Phi_2/s + c_7 d_1^2 \Phi_2/s^2 + c_8 d_1 \Phi_2^2/s$$

where

$$c_1 = 5.5634 \times 10^{-1}$$
$$c_2 = -4.8523 \times 10^{-2}$$
$$c_3 = 2.5707 \times 10^{-1}$$
$$c_4 = -3.0361 \times 10^{-2}$$
$$c_5 = 1.0105 \times 10^{-3}$$
$$c_6 = -6.3396 \times 10^{-2}$$
$$c_7 = 3.2751 \times 10^{-3}$$
$$c_8 = 2.3574 \times 10^{-3}$$

and

$$s = s_{nr2}$$

The following plots in figure 28 compare the effectiveness of the new D5 model with the existing B2 model, where the predicted values D5 and B2 of the models are compared with the residual depth error derr, and are plotted against time of run in seconds. The remaining predicted errors D5err and B2err are also plotted against time of run, where:

$$D5err = derr - D5$$

and

$$B2err = derr - B2$$

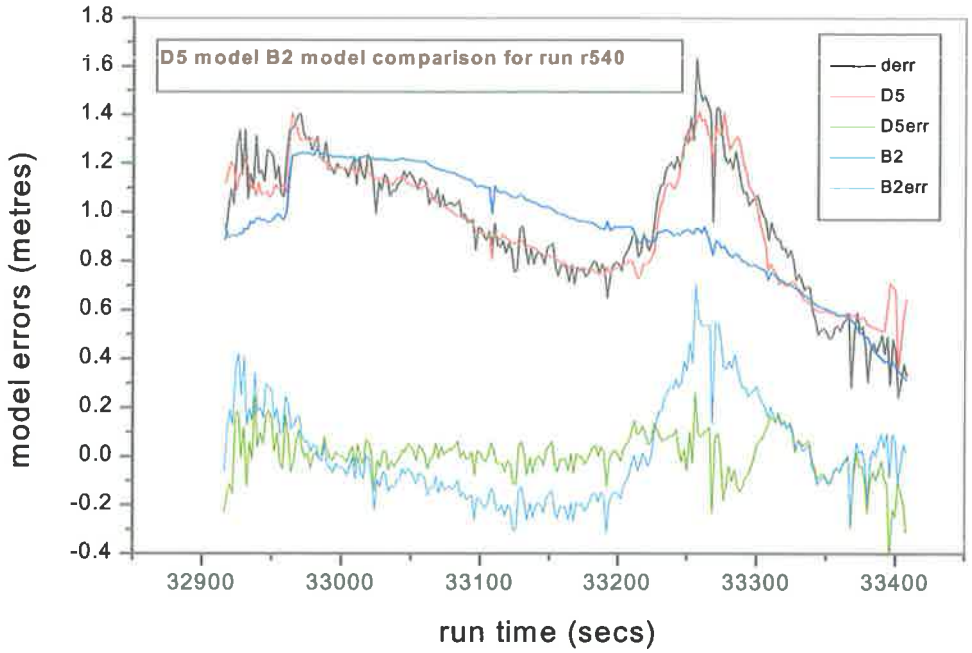


Figure 28a

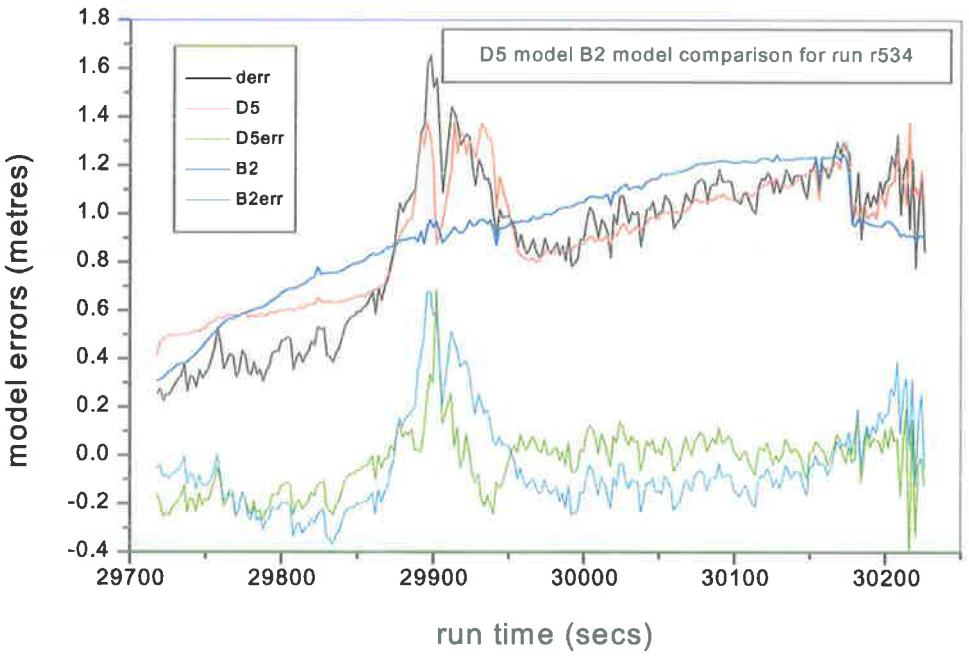


Figure 28b

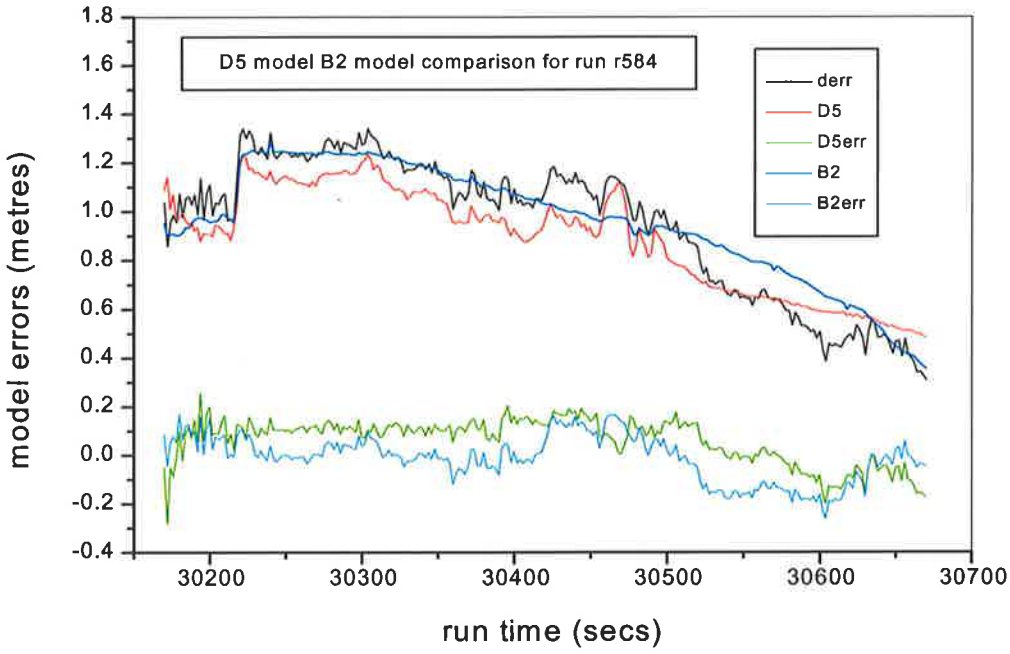


Figure 28c

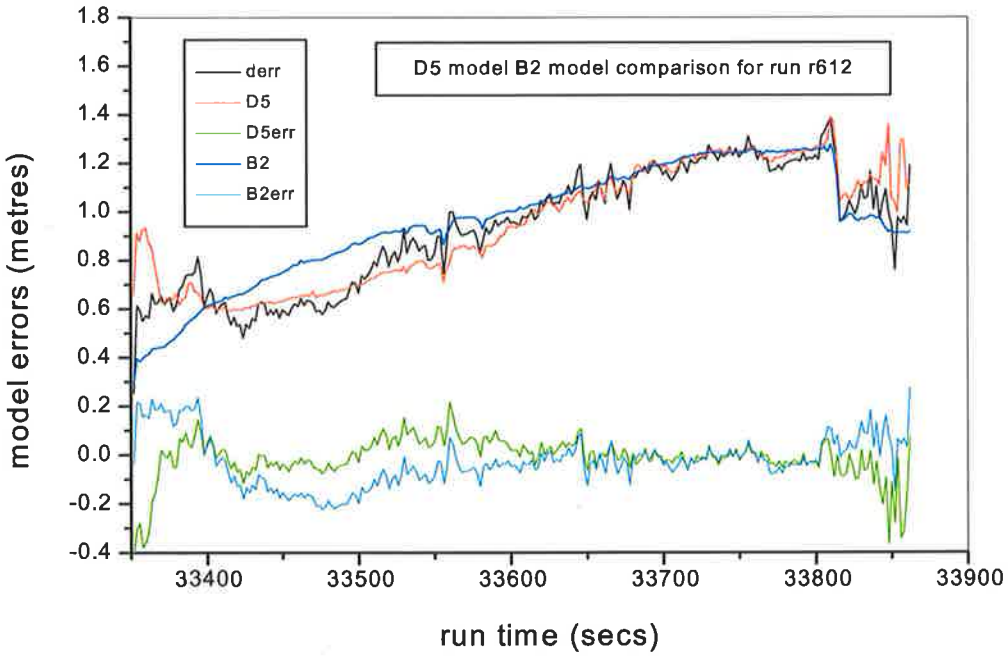


Figure 28d

Figure 28 The three-variable depth bias model comparison

The results in Figure 28, show that the B2 model does not allow for changes in the water quality, where it is seen that the B2 model generally over-compensates for depth bias correction, except for areas of turbid waters where it does not provide enough bias correction. The experimental D5 model however, tracks the residual depth error more closely, providing less bias correction in clear water and more bias correction in turbid water.

However there is still further research to be done to develop and validate a more sophisticated model, as the results shown here are based on a small sample of data. Other problems, such as loss of the bottom pulse signal, due to seabed reflection and absorption and water attenuation effects need to be considered, and related to signal to noise measurement. Nevertheless this small sample of data contains a wealth of variable information. It contains continuous data from shallow water to deep water, with varying degrees of turbidity, with data recorded on four separate days with sea conditions of smooth, glassy, rough and very rough.

## 5.8 Bottom Pulse Width Investigation

In the previous section (5.6) it was observed (in runs r540 and r533) that the width of the return bottom pulse increased with increasing water turbidity until a point where the pulse began to disappear into the background noise. This is an important observation, as it highlights a deficiency in the 50% bottom pulse detection algorithm. It suggests that in turbid water the 50% pulse detection process will measure depths deeper than true, refer discussion later in this section.

Let us examine the results of run R531 in the region of the turbid area (from time = 31400s to 31560s), refer to figure 29.

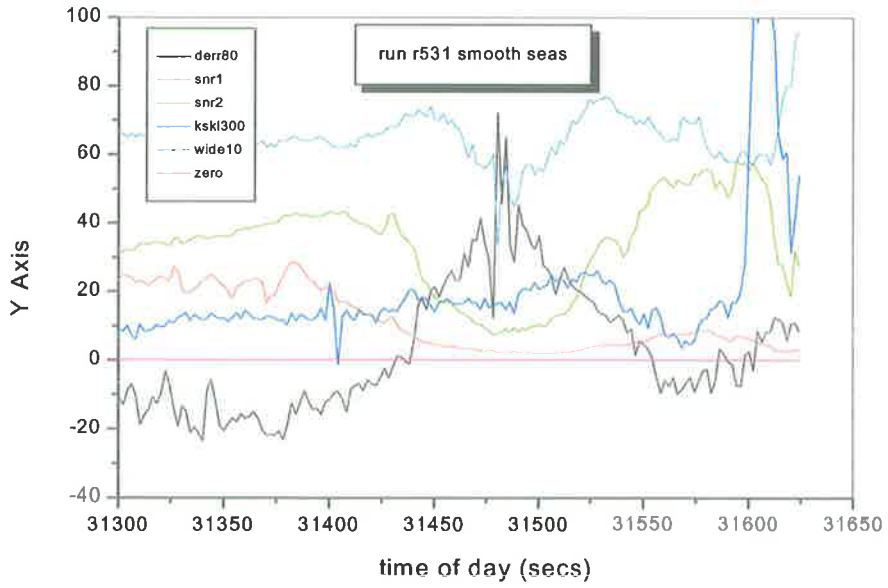


Figure 29 Residual Depth Error Correlation of Run r531

Here it is seen that $d_{err}$ increases from a time of 31400s to a peak at 31480s and then down to a low at 31560s. This increase and decrease in $d_{err}$ is assumed to be the result of photon scattering in turbid seawater. This assumption is supported, by observing the waveforms groups in Figure 30, and noting the loss of the bottom return signal into the background noise.

However, pulse width is expected to increase as seawater turbidity increases and decrease as seawater turbidity decreases. Monte Carlo studies support this assumption [31], as pulse stretching is predicted in turbid seawater, due to the multiple scattering of light.

This expectation however, does not occur absolutely in practice. Referring again to Figure 29, the width of the bottom pulse is seen to increase initially from 31400 s until 31450 s, then decrease to a low at 31480 s, and then increase again to 31530 s before decreasing again to 31560 s.

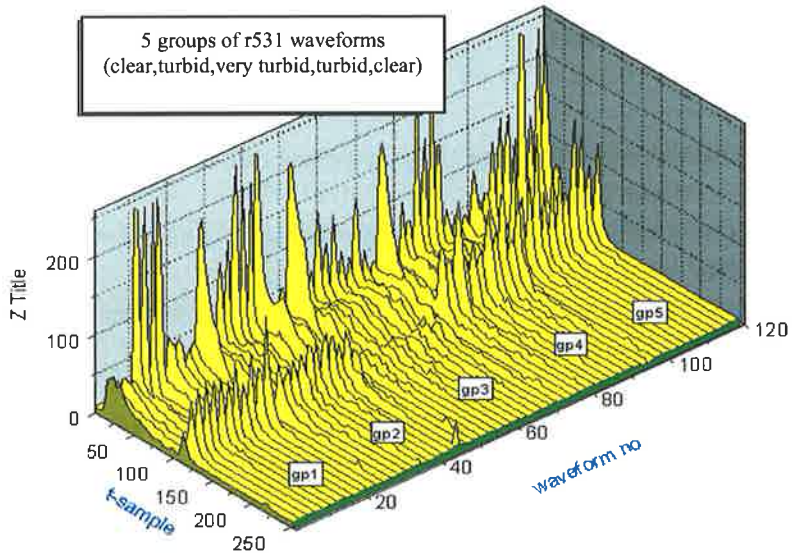


Figure 30 Sample turbidity waveforms

This decrease in pulse width with increasing seawater turbidity is best explained by observing the raw waveforms of Figure 30, which shows five groups of waveforms corresponding to 5 time samples in the region of interest.

| | | | | |
|---|---|---|---|---|
| Grp1 | f154 | 31400 s | 8:43:20 | normal seawater turbidity |
| Grp2 | f179 | 31450 s | 8:44:10 | medium seawater turbidity |
| Grp3 | f194 | 31480 s | 8:44:40 | high seawater turbidity |
| Grp4 | f219 | 31530 s | 8:45:30 | medium seawater turbidity |
| Grp5 | f236 | 31564 s | 8:46:04 | normal seawater turbidity |

This decrease in pulse width with increasing seawater turbidity is explained by observing that the return pulse is gradually lost into the background noise as seawater turbidity becomes high. As seawater turbidity decreases from 31480 s to 31564 s the reverse happens, with the pulse width first increasing before finally decreases as predicted.

The end result is twofold. Firstly pulse width is not a reliable measure of seawater turbidity for very turbid water, and secondly the 50% detecting point of a bottom pulse in very turbid water will result in a positive depth error. This will occur because the bottom section of the pulse is lost in the noise, and the 50% pulse detection point will essentially move towards the peak of the pulse and result in a depth measurement deeper than true.

## 5.9 Discussion

In this chapter the examination of trials data was scrutinized, in an attempt to identify possible causes of error, which were not accounted for in the signal processing methods of chapter 3.

Large depth errors were examined and the following possible causes of depth were identified.

- Platform tilt errors will be reduced by the surface filter but not completely removed.
- Shallow depth errors are sometimes caused by late detection of sea surface by the IR beam.

Benchmark results data was analysed and the following possible causes of depth error were identified.

- Spatial and temporal spreading of the bottom pulses due to seawater turbidity is a significant cause of depth errors.
- Significant depth errors are caused by seawater turbidity, and the existing depth bias models are not effective in removing these errors.
- Weak bottom pulse returns, in very turbid water, result in incorrect 50% bottom pulse detection and produce depth measurements deeper than true.

An experimental depth bias model was developed which showed a considerable improvement, over the existing depth bias models, in reducing residual depth errors.

Error Causes in existing algorithms

- Errors in the determination of the sea surface will result in corresponding errors to depth estimation. Consider the waveform correction to account for the delay in the green surface and bottom laser pulse returns due to non-vertical beams. A correction of $H(\sec(\phi) - 1)$ is made. Any errors in $\phi$ will result in errors in the correction of the green surface and bottom pulse positions and alter in the determination of the corresponding sounding depth.

- Also in rough weather where the sea surface is lumpy early detection of the green surface pulse may occur, which will contribute to sounding depths being estimated deeper than they are.

- In calm weather with a smooth sea surface the selection of nadir waveforms only to detect surface returns is suitable for surface bias determination, but not for sea surface tilt determination. The sensitivity of surface tilt to nadir surface detection is high, as near nadir detection only occur.

# 6. Summary

The major contributions of this thesis are an examination of the signal processing algorithms, the modelling of error propagation and the analysis of data to identify the significant causes of depth error in an Airborne Laser Bathymetry system.

Initially a functional description of a typical ALB system and its signal processing algorithms was established and from it an error model was developed. The error model was used to investigate the susceptibility of the ALB system to error and also to investigate the suitability of the signal processing algorithms used. Finally, the analysis of trials data was used to provide a true evaluation of the depth accuracy of the ALB system and to identify any further causes of depth errors that were not predicted by the error model.

Section 6.1 summarises the identification of depth errors from both error modelling and analysis of experimental data. Section 6.2 recommends improvements and suggests future research and Section 6.3 concludes this thesis.

## 6.1 Summary of identified depth errors

The most significant cause of error was found to be the result of water turbidity. It was predicted in sections 4.11, 4.12 and 4.13 that any errors in the measurement of seawater turbidity would result in significant errors in depth. Also, from the analysis of data, refer section 5.1, it was postulated that large systematic variations in depth error were the result of water turbidity. It was also found, refer section 5.5, that there was some limited correlation between measured turbidity coefficients and depth error. Further analysis of data, refer section 5.6, showed that a bottom pulse signal to noise ratio measurement provided a better correlation with depth error than the turbidity coefficients. A depth bias model using this signal to noise ratio measurement, refer section 5.7 was shown to significantly improve the depth accuracy of the ALB system. However this may be in part due to the error introduced because of the 50% bottom pulse detection algorithm used in the ALB system, refer to section 5.8.

Other errors recognized by the error model, and data analysis are listed following:

- Depth errors due to the analogue to digital algorithm have been shown to be small (section 4.3).
- The waveform storage algorithm has potential to cause significant system depth error, due to errors in the detected position of the IR surface and in the measurement of the scan angle for large scan angles (section 4.4).
- The waveform detection algorithm was found not to introduce any errors of significance (section 4.5).
- The sea surface filter algorithm generally will not result in any significant errors in the estimation of sea surface bias, but may perhaps introduce some minor errors in the estimation of sea surface tilt in smooth seas (section 4.6).
- The sea surface tilt correction algorithm transfers tilt errors to surface and bottom positions and eventually to system depths only for large scan angles (section 4.7).
- The sea bias correction algorithm will directly transfer an error in the estimation of sea surface bias to surface and bottom positions and therefore to system depth (section 4.8).

- The late entry correction algorithm will transfer approximately ¼ of any error in the measured wave trough to the estimated slant depth (section 4.9).
- The surface refraction correction algorithm assumes the refraction of the scanning green laser beam occurs through a horizontal air/water boundary. This may not be the case however, when surface wave action conditions occur, as the green laser beam is spread over 5m at the sea surface some variation in the slope of the air/water boundary is to be expected. Depth errors due to surface refraction were predicted to be negligible especially for small scan angles (section 4.10).
- Tide measurement errors were found to be significant, and any error in the estimation of tide was found to result in a corresponding error in depth (section 4.14).
- Benchmark depths are the measuring stick against which the ALB system depths are tested. Any errors in the estimation of benchmark depths do not contribute to any errors in the ALB system, but they will however directly result in error in the estimation of ALB depth errors (section 4.15).
- It was shown that in smooth seas there were more errors detected than in rough seas. Theoretical analysis suggested that in smooth seas, an apparent sea surface tilt error could result in increased depth error. However the results of data analysis did not support this contention (Section 5.3).
- Large negative depth errors are often associated with the early arrival of the green laser waveform relative to the IR reference surface (refer equation 3.2). Late detection of the IR surface pulse results in $\Delta_1$ being smaller and hence $w_r[s]$ moves to the left. However data analysis showed there was insufficient correlation to correct these errors to significantly improve depth accuracy (Section 5.4).

### 6.2 Recommendations and Future Research

Some suggested improvements to the ALB system and areas for future research are to:

- Provide a more accurate measurement of the angle of the scanning green laser beam. The accurate measurement of the green laser beam scan angle was found to be critical in the calculation of accurate depths.
- Improve the yield and accuracy in the detection of the sea surface by the scanning green laser beam. This will improve the accuracy of the sea surface filter algorithm in the determination of local sea surface bias and tilt.
- Provide a peak bottom pulse detection algorithm (in place of the 50% bottom pulse detection algorithm). In low signal to noise conditions the 50% pulse detection algorithm becomes inaccurate and produces depths deeper than true.
- Investigate the possibility of using a bottom pulse signal to noise ratio measurement in the estimation of water turbidity, and in the development of a more reliable depth bias model. The measurement of a bottom pulse signal to noise ratio is both robust and reliable.

### 6.3 Conclusion

This thesis has investigated the accuracy problems associated with the determination of seawater depth by Airborne Laser Bathymetry. The accurate measurement of depth in shallow waters is of prime importance to the hydrographer, and is fundamental to the creation of reliable charts for coastal shipping. The problem of depth accuracy was analysed in detail by modelling error propagation through the signal processing algorithms of a typical ALB system. Finally the analysis of real trials data was used to investigate benchmark depth comparison data and to

compare system error with system measurement variables. During this investigation several important results were established.

The measurement accuracy of scan angles, the measurement accuracy of the position of the sea surface reference by the IR laser beam, and the measurement accuracy of the sea water attenuation coefficients were found to be critical to the resultant depth accuracy of the ALB system. The last factor, ie turbidity measurement, was the most significant both from a theoretical and experimental point of view. The measurement of tilt by the sea surface filter was also found to be susceptible to error in smooth seas. A depth bias model based on a signal to noise ratio variable was found to be superior to the two-variable depth bias model in current use by the Royal Australian Navy, and the 50% bottom pulse detection method was found to be inaccurate in low signal to noise areas.

# APPENDIX A

# A Simplified Error Model

## A.1 Development of the Model

To explain the development of the model, first consider a simple nonlinear function $y = f(x)$ with one independent variable, refer to Figure A1. Here the error $\delta y$ in calculating y can be estimated given the error $\delta x$ in x as:

$$\delta y = \partial y/\partial x \,.\, \delta x$$

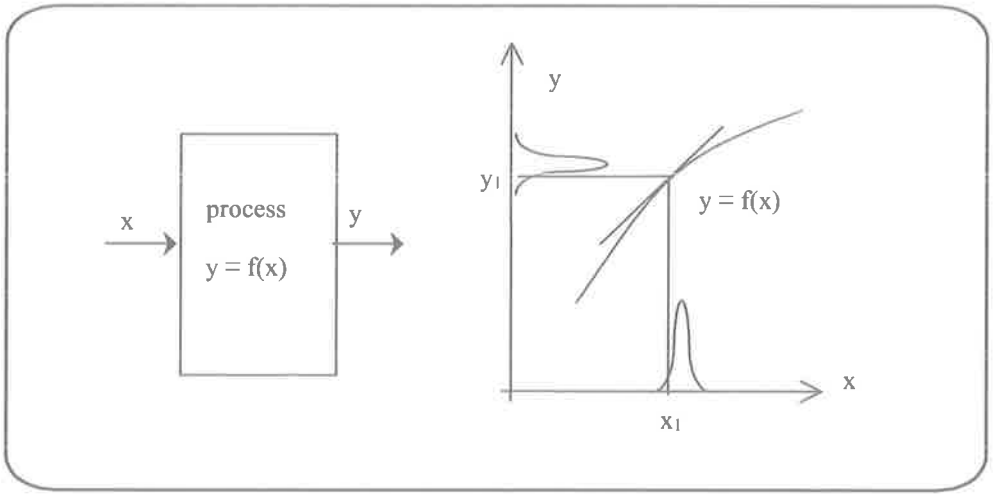


Figure A1 Model development diagram

Now given that an error distribution for the measured independent variable $\delta x$ is random, and provided the function is approximately linear in the region of interest, at say $x_1$, the error distribution of $\delta y$ can be estimated as follows.

The mean error $\mu_{\delta y}$ in $\delta y$ can be determined as:

$$\mu_{\delta y} = E\{\delta y\} = \int p(\delta y).\, \delta y \, dy$$

Now as

$$\delta y = \partial y/\partial x \,.\, \delta x \text{ and } p(\delta y).\, dy = p(\delta x).\, dx$$

we have

$$\mu_{\delta y} = \int p(\delta x)\, (\partial y/\partial x).\, \delta x \, dx$$

and assuming linearity at point $x_1$ we have:

$$\mu_{\delta y} = \partial y/\partial x \,|_{x1} \int p(\delta x) \,.\delta x \, dx$$

or

$$\mu_{\delta y} = \partial y/\partial x \,|_{x1} \,.\mu_{\delta x}$$

Similarly the standard deviation $\sigma_{\delta y}$ in $\delta y$ can be determined as:

$$\sigma^2_{\delta y} = E\{(\delta y - \mu_{\delta y})^2\} = \int (\delta y - \mu_{\delta y})^2 \, p(\delta y) \, dy$$

Now as

$$\delta y = \partial y/\partial x \, . \, \delta x \text{ and } p(\delta y). \, dy = p(\delta x). \, dx$$

we have

$$\sigma^2_{\delta y} = \int (\partial y/\partial x. \, \delta x - \partial y/\partial x. \, \mu_{\delta x})^2 \, p(\delta x) \, dx$$

and assuming linearity at point $x_1$ we have:

$$\sigma^2_{\delta y} = (\partial y/\partial x)^2 \,|_{x1} \int (\delta x - \mu_{\delta x})^2 \, p(\delta x) \, dx$$

or

$$\sigma^2_{\delta y} = (\partial y/\partial x)^2 \,|_{x1} \,.\sigma^2_{\delta x}$$

Thus in summary we have:

$$\mu_{\delta y} = (\partial y/\partial x) \,|_{x1} \,.\mu_{\delta x} \qquad \text{(A.1)}$$

$$\sigma^2_{\delta y} = (\partial y/\partial x)^2 \,|_{x1} \,.\sigma^2_{\delta x} \qquad \text{(A.2)}$$

This can now be expanded to cover multiple input single output functions. For example, consider a three input process $y = f(a,b,c)$. Here the error $\delta y$ in y due to errors $\delta a$, $\delta b$ and $\delta c$ in a, b and c respectively, can be determined as:

$$\delta y = [\partial f(a,b,c)/\partial a] \, \delta a + [\partial f(a,b,c)/\partial b] \, \delta b + [\partial f(a,b,c)/\partial c] \, \delta c \qquad \text{(A.3)}$$

Now providing the error distributions of $\delta a$, $\delta b$ and $\delta c$ are random, statistically independent and assuming the process is linear in the region of interest, at say point $(a_1,b_1,c_1)$, then the mean and standard deviation of the error distribution in $\delta y$ can be estimated as follows.

$$\begin{aligned} \mu_{\delta y} &= \partial f(a,b,c)/\partial a \,|_{a1,b1,c1} \, \mu_{\delta a} + \partial f(a,b,c)/\partial b \,|_{a1,b1,c1} \, \mu_{\delta b} + \partial f(a,b,c)/\partial c \,|_{a1,b1,c1} \, \mu_{\delta c} \\ \sigma^2_{\delta y} &= (\partial f(a,b,c)/\partial a)^2 \,|_{a1,b1,c1} \sigma_{\delta a}{}^2 + (\partial f(a,b,c)/\partial b)^2 \,|_{a1,b1,c1} \sigma_{\delta b}{}^2 + (\partial f(a,b,c)/\partial c)^2 \,|_{a1,b1,c1} \sigma_{\delta c}{}^2 \end{aligned} \qquad \text{(A.4)}$$

## A.2 The Resulting Error Model

By applying equations A.4 to the processing functions of an airborne laser bathymetry system, as detailed in chapter 4, we have in summary:

**Constants**

c = 2.99774e8 ------speed of light in air in metres per second

$\Delta t$ = 2e-9 -------sample time in seconds (ie $\Delta t$ = 2ns)

$H = 500$ -------height of aircraft above sea level in metres
$\eta_w = 1.3389$ -------refractive index of air to seawater
$f_{sd} = 64$ ------full scale deflection of data
$n = 6$ -------number of bit accuracy of data
$d_{2r} = pi/180.0$ ------degrees to radian conversion
$t_{2d} = (c\ \Delta t)/(2\eta_w)$ ----calc 2 ns sample time to distance conversion

**A/D Conversion (in seconds)**

Inputs($m_{s1}$, $m_{s2}$, $m_{b1}$, $m_{b2}$) , where ms1, ms2, mb1 and mb2 are the slopes of the waveform pulses at the quantization points.

$$\mu_{\delta tqs1} = \mu_{\delta tqs2} = \mu_{\delta tqb1} = \mu_{\delta tqb2} = 0$$
$$\sigma^2_{\delta tqs1} = (1/12)\ (fsd/(2^n\text{-}1))^2\ (\Delta t/m_{s1})^2$$
$$\sigma^2_{\delta tqs2} = (1/12)\ (fsd/(2^n\text{-}1))^2\ (\Delta t/m_{s2})^2$$
$$\sigma^2_{\delta tqb1} = (1/12)\ (fsd/(2^n\text{-}1))^2\ (\Delta t/m_{b1})^2$$
$$\sigma^2_{\delta tqb2} = (1/12)\ (fsd/(2^n\text{-}1))^2\ (\Delta t/m_{b2})^2$$

**Digital Waveform Storage (in number of samples)**

Inputs ($\sigma_{\delta kIR}$, $\Phi_1$, $\sigma_{\delta H}$, $\sigma_{\delta \Phi 1}$)

$$\mu_{\delta s} = -\mu_{\delta kIR} - [2(\sec\Phi_1 - 1)/(c\Delta t)]\ \mu_{\delta H} - [(2H/c\Delta t)(\sec^2\Phi_1)(\sin\Phi_1)]\ \mu_{\delta\Phi 1}$$
$$\sigma^2_{\delta s} = \sigma^2_{\delta kIR} + [2(\sec\Phi_1 - 1)/(c\Delta t)]^2\ \sigma^2_{\delta H} + [(2H/c\Delta t)(\sec^2\Phi_1)(\sin\Phi_1)]^2\ \sigma^2_{\delta\Phi 1}$$

**Waveform detection (in metres)**

Inputs ($s_{f1}$, $s_{b1}$)

$$\mu_{\delta t1} = 0$$
$$\mu_{\delta sf1} = (c\Delta t/2\eta_w)\ \mu_{\delta s}$$
$$\mu_{\delta sb1} = (c\Delta t/2\eta_w)\ \mu_{\delta s}$$
$$\sigma^2_{\delta t1} = (0.1/\sqrt{12})^2(\Delta t)^2 \qquad (4.8)$$
$$\sigma^2_{\delta sf1} = (c\Delta t/2\eta_w)^2\ \sigma^2_{\delta s} + (c/2\eta_w)^2\ \sigma^2_{\delta tqs1} + (c/2\eta_w)^2\ \sigma^2_{\delta tqs2} + (c/2\eta_w)^2\ \sigma^2_{\delta tl}$$
$$\sigma^2_{\delta sb1} = (c\Delta t/2\eta_w)^2\ \sigma^2_{\delta s} + (c/2\eta_w)^2\ \sigma^2_{\delta tqb1} + (c/2\eta_w)^2\ \sigma^2_{\delta tqb2} + (c/2\eta_w)^2\ \sigma^2_{\delta tl}$$

**Sea Surface Filter Calculation**

Inputs (b, $\Delta\Phi$, R)

$$\partial b/\partial s_{f1} = \cos(\Phi_1+\Delta\Phi)$$
$$\partial b/\partial\Phi_1 = H\sin\Phi_1\cos(\Phi_1+\Delta\Phi)/\cos^2\Phi_1 - (s_{f1} - s_{wave} + H/\cos\Phi_1)\sin(\Phi_1+\Delta\Phi)$$
$$\partial\Delta\Phi/\partial s_{f1} = (H+b)/((s_{f1}\text{-}s_{wave}+H/\cos\Phi_1)((s_{f1}\text{-}s_{wave}+H/\cos\Phi_1)^2\text{-}(H+b)^2)^{1/2})$$
$$\partial\Delta\Phi/\partial\Phi_1 = H(H+b)\sin(\Phi_1)\ /$$
$$(\cos^2\Phi_1(s_{f1}\text{-}s_{wave}+H/\cos\Phi_1)((s_{f1}\text{-}s_{wave}+H/\cos\Phi_1)^2\text{-}(H+b)^2)^{1/2})$$

$$\mu_{\delta b} = R(\partial b/\partial s_{f1})\ \mu_{\delta sf1} + R(\partial b/\partial\Phi_1)\ \mu_{\delta\Phi 1}$$
$$\mu_{\delta\Delta\Phi} = R(\partial\Delta\Phi/\partial s_{f1})\ \mu_{\delta sf1} + R(\partial\Delta\Phi/\partial\Phi_1)\ \mu_{\delta\Phi 1}$$
$$\sigma^2_{\delta b} = R^2(\partial b/\partial s_{f1})^2\ \sigma^2_{\delta sf1} + R^2(\partial b/\partial\Phi_1)^2\ \sigma^2_{\delta\Phi 1}$$
$$\sigma^2_{\delta\Delta\Phi} = R^2(\partial\Delta\Phi/\partial s_{f1})^2\ \sigma^2_{\delta sf1} + R^2(\partial\Delta\Phi/\partial\Phi_1)^2\ \sigma^2_{\delta\Phi 1}$$

**Sea Surface Tilt correction**

$s_{f2} = s_{f1} - (H/\eta_w)\sec^2\Phi_1 \sin\Phi_1 \Delta\Phi;$
$s_{b2} = s_{b1} - (H/\eta_w)\sec^2\Phi_1 \sin\Phi_1 \Delta\Phi;$
$\Phi_2 = \Phi_1 + \Delta\Phi;$

$\mu_{\delta sf2} = \mu_{\delta sf1} - [(H/\eta_w)(1/\cos\Phi_1 + 2\sin^2\Phi_1/\cos^3\Phi_1)(\Delta\Phi)]\,\mu_{\delta\Phi 1} - [(H/\eta_w)(\sin\Phi_1/\cos^2\Phi_1)]\,\mu_{\delta\Delta\Phi}$
$\mu_{\delta sb2} = \mu_{\delta sb1} - [(H/\eta_w)(1/\cos\Phi_1 + 2\sin^2\Phi_1/\cos^3\Phi_1)(\Delta\Phi)]\,\mu_{\delta\Phi 1} - [(H/\eta_w)(\sin\Phi_1/\cos^2\Phi_1)]\,\mu_{\delta\Delta\Phi}$
$\mu_{\delta\Phi 2} = \mu_{\delta\Phi 1} + \mu_{\delta\Delta\Phi}$
$\sigma^2_{\delta sf2} = \sigma^2_{\delta sf1} + [(H/\eta_w)(1/\cos\Phi_1 + 2\sin^2\Phi_1/\cos^3\Phi_1)(\Delta\Phi)]^2\,\sigma^2_{\delta\Phi 1} + [(H/\eta_w)(\sin\Phi_1/\cos^2\Phi_1)]^2\,\sigma^2_{\delta\Delta\Phi}$
$\sigma^2_{\delta sb2} = \sigma^2_{\delta sb1} + [(H/\eta_w)(1/\cos\Phi_1 + 2\sin^2\Phi_1/\cos^3\Phi_1)(\Delta\Phi)]^2\,\sigma^2_{\delta\Phi 1} + [(H/\eta_w)(\sin\Phi_1/\cos^2\Phi_1)]^2\,\sigma^2_{\delta\Delta\Phi}$
$\sigma^2_{\delta\Phi 2} = \sigma^2_{\delta\Phi 1} + \sigma^2_{\delta\Delta\Phi}$

**Sea Surface Bias Correction**

$s_{f3} = s_{f2} - b;$
$s_{b3} = s_{b2} - b;$

$\mu_{\delta sf3} = \mu_{\delta sf2} - \mu_{\delta b}$
$\mu_{\delta sb3} = \mu_{\delta sb2} - \mu_{\delta b}$
$\sigma^2_{\delta sf3} = \sigma^2_{\delta sf2} + \sigma^2_{\delta b}$
$\sigma^2_{\delta sb3} = \sigma^2_{\delta sb2} + \sigma^2_{\delta b}$

**Late Entry Correction**

$s_{b4} = s_{b3} + (1-1/\eta_w)\,s_{f3}$

$\mu_{\delta sb4} = \mu_{\delta sb3} + [1-1/\eta_w]\,\mu_{\delta sf3}$
$\sigma^2_{\delta sb4} = \sigma^2_{\delta sb3} + [1-1/\eta_w]^2\,\sigma^2_{\delta sf3}$

**Surface Refraction Correction**

$d_1 = \sqrt{(1-(\sin\Phi_2/\eta_w)^2)}\,s_{b4}$

$\mu_{\delta d1} = \sqrt{[1-(\sin\Phi_2/\eta_w)^2]}\,\mu_{\delta sb4} - [(s_{b4}/n^2_w)(\sin\Phi_2.\cos\Phi_2)/(\sqrt{(1-(\sin\Phi_2/\eta_w)^2)})]\,\mu_{\delta\Phi 2}$
$\sigma^2_{\delta d1} = [1-(\sin\Phi_2/\eta_w)^2]\,\sigma^2_{\delta sb4} + [(s_{b4}/n^2_w)(\sin\Phi_2.\cos\Phi_2)/(\sqrt{(1-(\sin\Phi_2/\eta_w)^2)})]^2\,\sigma^2_{\delta\Phi 2}$

**Turbidity determination**

Inputs( $k_L$, $k_S$, $\sigma_{\delta kL}$, $\sigma_{\delta kS}$ )

## Determine Forward scatter

Inputs($E_{bf}$, $\sigma_{Ebf}$)

$$b_f = f(k_S, k_L) + E_{bf}$$

$$\mu_{\delta bf} = (\partial b_f / \partial k_S)\, \mu_{\delta kS} + (\partial b_f / \partial k_L)\, \mu_{\delta kL} + \mu_{Ebf}$$
$$\sigma^2_{\delta bf} = (\partial b_f / \partial k_S)^2\, \sigma^2_{\delta kS} + (\partial b_f / \partial k_L)^2\, \sigma^2_{\delta kL} + \sigma^2_{Ebf}$$

## Depth Bias Correction

Inputs($E_{bias}$, $\sigma_{Ebias}$)

$$d_2 = d_1 - d_{bias}(d_1, \Phi_2, b_f) + E_{bias}$$

$$\mu_{\delta d2} = \mu_{\delta d1} - (\partial d_{bias} / \partial d_1)\, \mu_{\delta d1} - (\partial d_{bias} / \partial \Phi_2)\, \mu_{\delta \Phi 2} - (\partial d_{bias} / \partial b_f)\, \mu_{\delta bf} + \mu_{Ebias}$$
$$\sigma^2_{\delta d2} = \sigma^2_{\delta d1} + (\partial d_{bias}/\partial d_1)^2\, \sigma^2_{\delta d1} + (\partial d_{bias}/\partial \Phi_2)^2\, \sigma^2_{\delta \Phi 2} + (\partial d_{bias}/\partial b_f)^2\, \sigma^2_{\delta bf} + \sigma^2_{Ebias}$$

## Tide Correction

Inputs($d_{tide}$, $\sigma_{\delta dtide}$)

$$d_{lads} = d_2 - d_{tide}$$

$$\mu_{\delta dlads} = \mu_{\delta d2} - \mu_{\delta dtide}$$
$$\sigma^2_{\delta dlads} = \sigma^2_{\delta d2} + \sigma^2_{\delta dtide}$$

## Benchmark Comparison

Inputs($d_{bm}$, $E_{bmc}$, $\sigma_{\delta dbm}$, $\sigma_{\delta Ebmc}$)

$$d_{err} = d_{lads} - d_{bm} + E_{bmc}$$

$$\mu_{\delta derr} = \mu_{\delta dlads} - \mu_{\delta dbm} + \mu_{Ebmc} \cong 0$$
$$\sigma^2_{\delta derr} = \sigma^2_{\delta dlads} + \sigma^2_{\delta dbm} + \sigma^2_{Ebmc}$$

# APPENDIX B

## Sea Surface Filter Sensitivity Calculations

This appendix examines the sensitivity of the errors in the sea surface filter output variables (b, $\Delta\Phi$) to errors in the input variables ($s_{fl}$, $\Phi_l$). The accuracy of the platform tilt ($\alpha$) or measurement of apparent sea surface tilt ($\Delta\Phi$) in particular, is examined for smooth sea conditions. Also, the effect of errors in the calculation of the sea surface bias error (b) is examined for rough sea conditions.

### B.1 Introduction

Sea surface position measurements ($s_{fl}$) from reflections of the scanning green laser beam and the related laser beam scan angle ($\Phi$) are input into a Kalman filter to calculate any apparent sea-surface tilt ($\Delta\Phi$) and sea surface bias (b), refer 3.4. These output values are used to estimate the mean sea level from which sea depth is measured.

### B.2 Laser Platform Tilt Analysis

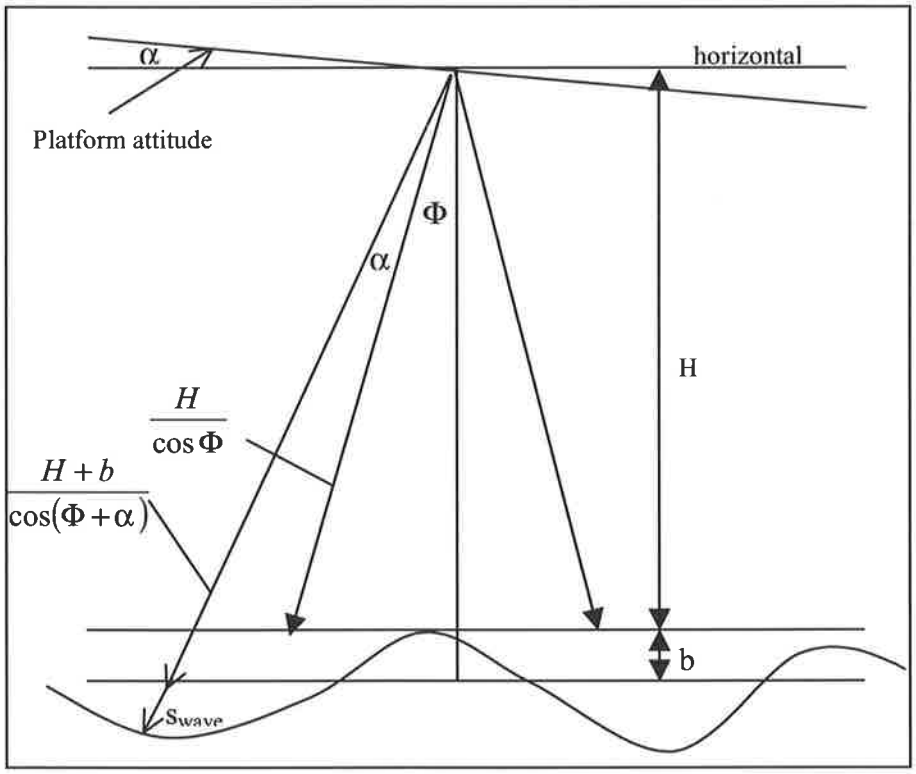


Figure B1 Sea Surface Filter Analysis Diagram

In the following analysis, a platform tilt ($\alpha$) is assumed, for a scanning green laser beam angle $\Phi$. From the system geometry, refer Figure B1, the expected surface position ($s_{fl}$) and sea surface bias (b) measurements can be calculated as follows:

$$s_{fl} = \frac{(H+b)}{\cos(\Phi+\alpha)} + s_{wave} - \frac{H}{\cos\Phi}, \quad \text{where } \Phi = \text{abs}(\Phi). \tag{B.2}$$

Rearranging we have:

$$b = \left( s_{f1} - s_{wave} + \frac{H}{\cos\Phi} \right) \cos(\Phi + \alpha) - H$$

$$\alpha = ar\cos\left( \frac{(H+b)}{\left( s_{f1} - s_{wave} + \frac{H}{\cos\Phi} \right)} \right) - \Phi = \Delta\Phi \tag{B.3}$$

and now the sensitivity of b and $\Delta\Phi$ to $s_{f1}$ and $\Phi$ can be determined as:

$$\frac{\partial b}{\partial s_{f1}} = \cos(\Phi + \alpha)$$

$$\frac{\partial b}{\partial \Phi} = \frac{H \sin\Phi \cos(\Phi + \alpha)}{\cos^2\Phi} - \left( s_{f1} - s_{wave} + \frac{H}{\cos\Phi} \right) \sin(\Phi + \alpha)$$

(B.4)

$$\frac{\partial \Delta\Phi}{\partial s_{f1}} = \frac{(H+b)}{\left( s_{f1} - s_{wave} + \frac{H}{\cos\Phi} \right) \left( \left[ \left( s_{f1} - s_{wave} + \frac{H}{\cos\Phi} \right)^2 - (H+b)^2 \right] \right)^{1/2}}$$

$$\frac{\partial \Delta\Phi}{\partial \Phi} = \frac{H(H+b)\sin\Phi}{\cos^2\Phi \left( s_{f1} - s_{wave} + \frac{H}{\cos\Phi} \right) \left( \left( s_{f1} - s_{wave} + \frac{H}{\cos\Phi} \right)^2 - (H+b)^2 \right)^{1/2}}$$

and the output errors as:

$$\delta b = R \frac{\partial b}{\partial s_{f1}} \delta s_{f1} + R \frac{\partial b}{\partial \Phi} \delta\Phi$$

$$\delta \Delta\Phi = R \frac{\partial \Delta\Phi}{\partial s_{f1}} \delta s_{f1} + R \frac{\partial \Delta\Phi}{\partial \Phi} \delta\Phi \tag{B.5}$$

where R is a filter reduction factor to account for the filtering effect of the sea surface Kalman filter.

An exponential filter is used to approximate the Kalman filtering giving:

$$y_i = (1 - \alpha_f) x_i + (\alpha_f) x_{i-1}$$

and

$$\sigma_{out} = \sqrt{\frac{1-\alpha_f}{1+\alpha_f}}\sigma_{in} = R\sigma_{in}$$

where

$$R = \sqrt{\frac{1-\alpha_f}{1+\alpha_f}}$$

R is the required filter reduction factor, and $\alpha_f$ is the filter factor.

Computing results for some typical conditions, with no filtering effect (ie for R=1) we have:

| H (m) | Φ (deg) | b (m) | α (deg) | | $\partial b/\partial s_{fl}$ (m/m) | $\partial b/\partial \Phi$ (m/deg) | $\partial \Delta\Phi/\partial s_{fl}$ (deg/m) | $\partial \Delta\Phi/\partial \Phi$ (deg/deg) |
|---|---|---|---|---|---|---|---|---|
| 500 | 1 | 0 | 1 | | 0.999 | -0.153 | 3.280 | 0.500 |
| 500 | 15 | 0 | 1 | | 0.961 | -0.175 | 0.384 | 0.930 |
| 500 | 1 | 1 | 1 | | 0.999 | -0.153 | 3.273 | 0.499 |
| 500 | 15 | 1 | 1 | | 0.961 | -0.180 | 0.383 | 0.928 |

These results clarify some important factors.

Firstly it is noted that the sensitivity $\partial\Delta\Phi/\partial s_{fl}$ is significantly larger for small scan angles Φ than for large scan angles. Results show that for a platform tilt of $\alpha$=1° that the sensitivity in the measurement of tilt to surface position $\partial\Delta\Phi/\partial s_{fl}$=3.280 deg/m is larger at a small scan angle Φ=1° compared to $\partial\Delta\Phi/\partial s_{fl}$=0.384 deg/m at a larger scan angle of Φ=15°. This result indicates that in smooth seas, where valid surface returns normally only occur for small scan angles, that the accuracy of the platform tilt estimation algorithm, will be significantly worse than in rough seas.

Secondly the results show that the sensitivities $\partial b/\partial s_{fl}$ and $\partial b/\partial\Phi$ in the determination of sea surface bias are almost identical in rough seas when b=1 compared with flat seas when b=0. However, it should be noted that, the error in determining sea bias $\delta b$ depends on other factors, refer to equation B.5. In particular, $\delta s_{fl}$ the error in the measurement of surface position is likely to be larger in rough seas due to the distortion of the surface pulse waveform.

Nevertheless, the filtering effect of the surface filter will reduce these effects as the filter reduction factor R becomes smaller as more filtering is applied. R=1/3 to 1/4 is assumed to satisfy normal operational filtering requirements.

# APPENDIX C

# Dependency of Depth Errors on the Early Detected Position of the Sea Surface by Green Laser Pulses

## C.1 Introduction

This appendix examines the dependence of depth errors on the position of green surface reflection pulses in flat sea conditions. In rough seas, wave action will displace the position of the surface pulse away from the mean sea surface and the correlation of depth error with surface position would be difficult to establish. However, if it can be shown (in flat seas) that depth errors occur related to the corresponding position of green surface pulses, then the possibility of reducing depth errors for this situation may be possible. Benchmark data from flat sea sorties s332 and s333 were analysed.

The data provides the time, the benchmark number and depth error ($d_{err}$), as defined in para 4.15, for all benchmark comparisons in smooth and glassy seas. The corresponding waveform data, provides the laser waveforms, from which the time of the surface pulses ($t_s$) can be extracted, and the position of the surface pulses ($s_{f1}$) calculated, refer para 3.3.1.

All the $d_{err}$ and corresponding $s_{f1}$ data were compiled for each benchmark area for each trial run for sorties s332 and s333. The sample mean and standard deviation of this data were calculated, using equations C1 and C2,

$$\bar{d}_{err} = \frac{\sum_{i=1}^{N} d_{err,i}}{N} \qquad \sigma_{d_{err}} = \sqrt{\frac{1}{N-1}\sum_{i=1}^{N}\left(d_{err,i} - \bar{d}_{err}\right)^2} \qquad \text{C.1}$$

$$\bar{s}_{f1} = \frac{\sum_{i=1}^{N} s_{f1,i}}{N} \qquad \sigma_{s_{f1}} = \sqrt{\frac{1}{N-1}\sum_{i=1}^{N}\left(s_{f1,i} - \bar{s}_{f1}\right)^2} \qquad \text{C.2}$$

and the data normalized using equations C3.

$$s_{norm,i} = \left(\frac{s_{f1,i} - \bar{s}_{f1}}{\sigma_{s_{f1}}}\right) \qquad d_{norm,i} = \left(\frac{d_{err,i} - \bar{d}_{err}}{\sigma_{d_{err}}}\right) \qquad \text{C.3}$$

A surface position zone $z_{s,i}$ was defined for each $s_{norm,i}$ as

$$z_{s,i} = round\left(s_{norm,i}\right) + 4 \qquad \text{such that} \quad 1 \le z_{s,i} \le 7 \qquad \text{C.4}$$

Now, for each surface position zone ($z_s$) in each benchmark area in each run, the percentage yield of $d_{norm}$ that is within ½ a std of the position of its corresponding $s_{norm}$ can be determined:

$$p_{yield} = \frac{yield}{total} 100\% \qquad \text{C.5}$$

where total is the number of surface positions within each zone and yield is the number of depth error within ½ std of its corresponding surface position.

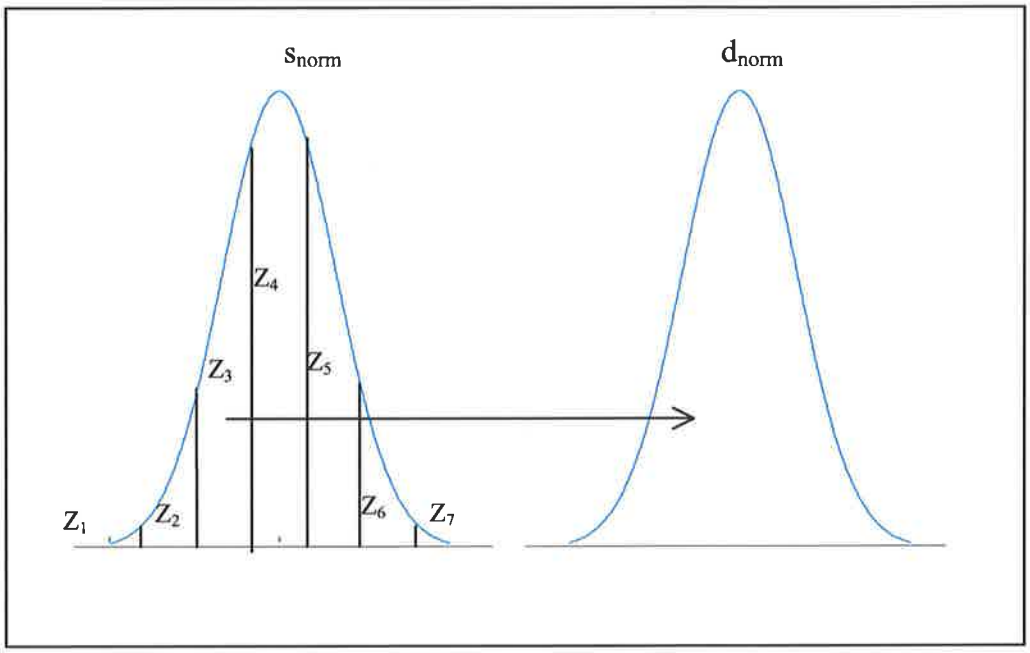


Figure C1 Depth Yield Dependency Diagram

For example consider the 7th measurement pair of surface position ($s_{fl,7}$) and depth error ($d_{err,7}$), and assume their normalised values are:

$$s_{norm,7} = 0.73 \quad \text{and} \quad d_{norm,7} = 1.10.$$

Now the surface position zone for the 7th surface position can be determined as:

$$z_{s,7} = \text{round}(0.73) + 4 = 5$$

and because the normalised depth error ($d_{norm,7} = 1.10$) lies within the range $0.73 \pm 0.5$, the result is a yield.

Performing this operation on all sample pairs; yields for all 7 zones can be found. The percentage yields are then calculated using equation C.5.

The percentage yield figure is therefore a measure of the dependency of depth error on the position of the surface pulse position to within ½ a standard deviation.

## C.2 Results

The following results, refer table C1, were obtained for all 20 benchmark areas within runs, r531, r532, r540, r533 and r534.

## C.3 Conclusions

The results are inconclusive and do not indicate a high dependence of depth errors on surface position. The highest percentage yields are between 30 to 40% and are generally achieved in zones 3, 4 and 5. In any case a much higher dependency of depth errors on surface positions would be required before any significant reduction in depth error using this phenomena, could be achieved.

### Table C1 Depth Dependency Percentage Yield Results

| run | r531 | (57813 samples) | | | | | | |
|---|---|---|---|---|---|---|---|---|
| bm | z1 | z2 | z3 | z4 | z5 | z6 | z7 | totals |
| 1 | 0.000 | 11.194 | 29.870 | 36.597 | 33.722 | 18.868 | 0.000 | 31.836 |
| 2 | 19.355 | 15.238 | 28.405 | 37.661 | 34.486 | 21.429 | 0.000 | 32.477 |
| 3 | 15.789 | 14.000 | 21.971 | 40.649 | 34.660 | 14.493 | 0.000 | 33.427 |
| 4 | 19.231 | 10.976 | 29.087 | 42.404 | 40.989 | 23.958 | 0.000 | 36.465 |
| 5 | 20.588 | 12.375 | 23.577 | 39.648 | 30.869 | 22.989 | 0.000 | 31.243 |
| 6 | 32.143 | 13.878 | 21.749 | 39.376 | 28.449 | 15.714 | 0.000 | 28.960 |
| 7 | 0.000 | 13.600 | 30.323 | 36.822 | 22.904 | 11.628 | 0.000 | 27.679 |
| 8 | 0.000 | 19.205 | 34.248 | 38.423 | 22.554 | 11.837 | 0.000 | 29.860 |
| 9 | 0.000 | 21.687 | 34.550 | 39.400 | 28.360 | 19.205 | 0.000 | 32.027 |
| 10 | 14.286 | 12.195 | 23.793 | 33.089 | 22.981 | 12.500 | 0.000 | 24.986 |
| 11 | 0.000 | 20.792 | 31.649 | 38.603 | 24.375 | 6.112 | 0.000 | 29.619 |
| 12 | 0.000 | 24.204 | 34.902 | 39.493 | 27.766 | 7.407 | 1.408 | 32.728 |
| 13 | 33.333 | 13.235 | 33.231 | 40.481 | 29.258 | 3.846 | 0.000 | 32.480 |
| 14 | 0.000 | 13.333 | 29.060 | 38.095 | 32.727 | 3.333 | 0.000 | 30.383 |
| 15 | 0.000 | 21.429 | 33.921 | 40.553 | 23.839 | 2.844 | 2.703 | 31.772 |
| 16 | 0.000 | 17.901 | 25.133 | 34.477 | 21.272 | 12.459 | 40.000 | 25.649 |
| 17 | 0.000 | 28.462 | 32.911 | 38.833 | 32.801 | 16.967 | 3.226 | 32.867 |
| 18 | 0.000 | 17.778 | 33.071 | 34.772 | 27.207 | 12.092 | 0.000 | 29.803 |
| 19 | 23.077 | 20.922 | 32.514 | 42.721 | 33.851 | 24.000 | 0.000 | 35.032 |
| 20 | 0.000 | 9.412 | 23.944 | 40.162 | 35.025 | 2.778 | 0.000 | 31.108 |

| run | r532 | (60787 samples)) | | | | | | |
|---|---|---|---|---|---|---|---|---|
| bm | z1 | z2 | z3 | z4 | z5 | z6 | z7 | totals |
| 1 | 16.667 | 8.696 | 25.050 | 37.383 | 31.920 | 20.000 | 0.000 | 30.418 |
| 2 | 13.333 | 8.052 | 22.110 | 38.126 | 31.870 | 19.847 | 0.000 | 29.846 |
| 3 | 7.500 | 9.059 | 23.377 | 36.897 | 32.583 | 13.253 | 0.000 | 30.099 |
| 4 | 9.091 | 16.949 | 18.029 | 34.626 | 27.658 | 13.333 | 0.000 | 26.180 |
| 5 | 23.529 | 20.000 | 23.648 | 35.053 | 33.868 | 19.259 | 25.000 | 30.085 |
| 6 | 13.793 | 12.105 | 23.759 | 36.583 | 35.170 | 27.206 | 0.000 | 30.856 |
| 7 | 0.000 | 10.753 | 25.043 | 33.672 | 28.833 | 14.754 | 100.000 | 27.307 |
| 8 | 19.048 | 9.467 | 26.029 | 36.654 | 24.912 | 9.677 | 0.000 | 27.366 |

| | | | | | | | | |
|---|---|---|---|---|---|---|---|---|
| 9 | 8.333 | 13.008 | 27.104 | 37.018 | 26.062 | 10.345 | 0.000 | 28.627 |
| 10 | 0.000 | 12.727 | 29.975 | 37.324 | 19.248 | 10.440 | 0.000 | 26.547 |
| 11 | 23.529 | 18.557 | 24.028 | 39.149 | 27.884 | 6.573 | 20.000 | 28.623 |
| 12 | 20.000 | 14.493 | 28.486 | 39.706 | 21.669 | 17.677 | 8.333 | 29.218 |
| 13 | 0.000 | 7.692 | 28.615 | 38.071 | 16.372 | 8.602 | 10.000 | 26.636 |
| 14 | 0.000 | 21.053 | 30.693 | 43.038 | 22.222 | 10.000 | 0.000 | 31.915 |
| 15 | 0.000 | 16.535 | 23.716 | 37.513 | 21.565 | 8.300 | 12.500 | 26.335 |
| 16 | 35.714 | 20.497 | 24.277 | 37.408 | 27.182 | 15.194 | 18.182 | 28.356 |
| 17 | 50.000 | 21.930 | 30.465 | 42.685 | 33.378 | 20.798 | 6.667 | 34.171 |
| 18 | 0.000 | 17.757 | 27.615 | 40.327 | 29.391 | 8.108 | 3.846 | 30.334 |
| 19 | 28.571 | 20.280 | 35.549 | 40.798 | 30.738 | 13.333 | 0.000 | 34.082 |
| 20 | 33.333 | 5.063 | 14.356 | 55.614 | 43.774 | 9.259 | 0.000 | 36.985 |

| run | r540 | (60335 samples) | | | | | | |
|---|---|---|---|---|---|---|---|---|
| bm | z1 | z2 | z3 | z4 | z5 | z6 | z7 | totals |
| 1 | 15.217 | 12.329 | 25.771 | 36.706 | 28.501 | 18.750 | 33.333 | 29.497 |
| 2 | 14.286 | 11.314 | 22.727 | 41.280 | 35.344 | 18.310 | 0.000 | 32.666 |
| 3 | 8.333 | 16.402 | 24.094 | 34.806 | 26.859 | 17.178 | 0.000 | 27.407 |
| 4 | 0.000 | 15.000 | 19.252 | 35.181 | 22.295 | 11.558 | 14.286 | 23.659 |
| 5 | 0.000 | 20.625 | 27.096 | 34.425 | 21.339 | 7.420 | 0.000 | 25.891 |
| 6 | 0.000 | 12.632 | 26.072 | 32.858 | 21.007 | 9.968 | 11.111 | 25.200 |
| 7 | 0.000 | 16.667 | 25.441 | 37.836 | 18.842 | 8.133 | 9.091 | 26.324 |
| 8 | 0.000 | 20.000 | 30.757 | 34.642 | 25.050 | 16.974 | 3.704 | 28.941 |
| 9 | 0.000 | 18.548 | 29.184 | 36.806 | 21.379 | 9.286 | 0.000 | 27.651 |
| 10 | 0.000 | 19.149 | 32.494 | 37.939 | 25.968 | 6.209 | 0.000 | 30.500 |
| 11 | 0.000 | 32.394 | 35.757 | 39.972 | 30.827 | 7.837 | 1.370 | 33.369 |
| 12 | 20.000 | 22.047 | 34.708 | 43.005 | 19.806 | 7.819 | 1.282 | 32.842 |
| 13 | 0.000 | 14.583 | 35.897 | 42.570 | 27.322 | 6.329 | 12.121 | 33.795 |
| 14 | 0.000 | 12.500 | 28.358 | 29.630 | 10.476 | 3.846 | 0.000 | 22.010 |
| 15 | 0.000 | 14.000 | 29.067 | 36.042 | 17.063 | 5.063 | 0.000 | 26.513 |
| 16 | 0.000 | 21.538 | 30.868 | 35.457 | 22.762 | 6.824 | 0.000 | 28.260 |
| 17 | 13.333 | 19.774 | 32.329 | 37.943 | 32.031 | 15.544 | 5.195 | 32.379 |
| 18 | 100.000 | 34.839 | 30.947 | 54.749 | 49.817 | 32.524 | 6.667 | 47.029 |
| 19 | 50.000 | 20.091 | 28.713 | 48.039 | 41.026 | 35.417 | 2.000 | 40.221 |
| 20 | 0.000 | 2.222 | 15.060 | 39.789 | 13.504 | 6.667 | 0.000 | 20.459 |

| run | r533 | (58940 samples) | | | | | | |
|---|---|---|---|---|---|---|---|---|
| bm | z1 | z2 | z3 | z4 | z5 | z6 | z7 | totals |
| 1 | 13.793 | 8.750 | 28.859 | 36.814 | 30.241 | 10.714 | 0.000 | 30.376 |
| 2 | 12.500 | 12.217 | 22.321 | 36.223 | 31.829 | 22.414 | 50.000 | 30.012 |
| 3 | 21.622 | 14.884 | 19.248 | 35.000 | 31.610 | 11.207 | 0.000 | 28.454 |

| | | | | | | | | |
|---|---|---|---|---|---|---|---|---|
| 4 | 18.182 | 9.524 | 20.845 | 33.333 | 23.746 | 13.043 | 0.000 | 24.702 |
| 5 | 26.667 | 17.791 | 25.280 | 37.077 | 26.420 | 10.494 | 0.000 | 28.269 |
| 6 | 23.684 | 20.588 | 23.096 | 34.786 | 26.927 | 12.000 | 0.000 | 28.072 |
| 7 | 22.917 | 23.464 | 26.362 | 35.849 | 23.814 | 11.811 | 0.000 | 28.616 |
| 8 | 11.765 | 19.072 | 23.114 | 37.332 | 30.133 | 10.559 | 0.000 | 29.712 |
| 9 | 35.000 | 17.391 | 21.207 | 36.707 | 26.917 | 7.547 | 0.000 | 27.645 |
| 10 | 25.000 | 13.100 | 23.444 | 39.680 | 32.171 | 8.511 | 50.000 | 30.665 |
| 11 | 22.222 | 15.000 | 27.273 | 40.842 | 29.688 | 16.327 | 0.000 | 31.414 |
| 12 | 0.000 | 0.000 | 21.739 | 38.889 | 20.690 | 28.571 | 0.000 | 26.214 |
| 13 | 12.500 | 16.575 | 20.460 | 40.193 | 37.115 | 23.333 | 20.000 | 33.182 |
| 14 | 21.739 | 16.742 | 15.204 | 33.273 | 27.835 | 18.987 | 0.000 | 26.069 |
| 15 | 0.000 | 10.294 | 22.544 | 39.216 | 23.178 | 6.316 | 0.000 | 25.872 |
| 16 | 14.286 | 10.732 | 18.624 | 35.694 | 23.114 | 10.625 | 0.000 | 24.037 |
| 17 | 25.000 | 17.273 | 32.083 | 36.030 | 30.649 | 15.686 | 0.000 | 31.662 |
| 18 | 21.277 | 17.021 | 25.867 | 36.356 | 30.960 | 13.223 | 0.000 | 30.052 |
| 19 | 9.091 | 17.972 | 22.676 | 32.372 | 26.445 | 12.805 | 0.000 | 26.087 |
| 20 | 0.000 | 24.615 | 23.372 | 28.669 | 23.264 | 17.308 | 0.000 | 24.636 |

| run | r534 | (60796 samples) | | | | | | |
|---|---|---|---|---|---|---|---|---|
| bm | z1 | z2 | z3 | z4 | z5 | z6 | z7 | totals |
| 1 | 11.364 | 8.491 | 27.561 | 38.070 | 28.343 | 17.808 | 0.000 | 30.017 |
| 2 | 7.143 | 9.942 | 20.277 | 33.830 | 24.504 | 15.328 | 0.000 | 24.767 |
| 3 | 26.923 | 14.179 | 22.455 | 39.574 | 31.929 | 22.321 | 0.000 | 31.004 |
| 4 | 16.667 | 12.987 | 16.572 | 33.429 | 26.168 | 14.783 | 50.000 | 24.618 |
| 5 | 12.500 | 12.442 | 20.998 | 33.119 | 27.502 | 15.714 | 0.000 | 25.612 |
| 6 | 40.000 | 15.074 | 21.757 | 36.197 | 31.574 | 12.500 | 0.000 | 29.366 |
| 7 | 12.000 | 15.854 | 26.250 | 41.408 | 33.714 | 16.822 | 0.000 | 32.850 |
| 8 | 23.529 | 22.222 | 25.210 | 34.539 | 34.622 | 21.256 | 0.000 | 30.464 |
| 9 | 28.571 | 16.779 | 22.973 | 36.667 | 34.737 | 13.684 | 0.000 | 30.675 |
| 10 | 21.739 | 13.566 | 23.538 | 41.449 | 31.954 | 17.857 | 0.000 | 31.568 |
| 11 | 21.429 | 7.339 | 24.060 | 32.962 | 24.169 | 16.667 | 0.000 | 25.509 |
| 12 | 0.000 | 14.286 | 25.000 | 25.000 | 18.519 | 40.000 | 0.000 | 22.078 |
| 13 | 24.138 | 15.344 | 25.512 | 39.158 | 33.153 | 25.000 | 0.000 | 32.165 |
| 14 | 29.412 | 16.000 | 17.364 | 39.379 | 36.215 | 10.526 | 0.000 | 30.481 |
| 15 | 20.000 | 10.280 | 20.482 | 36.545 | 29.766 | 12.195 | 40.000 | 27.260 |
| 16 | 16.000 | 16.850 | 20.730 | 35.205 | 36.631 | 29.825 | 0.000 | 30.679 |
| 17 | 28.571 | 24.188 | 26.126 | 43.715 | 45.929 | 20.833 | 0.000 | 38.542 |
| 18 | 34.146 | 14.063 | 23.865 | 38.801 | 37.548 | 19.014 | 0.000 | 32.714 |
| 19 | 37.500 | 15.564 | 19.884 | 28.704 | 28.476 | 13.415 | 0.000 | 24.773 |
| 20 | 0.000 | 13.636 | 20.000 | 25.816 | 18.373 | 14.754 | 0.000 | 20.588 |

# Bibliography

[1] M. F. Penny, R. H. Abbot, D. W. Lane, "LADS depth bias investigations: formulation of a multi-parameter depth bias model", DSTO report 25 Nov 1994.

[2] L. Estep, "A Review of Airborne Lidar hydrographic (ALH) systems", The Hydrographic Journal, Jan 1993.

[3] M. F. Penny, R. H. Abbot, D. M. Phillips, B. Billard, D. Rees, D.W.Faulkner, D.G. Cartwright, B. Woodcock, G. J. Perry, P.J. Wilsen, T. R. Adams, and J. Richards, "Airborne laser hydrography in Australia", Applied Optics vol. 25, no. 13, pp. 2046-58, July 1986.

[4] M. F. Penny, B. Billard, R. H. Abbot, "LADS the Australian Laser Airborne Depth Sounder", Int. J. Remote Sensing, Vol. 10, no. 9, pp. 1463-1497, 1989.

[5] C. Setter and R.J. Willis, "LADS from development to hydrographic operations", Proceedings U.S. Hydrographic Conference ', Norfolk USA, pp. 134-143, April 18-23, 1994.

[6] R. Nain, "Royal Australian Navy Laser Airborne Depth Sounder, The First Year of Operations", International Hydrographic Review, LXXI (1), pp. 109-119, March, 1994.

[7] J. Banic, J.S. Sizgoric, R. O'Neill "Scanning lidar bathymetry for water depth measurement"' Proc. SPIE, vol. 663, 187-195, 1986.

[8] O. Steinvall, T. Claesson, J. Lexander, and A. Widen, "Laser depth sounding in the Baltic Sea", Appl. Optics vol. 20, no. 19, pp. 3284-3286, Oct. 1984.

[9] O. Steinvall, K.Koppari and U. Karlsson, "Experimental evaluation of an airborne depth sounding lidar", Optical Engineering, vol. 32, no. 6, pp. 1307-1321, June 1993.

[10] K. Koppari, U. Karlsson and O. Steinvall, "Airborne Laser Depth Sounding in Sweden", International Hydrographic review, LXXI (2), pp. 70-90, September 1994.

[11] O. Steinvall, K. Koppari and U. Karlsson, :"Airborne laser depth sounding, System aspects and performance" Ocean Optics XII SPIE vol. 2258, pp. 392-412, Bergen 1994.

[12] P. Thuresson, "SHOALS-Hawk Eye", International Laser Bathymetry Seminar 3-4 May, Ronneby, Sweden, 1994. + Broschyre material Sab Dynamics, Jonkoping Sweden.

[13] W.J.Lillycrop, L.E. Parson, L.L. Estep, P.E. Larocque, G.C. Guenther, M.D. Reed and C.L. Truitt, "Field testing of the U.S. army corps of engineers airborne lidar hydrographic survey system", Proceedings U.S. Hydrographic Conference '94, pp. 144-151, April 18-23, 1994 Norfolk USA.

[14] G.C. Guenther, P.E. LaRocque, W.J.Lillycrop, "Multiple surface channels in Scanning Operational Airborne Lidar Survey (SHOALS) airborne lidar", Ocean Optics XII SPIE vol. 2258, pp.

[15] Hoge F.E., Swift R.N., Federick E.B. "Water depth measurement using an airborne pulsed neon laser system", Applied Optics, vol. 19, no. 6, pp 871-883, 1980.

[16] Hoge F.E., Wright C.W., Krabill W.B., Buntzen R.R., Gilbert G.D., Swift R.N., Yungel J.K., Berry R.E. "Airborne lidar detection of subsurface oceanic scattering layers", applied Optics, vol. 27, no. 19, 3969-3977, 1988.

[17] Curran T., Keck T., Contarino V.M., Harris M.M., Haimbach S.P.,"Digital ABC Laser Sounder Bathymetry", Proc. SPIE Ocean Optics IX, vol. 925, pp 242-249, 1988.

[18] Lutomirski R., Haimbach S., Curran T. and Gibbons J., "Performance modelling and analysis of the Ocean Water Lidar (OWL) Hydrographic System", Proceedings U.S. hydrographic Conference '94, pp. 200-205, April 18-23, 1994 Norfolk USA.

[19] Tsetkov E.A. "Lidar related shipboard and aircraft measurements," Report at the Technical Seminar on Issues in Lidar and Ocean. Naval Ocean Systems Center San Diego, CA, Oct. 1-2, 1991.

[20] Liu Shi-Shen, "Estimate of maximum penetration depth of lidar in coastal water of the China Sea", Proc. SPIE Ocean Optics X, vol. 1302, 655-661, 1990.

[21] B.Billard, "Rogue point elimination in airborne laser hydrography", Appl Opt. 25, 2074 1986.

[22] B. Billard, R. H. Abbot, and M. F. Penny, "Airborne estimation of sea turbidity parameters from the WRELADS laser airborne depth sounder", Appl. Opt. 25, 2080 1986.

[23] B. Billard, "Remote sensing of scattering coefficient for airborne laser hydrography", Appl. Opt. 25, 2099 1986.

[24] B. Billard, "Estimation of a mean sea surface reference in the WRELADS airborne depth sounder", Appl Opt. 25, 2067 1986.

[25] B. Billard, R. H. Abbot, and M. F. Penny, "Modelling depth bias in an airborne laser hydrographic system", Appl. Opt. 25, 2089 1986.

[26] Hydrographer of the Navy, "Admiralty Tidal handbook No.2: Datum's for Hydrographic Surveys", Admiralty, Taunton, Somerset, England, May 1975.

[27] J. S. Bendat and A. G. Piersol, "Random data analysis and measurement procedures", John Wiley & Sons, 1986.

[28] R.J.Wiley, "Electronic Intelligence: the Analysis of Radar signals", Artech House, 1982.

[29] M. F. Penny, R. H. Abbot, D. W. Lane, "LADS depth bias investigations: formulation of a two parameter depth bias model", DSTO report 25 Nov 1993.

[30] B. Billard and P. Wilsen, "Sea surface and depth detection in the WRELADS airborne depth sounder", Appl Opt. 25, 2059 1986.

[31] A. Kouzoubov and J.T.Thomas, "Underwater Light Propagation Study", DoD Report (PO9383DX), 1998.

[32] W. H. Press, B. P. Flannery, W. T. Vetterling, S. A. Teukolsky, "Numerical Recipes in C, The Art of Scientific Computing", Cambridge University Press, NY, 1992.

[33] R. M. Measures, "Laser Remote Sensing: Fundamentals and Applications", John Wiley & Sons, 1984.

[34] F. Durst, A. Melling and J. H. Whitelaw, "Principles and Practice of Laser-Doppler Anemomentry", Academic Press, 1976.